POLITECNICO DI TORINO

Master's Degree in Aerospace Engineering

Master's Degree Thesis

Aerodynamic and aeroacoustic optimization of drone propeller blades

Supervisors

Prof. ARINA Renzo

Prof. RAGNI Daniele

Prof. AVALLONE Francesco

Candidate

CARIELLO Maria Rossella

10 April 2024

Summary

Recently, interest in battery-powered Unmanned Aircraft Vehicles has grown as potential sustainable aerial transport. Reference is made to several Sustainable Development Goals of the 2030 Agenda thanks to the wide field of application of UAVs, covering health, food security, infrastructure, cities, and human settlements. Among the challenges that the integration of UAVs in the existing aviation airspace has to overcome, noise regulation and public acceptance appear, as the noise signature of propellers could critically penalize their perception in the community. In propeller design optimization, noise reduction typically entails a trade-off with aerodynamic efficiency or thrust generation. Moreover, small size and low flight speed collocate drones in the range of Low Reynolds Number, $10^4 \leq Re_c \leq 10^5$, where conventional airfoils exhibit a critical performance level.

In this thesis, a multi-objective optimization is conducted to find an efficient and silent propeller, starting from a two-blade propeller similar to an APC 9x6, with a diameter of 30 cm, reshaped with NACA 4412 airfoil sections, operating at 4000 rpm and at low advance ratio. Specifically, the condition at J=0.1 is studied, and the influence of modifications in blade design concerning chord length and twist angle on the figure of merit and tonal noise sound pressure level is investigated. Second-degree chord distributions are parameterized, identified by the chord value at the root and tip, along with third-degree twist angle distributions, identified by the twist angle value at the root of each blade.

Blade Element Momentum Theory is employed for calculating the aerodynamic load distribution across the blade, combining data from Xfoil at $Re = 50000$, while the frequency-domain Helicoidal Surface Theory (Hanson 1980) is implemented for predicting noise. A study of the several tonal noise components at low frequencies is performed. Using a genetic algorithm 'gamultiobj', multiple compromise solutions were found, and it was possible to achieve a noise reduction of about -2 dB and an increase in the figure of merit by 5% on the same blade.

Acknowledgements

Table of Contents

List of Tables

List of Figures

Chapter 1

Introduction

1.1 Unmanned aircraft systems

An Unmanned Aircraft System is defined as a vehicle operated with no pilot on board (UAV) with eventually all the associated elements to control it remotely. These systems include remotely piloted air systems (RPAS) and autonomously and semi-autonomously controlled UAV. The early records of aerial unmanned vehicles occurred in the twentieth century in military scenarios, from when they had been employed to carry explosive payloads to a predetermined target or for surveillance aims. Thanks to innovation in control and sensor technology, resulting in competitive costs, UAV applications expanded to different fields like Search and Rescue, natural resource monitoring, environmental compliance, pipeline and power inspection, sustainable small cargo, urgent medical deliveries, sport photos and filming. 2013 is referred as a crucial year for the development of drones in the civil market, due to the announcement of the package delivery project by Amazon.

Figure 1.1: Examples of UAVs for military, transport and filming purposes

UAVs can be designed in different sizes, configurations and complexity (**Figure 1.1**). Flying wing and blended wing body configuration ensure lower drag and

stealth. When hovering and vertical flight are prioritized, the quadcopter or multirotor configuration are preferred. While long-range drones are powered by traditional internal combustion and jet engines, for shorter-range missions these have been replaced with electric power, mostly with lithium-polymer batteries (Li-Po) or hydrogen fuel cells. Endurance of several weeks has been reached with solar-powered drones, which could be potentially employed to provide Internet connectivity in remote areas. Miniature UAVs up to the size of 5 centimeters have been realized for low-altitude support operations, forming the category of Micro Air Vehicles (MAVs).

1.1.1 Regulations

The ICAO Model UAS Regulations titled Parts 101, 102 and 149 with Advisory Circulars (ACs) offer a template for Member States to implement or to supplement their existing UAS regulations. EU Regulations 2019/947 and 2019/945 [1] outline the framework for civil drones to be operated safely within European skies. Inside the Regulations, UAS are classified into three main categories of operations in a risk-based approach:

- The "Open" category does not require authorization to fly from an Aviation Authority but should respect boundaries for the operation, such as distance from people and aerodromes. An unmanned aircraft falls under the open category if its Maximum Take off Mass (MTOM) is below 25 kg and it is operated within the Visual Line of Sight (VLOS), until an altitude of 120 m above ground level.

- The "Specific" operation category demands a risk assessment and Operations authorization correlated to the particular task. Examples of UAS operations in the group are: BVLOS (Beyond Visual Line Of Sight) operations; when operating with a MTOM that exceeds 25 kg; flying higher than 120m above ground level; in case of dropping material; when operating a drone in an urban environment with a MTOM> 4 kg.

- The "Certified" operations comprehend a higher associated risk and are often requested by organizations providing services such as passengers or cargo transport.

The classification is reported in **Fig.1.2**. **Figure 1.3** describes the three subcategories (A1,A2,A3) of the "Open" group of UAS. The subdivision is based on operational limitations and requirements for the remote pilot, while the label C0-C4 is representative of the UAS size.

Figure 1.2: Categories of operations according EU Regulations 2019/947 and 2019/945

Figure 1.3: Subcategories and limits for "Open" operations UAS from 1st January 2024

1.2 Research Framework and goals

Recently, interest in the battery-powered UAV sector has grown as potential sustainable aerial transport. Reference is made to several Sustainable Development Goals of the 2030 Agenda thanks to the wide field of application of UAVs, covering health, food security, infrastructure, cities, and human settlements. Among the several challenges that the integration of UAVs in the existing aviation airspace has to overcome, besides vehicle certification and operational safety, noise regulation and public acceptance appear.

Drone noise signature could critically penalize their perception in the community. Differing from aircraft, whose main concern is the noise in the vicinity of the airport area, UAVs could operate relatively close to people during the whole en-route phase. A comparison with aircraft noise is found in Ref.[2]. The frequency spectra of two multi-copters (DJI M200 and Yuneec Typhoon) and two conventional civil aircraft (Boeing 737 MAX 8 and Airbus 320) have been analyzed from the authors and reported in **Fig.1.4**. The former were recorded in a level flyover phase of about 46 m above the microphone, at the maximum speed of the vehicles, while the latter were sampled in a take-off phase at around 435 m high over a microphone at 900 meters from the end of the south runway of London Heathrow Airport.
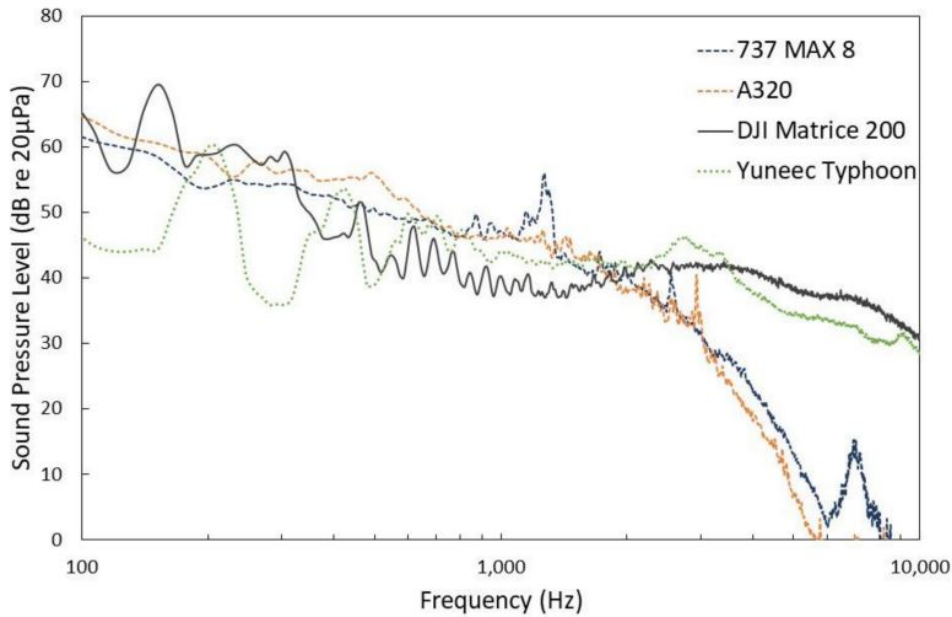
Figure 1.4: Frequency spectra normalized at 65 dBA of two conventional aircraft (Airbus A320 and Boeing 737-8 MAX) and two multi-copter UAVs (DJI M200 and Yuneec Typhoon) from Ref. [2]

The quadcopter and hexacopter noise footprints are primarily tonal along the low-frequency spectra (below 1 kHz). High-frequency emissions of the selected UAVs are attributed to turbulent boundary layer trailing edge noise, the interaction between near rotors, and electric motor noise. Moreover, at high frequencies, the sound pressure level is not subject to atmospheric absorption that occurs when operating with aircraft at long-range distances.

In Ref. [3] the authors concluded that even with the same L_{Aeq} of 65 dB(A), quadcopter UAV noise is preferred 33% less than civil aircraft noise in psychoacoustic tests.

Regulation (EU) 2019/945 [4] defines the maximum sound power level L_{WA} for classes C1 and C2 of the "Open" category by limiting the value at 85 dB when operating under 900 m for the first two years from the start of operation, while EASA in 2022 established the guidelines [5] to measure and compare various UA designs below 600 kg in hover and level-flight operational conditions.

Passive noise control strategies are pursued for small and medium UAVs, particularly in multi-rotor configurations. Looking at the single unity of the propulsion systems, blade design optimizations for specific operating conditions are found in the literature to mitigate the tonal component of the noise. The attenuation of broadband noise could be achieved through trailing edge serration [6], boundary layer trips, or porous materials structures [7] .

To understand aerodynamic noise generation and the relative significance of every sound source, the comprehension of the flow characteristics at the representative Reynolds number is fundamental. Small size and low flight speed collocate drones in the range of Low Reynolds Number, $10^4 \leq Re_c \leq 10^5$, where conventional airfoils exhibit a critical performance level. Moreover, in blade design optimization, noise reduction typically entails a trade-off with aerodynamic efficiency or thrust generation [8, 9]. Instead of addressing aeroacoustic refinements after the attainment of an efficient propeller in an iterative process, multi-objective optimizations recently consent to reach two or more targets to guarantee the best design solution as deemed by the operator [10, 11, 12, 13].

The aeroacoustic signature of a two-blade propeller at Low Reynolds numbers is examined in Ref. [14] through the comparison of high-fidelity numerical solutions, low-fidelity prediction models and experimental measurements, providing a benchmark for operations in axial flow controlled conditions. In Ref. [15] the characteristics of the flow around the blades and transitional boundary layer proprieties at different advance ratios are investigated through oil-flow visualization and PIV, and subsequently linked to noise generation mechanisms.

This thesis constitutes an attempt at a simultaneous aerodynamics and aeroacoustics optimization of a single propeller design, limiting the case study to the attenuation of low-frequency tonal noise at a low advance ratio.

1.3   Outline of the thesis

This project of thesis will follow the following structure.

- Chapter 1: Introduction to UAVs, aerodynamic noise problem and structure of the work developed in this thesis;

- Chapter 2: Introduction to propellers and their operation at Low Reynolds number, insight on the characteristics of the aerodynamic regime;

- Chapter 3: Overview of the governing equations of fluid dynamics for propellers;

- Chapter 4: Understanding of Blade Element Momentum Theory and corrections to the model;

- Chapter 5: Introduction to aeroacoustics and sound metrics;

- Chapter 6: Outline of sources of aerodynamic noise for propellers;

- Chapter 7: Understanding of Helicoidal Surface Theory at the base of the noise prediction;

- Chapter 8: Literature review, definition of geometric and operative parameters of the case study and aeroacoustic setup, implementation of the models, aerodynamic and aeroacoustic study. Parameterization of several blades and design space exploration;

- Chapter 9: Verification of the implemented methods for load and noise prediction with literature results

- Chapter 10: Introduction to the optimization framework and analysis of results

- Chapter 11: Conclusions of the thesis with recommendations about future work.

Chapter 2

Propellers

A propeller consists of a small number of blades attached axisymmetrically to a rotating hub. When spinning, it creates a pressure difference between the two surfaces of the blade, exerting thrust upon the fluid in which it is immersed. The blade of a propeller can be thought to be similar to an aircraft wing of reduced size, so the aerodynamic behavior of the propeller in a flow has familiarity with the aerodynamics of a finite wing.

Figure 2.1: Two-blade propellers for UAV

The wing length is called span, while the wing width is named chord. A chord is defined from the most forward point, named leading edge, to the most rearward point, the trailing edge. The length of the chord usually varies along the span. The cross-section of the wing, properly named airfoil, characterizes the pattern of a uniform airflow that goes from left to right as it follows. An air particle accelerates

its motion because of the curved shape of the airfoil. The airfoil upper surface has a greater curvature than the lower surface. As a consequence, the flow over the airfoil has a higher speed compared to the flow below the airfoil. Bernoulli's principle states that an increase in speed corresponds to a reduction of the static pressure, thus the air pressure acting on the airfoil upper surface is less than the pressure on the lower surface. The pressure difference acting on the cross-section of the blade is the reason for the generation of lift and drag.
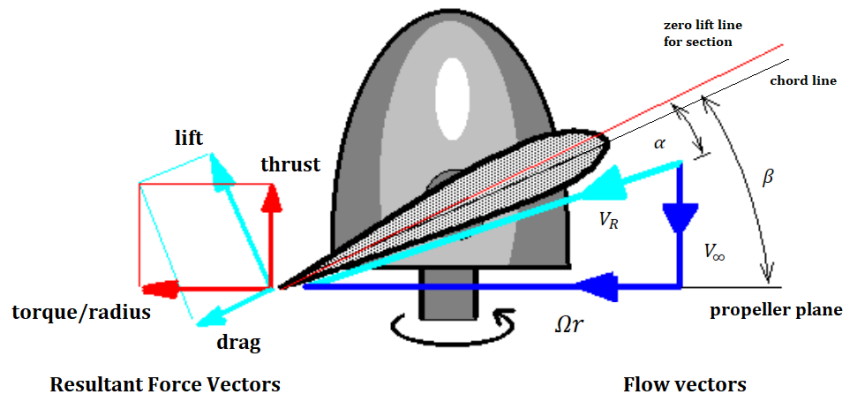
Figure 2.2: Cross section of a blade, flow vectors and resultant force vectors

The angle of attack, α or AoA, is defined as the angle subtended by the direction of airflow relative to the airfoil chord line. Varying the angle of attack, the propeller disk changes its own thrust. With an increase in the angle of attack, lift increases linearly, usually up to $15° \pm 2°$, and then drops due to the stalling of the airfoil, while the drag force continues to increase.

The angle between the chord line of an airfoil and the plane of the propeller disc is known as the local pitch angle, β. Usually, the local pitch angle at the 75% of the blade is taken as a reference. Pitch distribution refers to the gradual change in the local pitch angle from the root of a propeller blade to its tip. On account of the tangential velocity being much higher at the tip of the blade than it is at the root, the presence of a twist along the span is necessary to maintain a more or less constant angle of attack distribution.

According to their operating mechanism, propellers can be divided into two groups:

- Fixed-Pitch propellers

- Constant-Speed propellers

Fixed-pitch propellers are characterized by having the highest efficiency in correspondence to an optimum angle of attack. Conversely, variable-pitch propellers can manage the blade angle during the different flight phases. Because of the weight and the complexity of the variable pitch mechanism, UAV propellers are designed in the fixed pitch configuration. Therefore, drone propellers are optimized for a particular flight phase and angle of attack, resulting in reduced efficiency in off-design conditions.

An important non-dimensional term to describe the operating conditions of the propeller is the Advance Ratio, J,

$$J = \frac{V}{nD}$$

where V is the freestream fluid velocity in m/s, D is the propeller diameter in m, and n is the rotational speed of the propeller in revolutions per second.

The following analysis can be conducted at constant V or at constant n. If the freestream velocity increases, for example in an experimental setup, the angle of attack over the blade decreases, due to the rise of the inflow angle $\phi = \beta - \alpha$. This is shown in **Figure 2.3** with two velocity triangles for a generic blade section at the same tangential velocity and two different advance ratios $J_2 > J_1$, corresponding to $V_{\infty 2} > V_{\infty 1}$. The inflow angle is defined as the angle between the propeller plane and the velocity resultant vector, taking into account the effects of induced velocity. An in-depth focus on the induction factors, a and b, will be dedicated in Chapter 3.
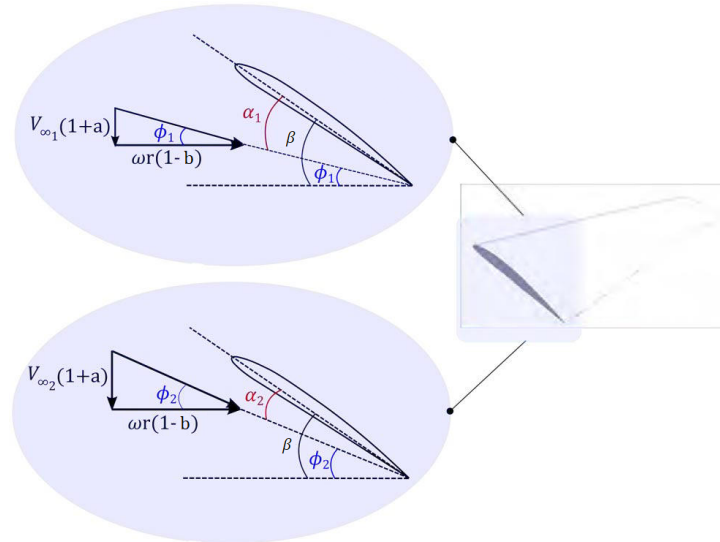
Figure 2.3: Velocity triangles for a fixed-blade section at two different free-stream velocities $V_{\infty 2} > V_{\infty 1}$ from Ref. [15]

The propulsive efficiency is defined as the ratio of the power transferred to the air mass moved through the propeller disk to the mechanical power required to drive the propeller.

$$\eta = \frac{TV}{\Omega Q}$$

Ω is the angular speed of the propeller in rad/s, T is the thrust generated by the propeller and Q is the required torque.

Fig. 2.4 shows the propulsive efficiency, η, at different advance ratios. Although the figure represents the envelope of maximum efficiency for a variable pitch propeller, it clarify that fixed blade-propeller are designed to be optimal at a certain design point, and that in the off-design operating conditions the efficiency drops dramatically. The maximum thrust is reached at fixed point $V = 0$ **(Fig.2.5),** when the propeller is in hover condition. In this case, the local angle of attack is maximum at every point of the blade and it is equal to the local pitch angle. In addition, a limit value for J exists and it represents the threshold for the propeller acting in tractor configuration. If the freestream velocity increases so that the angle of attack becomes $\alpha \approx 0$, equal to a negligible thrust, the propeller disk reaches a braking configuration. After this value of the advance ratio, when thrust is below zero, the propeller disc operates in a windmill regime.
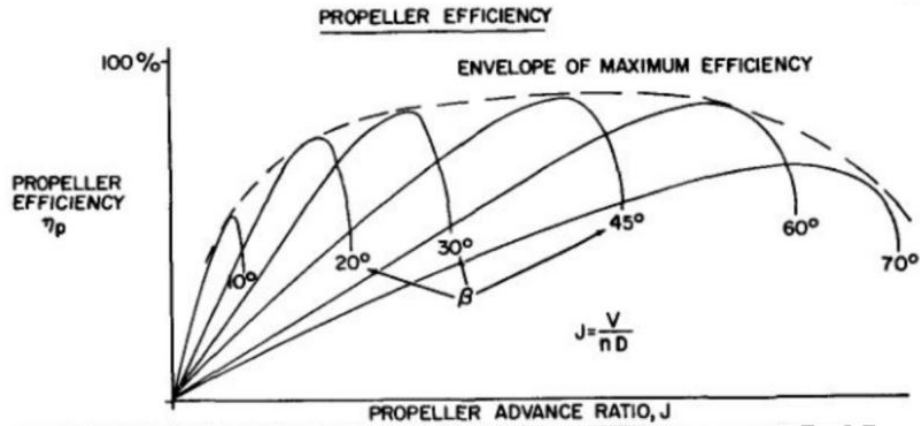
Figure 2.4: Propeller efficiency vs advance ratio for blades with different local pitch angles at 0.75 radius
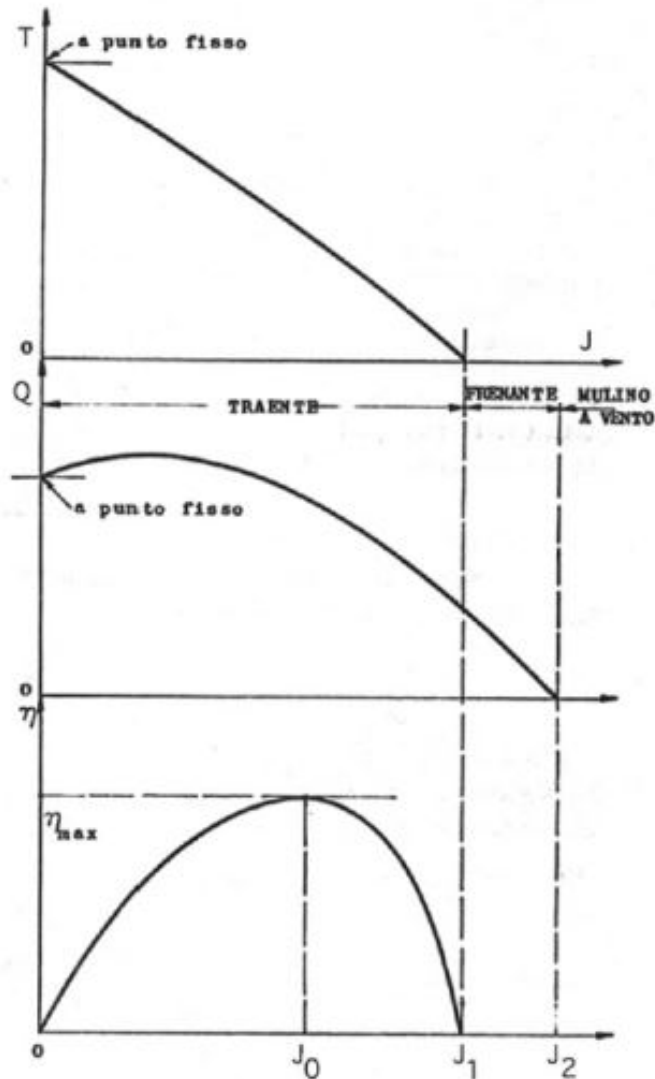
Figure 2.5: Propeller Thrust, Torque and Efficiency with Advance Ratio

2.1 Propellers at Low Reynolds number

Several databases for preliminary studies on propellers have been realized after experimental tests, such as the one in Ref. [16], where the performance of different two-blade propellers at low Reynolds numbers is analyzed at various rotational speeds. Discrepancies in efficiency curves and thrust and power characteristics are particularly noticeable at moderate advance ratios ($J = 0.4 - 0.6$), demonstrating superior performance for conditions with a higher RPM, corresponding to higher

chord-based Reynolds numbers. Results for APC Thin Electric 11x8 are presented as examples in **Fig. 2.6**
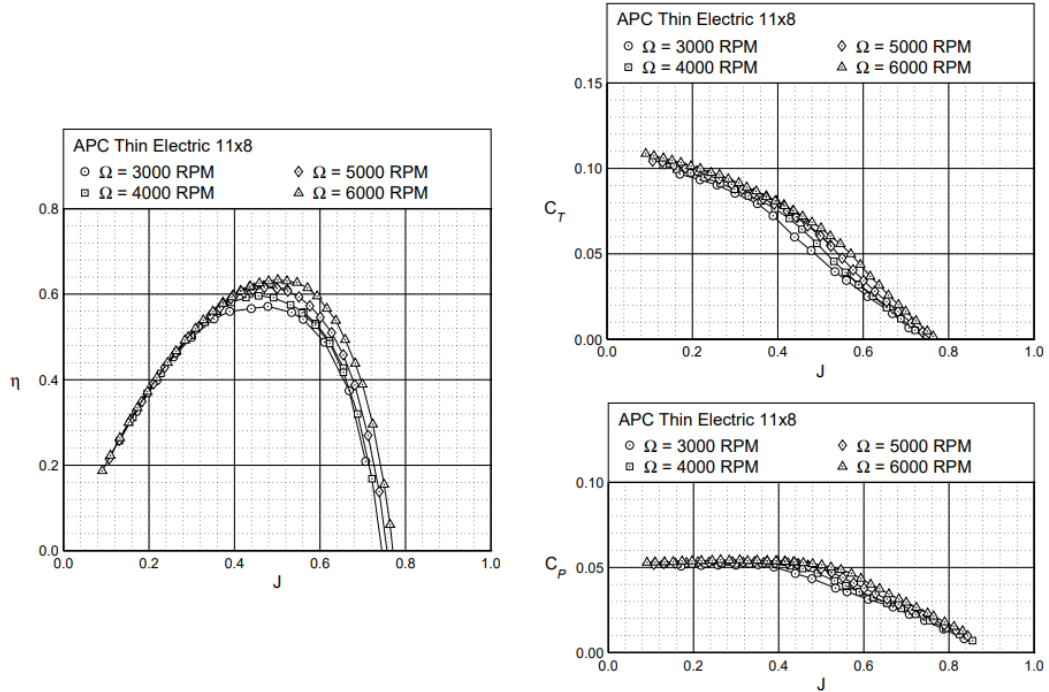
Figure 2.6: APC Thin Electric 11x8

In the following paragraphs, a step back is taken to explain the concepts of Reynolds number and boundary layer. Subsequently, the behavior of an airfoil at low Reynolds numbers is analyzed.

The Reynolds number is a nondimensional parameter that describes the ratio of inertial forces to viscous forces within a fluid. It is defined as

$$Re = \frac{\rho V L}{\mu}$$

where V is the flow speed (m/s), L is a characteristic length (m) of a surface within the flow, ρ is the density of the fluid and μ is the dynamic viscosity of the fluid (Pa s or N s/m2 or kg/(m s)). When discussing propellers, the characteristic length typically refers to a chord, thus the chord-based Reynolds number is considered, Re_c.

Aerodynamic forces generated between a moving surface within a fluid depend on the viscosity of the fluid. As the fluid moves past the object, the molecules right

next to the surface stick to the surface. The molecules just above the surface are slowed down in their collisions with the molecules sticking to the surface. These molecules in turn slow down the flow just above them. The boundary layer is defined as a thin layer of fluid near the surface in which the velocity changes from zero at the surface to the free stream value far from the surface. The boundary layer may be laminar or turbulent depending on the value of the Reynolds number. For lower Reynolds numbers, the boundary layer over an airfoil is laminar. The streamwise velocity inside the boundary layer changes uniformly moving away from the wall. For higher Reynolds numbers, the boundary layer is turbulent, and the streamwise velocity is characterized by unsteady swirling flows. The value of the critical Reynolds number is dependent on the geometry of the system. The external flow reacts to the shape of the boundary layer just as it would to the physical surface of an object. The shape of the boundary layer can change because of the separation of the boundary layer, which happens in the presence of a strong adverse pressure gradient. When the flow separates at a high angle of attack the airfoil is in stall conditions and the lift is lost. The turbulent boundary layer is more resistant to separation. If the transition to a turbulent regime occurs before the separation, the shape of the boundary layer forces the flow to a minor deviation from the surface than in the laminar case, which reflects in a minor parasitic drag.

A common feature across all UAVs is their small length scale and relatively low flight speed, which correspond to flight domain characterized by chord-based Reynolds numbers between $10^4 < Re_c < 10^5$, defined as Low Reynolds Number regime. To make a comparison, conventional aircrafts operate above $Re_c = 10^6$.

Empirical data are widely collected for low-speed airfoil design and juxtaposed to airfoil data at the typical aircraft velocities range [17][18]. From **Fig. 2.7**, **2.8**, **2.9**, it is evident that airfoil performance degrades for Reynolds number below 10^5. While the maximum aerodynamic efficiencies $C_l/C_{d_{max}}$ for low-speed fixed-wing aircraft are located between 10 and 10^2, values for MAVs at low Reynolds numbers are usually less than 10. Moreover, to achieve this value at low Reynolds numbers, airfoils must be selected taking as reference wings of birds and insects. Specifically, thin airfoils with moderate camber quantity are found to perform best[18].

Fig. 2.10 depicts the streamlines of a flow at Reynolds numbers below $Re = 10^6$ over a generic airfoil with a moderate Angle of Attack [19].

- For flow regimes between $10^4 \leq Re \leq 5 \cdot 10^4$, the boundary layer is entirely laminar and resistant to transition. Laminar separation occurs near the trailing edge until the angle of attack is further increased. At that stage, the separation point moves toward the leading edge, causing a pronounced shear layer that ends in trailing-edge stall. The airfoil performance for a given angle of attack is affected by inadequate lift generation and high pressure drag as the Reynolds number decreases, resulting in a stalled configuration for almost
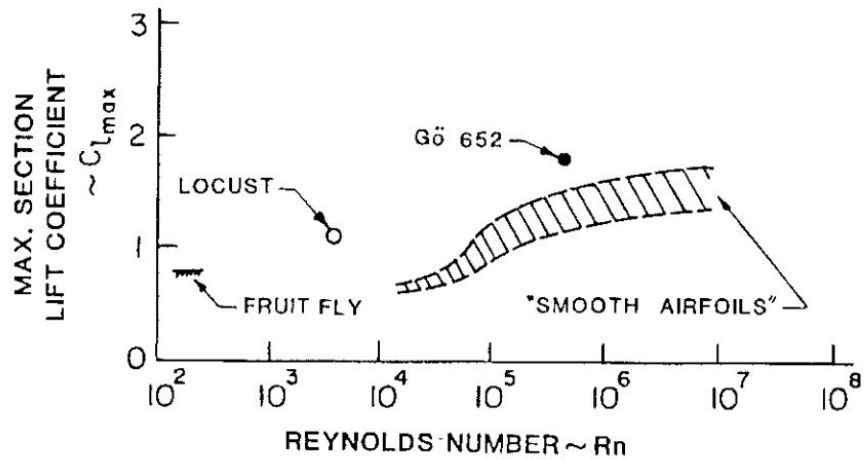
Figure 2.7: Maximum lift coefficient [18]
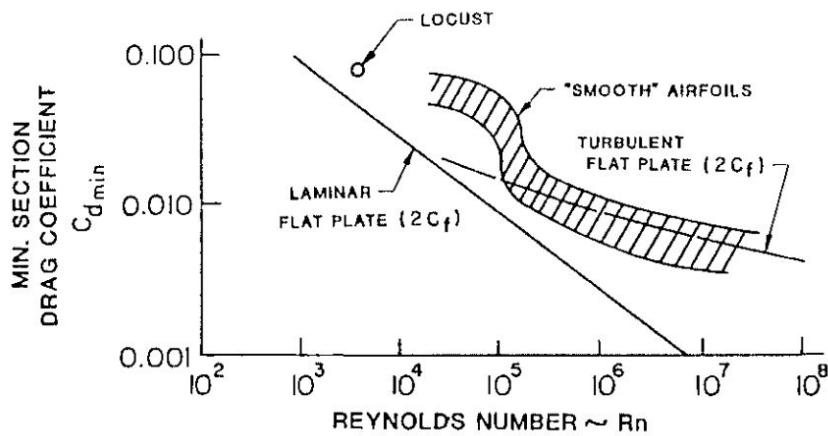
Figure 2.8: Minimum drag coefficient [18]

the entire operational range.

- The chord Reynolds number range between $5 \cdot 10^4 \leq Re \leq 10^5$ is characterized by large Laminar Separation Bubbles (LSB) on the upper surface of most airfoils. The origin of the laminar separation bubbles lies in the adverse pressure gradient that the boundary layer encounters near the leading edge and in the low kinetic energy of the boundary layer at this Reynolds number: the separation as a shear layer is followed by a gain of momentum from the freestream and reattachment as a turbulent boundary layer. The reattachment point is located back on the upper surface, nearer to the trailing edge as
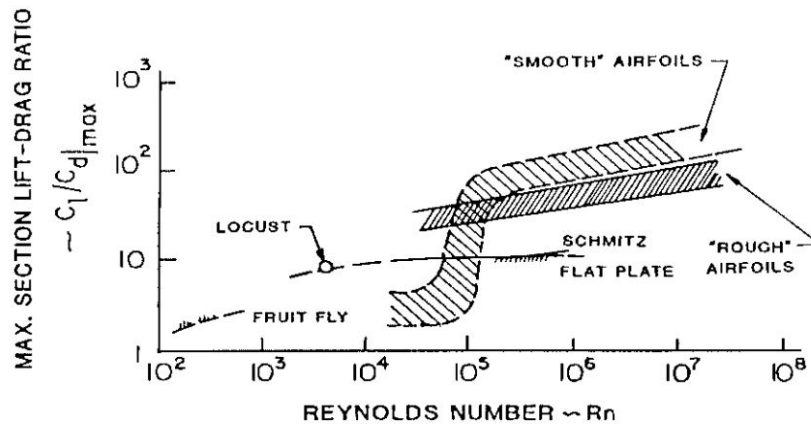
Figure 2.9: Maximum lift-to-drag ratio [18]

the angle of attack increases. When the airfoil is about to stall, the flow fluctuates between reattachment and complete separation, resulting in an unsteady aerodynamic phenomenon called hysteresis. Especially thick airfoils (above 6%) can be subjected to remarkable hysteresis.

- At Reynolds number $Re \geq 500,000$, the extent of the laminar separation bubble is reduced and the turbulent boundary layer remains attached until the trailing edge. At higher angles of attack, trailing edge stall occurs.

Figure 2.11 from Ref. [15] illustrates the extent of the laminar separation bubble on the suction side of a propeller blade operating at 4000 RPM and at different advance ratios, with the chord-based Reynolds number, Re_c, falling in the order of 10^4. The separation line and the reattachment line are denoted with S and R: the laminar separation bubble is observed to shift towards the leading edge and diminish in size as the advance ratio is reduced, which means as the angle of attack is increased. The angle of attack influence on the characteristics of the LSB is found to be predominant with respect to the variation of the Re_c at the several operational conditions.

Laminar separation bubbles result in rapid deterioration of the airfoil efficiency L/D. Attempts in active control of the boundary layer are widely found in literature in the form of forcing the early transition to a turbulent boundary layer by the installation of various types of "turbulators" (zig-zag tape strips, grooves, holes) at the proper location on the airfoil surface.

Measurements and high-fidelity simulation in PowerFLOW conducted by Casalino [14] have revealed that tripping the suction side of a propeller blade results in a

15

a) 10,000 < Re < 50,000

b) 50,000 < Re < 100,000

c) Re > 500,000
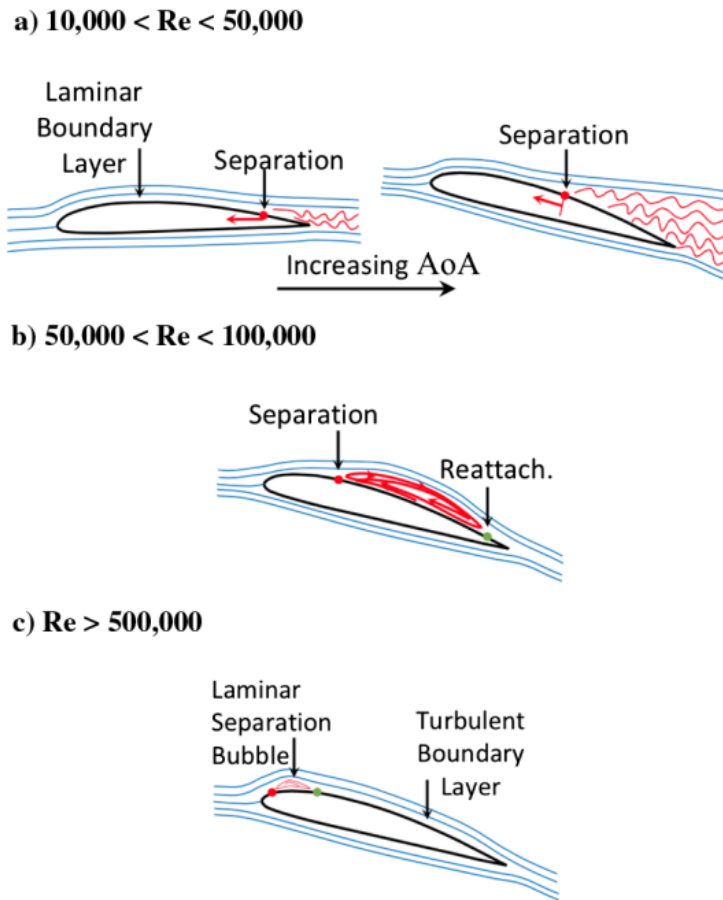
Figure 2.10: Boundary layer separation characteristics for a conventional airfoil at different Reynolds number regime below 10^6 from Ref.[19]

reduction of the high-frequency broadband hump generated by the laminar separation bubble. The trip location on the blade affects the broadband noise of 1 dB in hover conditions, and up to 10 dB close to zero thrust conditions, while does not impact the tonal noise component.
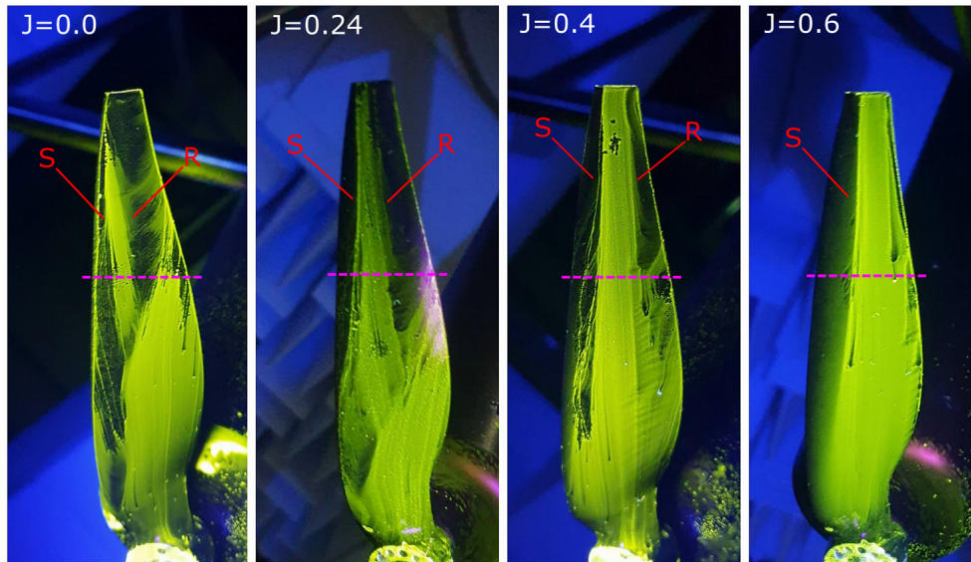
Figure 2.11: Oil flow visualization of laminar separation bubbles on the suction side of the blade at 4000 rpm and J=0, 0.24, 0.4, and 0.6 from Ref. [15]
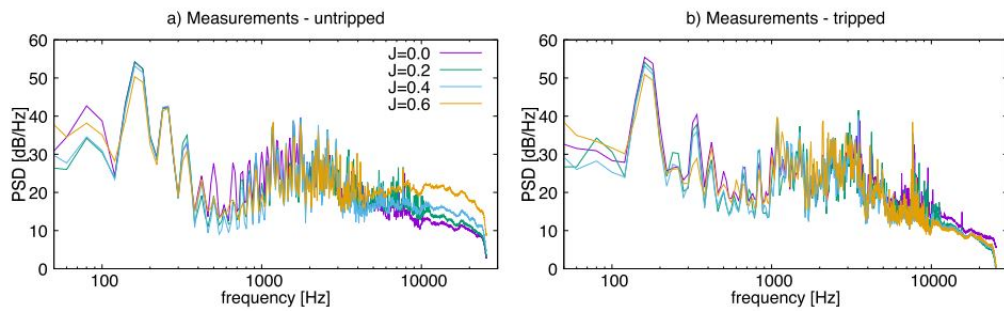
Figure 2.12: Noise power spectral density at the propeller plane for several values of the advance ratio with and without trip on the suction side of the blade from Ref. [14]

Chapter 3

Governing equations of fluid dynamics for propellers

In this chapter of the dissertation we assume the propeller to be fixed in the space, immersed in the flow, therefore the flow over the propeller is not interfered by the presence of another body. The governing equations for the motion of viscous, compressible fluids are the Navier-Stokes equations, which are non-linear second-order partial differential equations and impossible to solve analytically. Even if the flow is steady (e.g. an aircraft moving forward at a constant speed in a stationary atmosphere) there are regions very close to the surface where the boundary layer may be turbulent and moving chaotically as a function of time. If the flow remains attached to the body and the boundary layer does not separate, the airflow outside the boundary layer may be interpreted as inviscid. By applying the assumption of inviscid flow, the Navier-Stokes equation can be simplified to become the Euler equation. The flow of a two-dimensional wing is then divided into two distinct regions: the viscous boundary layer and the inviscid outer region. Within the former, the Navier-Stokes equations can be simplified in the Boundary Layer equation, considering that the length scale in the direction normal to the flow is shorter than length scales in other directions. The solution of the Euler equation could still be difficult to find in the presence of discontinuities and shock waves in a compressible flow, provided that the speed of the flow is greater than the speed of sound in some regions within the flow field.

A better way of simplifying the Navier-Stokes is to remove its time dependence by applying the statistical averaging technique proposed by Reynolds. This procedure is known as Reynolds Averaged Navier-Stokes equations or RANS equation. The new equation is similar to the Euler equation, except for a Reynold turbulent stress term as a new variable. The closure of the problem is granted by adding empirical equations of turbulence models to the basic governing equations.

If the flow is always subsonic everywhere within the flow field, the complexity of the governing equations can be reduced significantly. In the present situation, the model flow is described from the incompressible RANS or incompressible Euler equations adding the incompressible boundary layer equation. If the flow is assumed to be irrotational, the compressible Euler equation is simplified into the Full Potential Equation. For the incompressible flow case, the simplified governing equation is the Laplace Equation, which is a linear second-order partial different equation.

Real flows are 3-dimensional and the generation of computational grids for 3-dimensional flows is more complicated. To simplify the analysis of a 3-dimensional flow over a wing, it is assumed that the wing can be seen of as being composed of a large number of wing sections along the wing span axis. The flow over each wing section is assumed to be independent of what is happening over every other section, at the cost of introducing the 3-dimensionality effect using a suitable modeling technique. A quite effective method to reintroduce the 3-dimensionality is to assume that a vortex sheet is formed by the wing and is shed at the trailing edge of the wing. The vortex sheet induces a downwash to the incoming flow, reducing the effective angle of attack of the flow. This reduces the lift and creates a lift-dependent drag, namely the induced drag. This assumption is at the basis of the Lifting Line method, a fast method that gives accurate predictions for thin wings that have no sweep-back angle, without dihedral, and not highly tapered.

An analogous concept can be applied to investigate the aerodynamic properties of a propeller. What differentiates the propeller blade from the aircraft wing is that the propeller blade rotates around its longitudinal axis instead of only moving forward as in the case of the wing. Consequently, several Mach number and Reynolds number are involved along the propeller radius, and local velocities at the extremities could fall within the range of compressible flow even operating at relatively low speeds.

Moreover, the vortex sheet produced and shed by the blade at the trailing edge will have a shape similar to a helix, rather than just a flat sheet. The complex shape of the sheet makes it very difficult to analyze the induced flow field by utilizing the fundamental equation for a vortex known as the Biot-Savart equation.

For these reasons, the aerodynamic properties of the idealized propeller are often analyzed using reduced-order analyses, as the momentum theory of an actuator disk. The momentum equation can be combined with the blade element theory in a Blade Element Momentum theory. BEMT is extremely useful in predicting the aerodynamic performance of a rotary wing, such as propellers, helicopter rotors or wind turbine rotors. [20]

Chapter 4

Blade Element Momentum Theory

This chapter describes the Blade Element Momentum Theory, a standard method in propeller design that will be employed in this thesis to obtain the discretized distributions of loads along the propeller radius. BEMT is a combination of Blade Element Theory and Momentum theory. The former divides the propeller into several finite elements, so that each section of the blade is considered as a two-dimentional airfoil. The latter provides an approximation of inflow velocity by applying conservation of mass, momentum and energy to a control volume surrounding the propeller. BEMT approach stands out as the favored choice during the propeller design and optimization stages, as opposed to utilizing Computational Fluid Dynamics (CFD) simulations, primarily due to its significantly reduced computational expense, amounting to 10^{-5} CPU hours compared to the substantially higher 10^3 CPU hours associated with CFD methods. [21]

4.1 Momentum theory

The Simple Momentum theory was first proposed by Rankine in the mid-eighteenth century for the estimation of the ideal performance of a rotor. The theory assumes that physical quantities within a flow tube are solely a function of the axial position. This theory implies that there is no discontinuity in the tangential velocity component across a disk, which means it does not induce flow rotation. It is fundamental to remember that alone it cannot determine the flow field in the immediate vicinity of the propeller or the exact distributed forces acting on it. In fact, the theory is most effective when used to analyze the flow field at a significant distance from the propeller. The hypotheses used for the theory are

- Stationary and irrotational flow

- Ideal flow (incompressible and non viscous)

- Velocity and pressure gaps are constant along the disc radius

The propeller is seen as an actuator disc, consisting of an imaginary disc having the same diameter as the propeller. The actuator disc is contained in a streamtube flow that models the airflow path.

At the upstream section, the free stream velocity is the speed V of the vehicle. Downstream the flow is accelerated and visually the streamtube contracts itself, reaching a speed of V_0 as the air passes through the disc and settling at a speed V_s when approaching a sufficiently far location. The static pressure of the flow has a point of discontinuity in correspondence to the actuator disc. The pressure jumps from p_1 upstream of the disc to p_2 immediately downstream. The pressure difference acting upon the disc multiplied to the disc area, $A = \pi R^2$, corresponds to the thrust generated by the propeller, T.

$$T = A(p_2 - p_1)$$
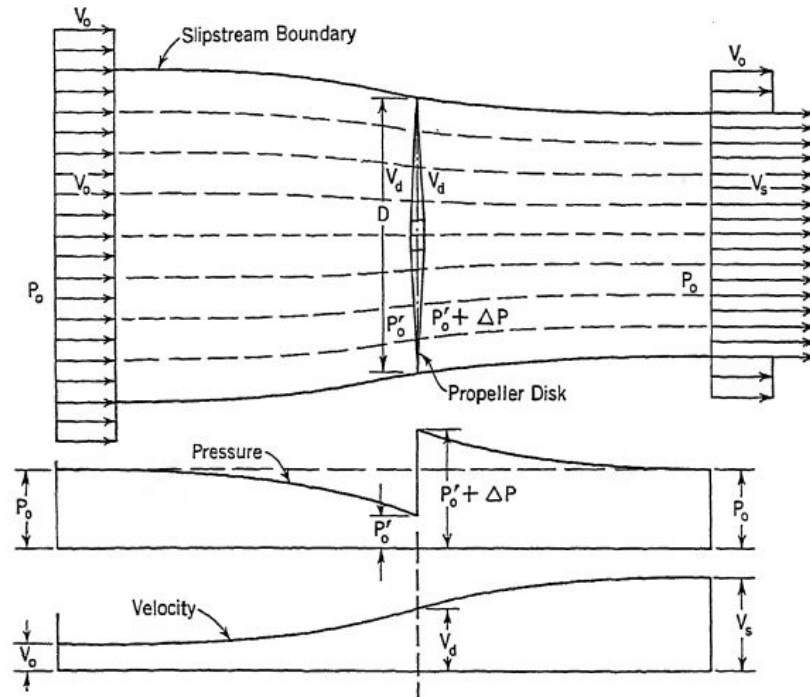
Figure 4.1: Momentum theory relationship from Ref.[22]

The thrust imparted to the air is equal to the mass flow rate within the streamtube multiplied by the difference between the air velocity at the end and at the beginning of the tube

$$T = \dot{m}(V_s - V)$$

Equating the previous expressions for thrust the following result is obtained:

$$p_2 - p_1 = \rho V_0(V_s - V)$$

Since the enthalpy in the far region upstream of the disc and in the region downstream of the disc remains unaltered, the Bernoulli equation returns the following results:

$$p_0 + \frac{1}{2}\rho V^2 = p_1 + \frac{1}{2}\rho V_0^2$$

$$p_2 + \frac{1}{2}\rho V_0^2 = p_0 + \frac{1}{2}\rho V_s^2$$

Therefore, combining the equations above:

$$p_2 - p_1 = \frac{1}{2}\rho(V_S^2 - V^2)$$

And including them in the aforementioned thrust definition

$$\rho V_0(V_s - V) = \frac{1}{2}\rho(V_s^2 - V^2)$$

The obtained equation can be simplified in order to highlight the following results

$$V_0 = \frac{1}{2}(V_s + V)$$

$$V_s = 2V_0 - V$$

If the propeller is stationary, the velocity induced by the propeller is simply $V_0 = \frac{1}{2}V_s$. Instead, assumed V as the vehicle velocity, We can define the inflow factor, a, as follows

$$a = (V_0 - V)/V$$

and the axial velocity induced by the propeller disc is

$$aV = V_0 - V = \frac{1}{2}(V_s - V)$$

The momentum theory developed by Rankine (1865) was modified by Froude in 1878 to take into account that the inflow factor is not constant along the actuator disc but is a function of the radial distance from the axis of the propeller. The actuator disc is now discretized in a very large number of rings of infinitesimal

width dr, so that the area considered for the momentum theory for an element at a radial station r is $2\pi r dr$. Therefore the elemental thrust is

$$dT = \rho V_0 2\pi r (V_s - V) dr$$

or, showing the induction factor,

$$dT = 4\pi \rho r V^2 a(1 + a) dr$$

The theory is refined by noting that a vortex sheet is shed at the trailing edge of the rotating blades. The presence of the vortex sheet induces an additional speed upstream of the disc and a reduction of speed downstream in the direction of rotation of the propeller. Therefore, the induced azimuthal speed is a small fraction of the rotational velocity, $b\Omega r$, where b is a small positive value and Ω is the rotational speed of the propeller in radian per second. Passing through the propeller disc, the streamline would have azimuthal and axial velocity, describing a helical shape. Moreover, the airflow is subjected to an azimuthal speed jump of $2b\Omega r$ [23] that multiplied by the mass flow rate and by r gives the expression for the elemental torque, dQ:

$$dQ = \rho V_0 \; 2\pi r dr \; 2b\Omega r \; r$$

which rearranged gives

$$dQ = 4\pi \rho r^3 \Omega V (1 + a) b dr$$
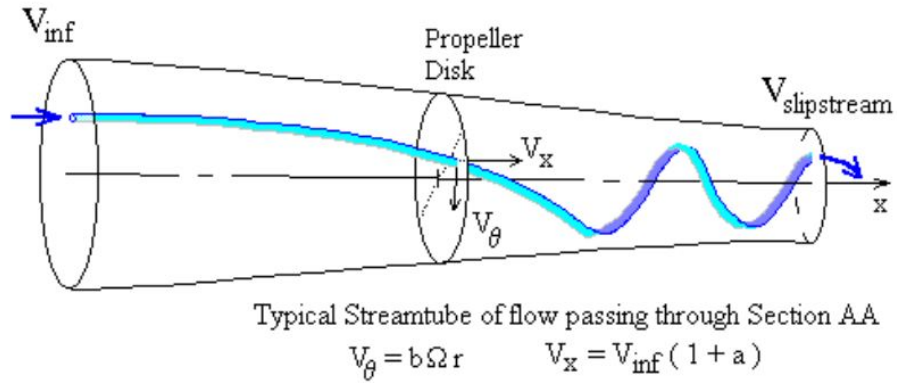
Figure 4.2: The streamtube of the flow that passes over the propeller disc from Ref. [20]

4.2   Blade Element Theory

The aim of Blade Element Theory is to simplify the model of a 3-dimensional flow assuming that it can be seen as a summation of a large number of bidimensional flows. It is assumed that the geometry of the airfoil section along the span is specified. The blade of a propeller is discretized into a number of elements and the flow over each blade element is assumed to be independent of each other. The vortex sheet being shed at the trailing edge of the blade as a helical path is modeled assuming that the flow approaching the propeller disc plane is affected by an induced velocity in both axial and azimuthal directions.

Each small element can be regarded as an airfoil at a particular angle of attack with an infinitesimal width Δr, where r is the radial distance from the hub axis, located at a radial distance between r and $r + \Delta r$. A representative blade element is shown in **Fig. 4.3**
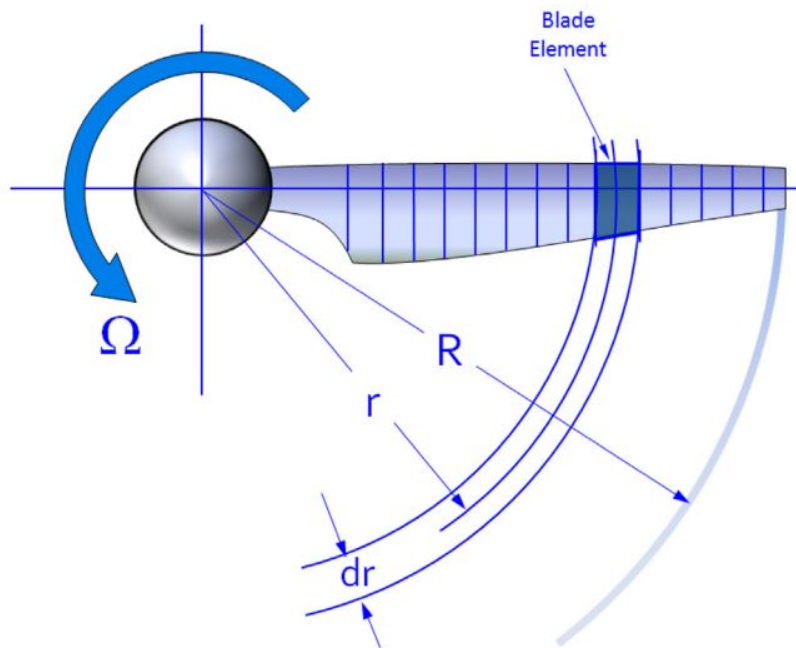
Figure 4.3: Definition of blade element from ref. [24]

The tangential speed of the air seen by the blade is Ωr, where Ω is the angular speed in radians per second of the propeller spinning at n revolution per minute

$$\Omega = 2\pi n/60$$

The propeller is assumed to fly with an axial speed of $V = V_{vehicle}$, which can be seen as a free stream flow velocity. The axial direction is normal to the propeller disk, therefore the resultant velocity seen by the blade element V_R is

$$V_R = \sqrt{V^2 + (\Omega r)^2}$$

Each blade element is subjected to elemental lift ΔL and drag ΔD forces

$$\Delta L = \frac{1}{2}\rho V_{R0}^2 C_l c \Delta r$$

$$\Delta D = \frac{1}{2}\rho V_{R0}^2 c_D c \Delta r$$

where ρ is the fluid density, c is the blade sectional chord of the element, C_l and C_d are the lift and drag coefficients and V_{R0} is the resultant velocity of the fluid as seen by the airfoil. The resultant force

$$\Delta F = \sqrt{\Delta L^2 + \Delta D^2}$$

can be divided into two other different components, an axial component ΔT and an azimuthal component $\Delta Q / r$. The latter, multiplied by the radial distance r, is the elemental torque acting on the blade, whilst the former is the elemental thrust. This corresponds to a little incremental axial velocity induced by the propeller blade, which is a fraction of the speed of the propeller, aV, with the coefficient a lesser than 1, and to a decrement of the azimuthal velocity component $b\Omega r$, as pointing in the direction opposing the azimuthal speed. The axial velocity seen by the blade element is $(1 + a)V$, whereas the azimuthal velocity is $(1 - b)\Omega r$. It follows that the resultant velocity is

$$V_{R0} = \sqrt{(1+a)^2 V^2 + (1-b)^2 (\Omega r)^2}$$

and the angle subtended by the velocity components is defined as the Inflow angle, Φ_0

$$\tan \phi_0 = \frac{(1+a)V}{(1-b)\Omega r}$$

The effective angle of attack of the flow relative to the blade element, as a result of the geometrical blade section pitch β and the wake induction, corresponds to

$$\alpha = \beta - \phi_0$$

25
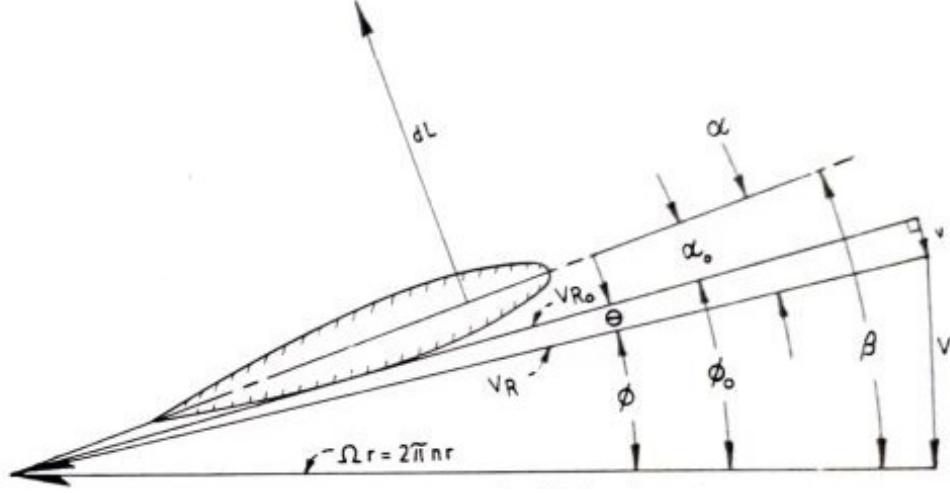
Figure 4.4: Flow past the blade element Ref.[25]

4.3   Blade Element Momentum Theory

The blade element theory and the momentum theory are combined in a blade element momentum theory in order to compute the values of the inflow factors a and b. If a propeller has B blades, the equilibrium for a circular radial element of width Δr reads:

$$\Delta T = 4\pi r \rho V_\infty^2 (1 + a)a\Delta r = \frac{1}{2}\rho_\infty V_{R0}^2 c(c_l \cos\phi_0 - c_d \sin\phi_0)B\Delta r$$

$$\Delta Q = 4\pi r^3 \rho_\infty V_\infty \Omega(1 + a)b\Delta r = \frac{1}{2}\rho_\infty V_{R0}^2 c(c_d \sin\phi_0 + c_l \sin\phi_0)Br\Delta r$$

The sectional lift and drag coefficients, c_l and c_d, are functions of the local angle of attack α, Reynolds, and Mach number. In the present thesis, lift and drag coefficients are extracted from look-up tables generated by XFoil open-source software. X-foil uses a high-order panel method and a fully coupled viscous/inviscid interaction method to evaluate drag, boundary layer transition and separation.

Introducing the radial solidity coefficient $\sigma = cB/(2\pi r)$, the sectional thrust and torque coefficient $c_T = c_l \cos\phi_0 - c_d \sin\phi_0$ and $c_Q = c_d \sin\phi_0 + c_l \sin\phi_0$ and simplifying, it is possible to obtain the following system of algebraic equations:

$$\left(1 - \frac{\sigma}{4}c_T\right)a^2 + \left(1 - \frac{\sigma}{2}c_T\right)a - \frac{\sigma}{4}c_T\left[1 + \frac{\Omega r}{V_\infty}^2(1 - b')^2\right] = 0$$

26

$$b = \frac{\sigma}{4} \frac{V_\infty^2 (1 + a)^2 + \Omega^2 r^2 \left(1 - b'\right)^2}{V_\infty \Omega r} \frac{c_Q}{1 + a}$$

The system is solved with an iteration method: b' denotes the value of b at the previous iteration, while the initial guess values assigned for a and b respectively are 0.2 and 0.1. A relaxation coefficient of 0.3 is used for both a and b, and a is selected as the larger positive root of the second-order equation. This procedure allows a to exceed the unitary value at a low advance ratio [14]. The elemental thrust and torque, integrated along the blade span, provide the overall thrust and torque, which are translated into thrust and torque coefficients C_T and C_Q of the propeller

$$C_T = \frac{T}{\rho_\infty \Omega^2 \pi R_T^4}$$

$$C_Q = \frac{Q}{\rho_\infty \Omega^2 \pi R_T^5}$$

It is important to note that in literature the thrust coefficient and torque coefficient are often expressed in a different non-dimensional form [26]

$$C_T = \frac{T}{\rho_\infty n^2 D^4}$$

$$C_Q = \frac{Q}{\rho_\infty n^2 D^5}$$

where n is the number of revolutions per second of the blades and D denotes the diameter of the propeller. In the first notation, the Power Coefficient

$$C_P = \frac{P}{\rho \Omega^3 \pi R_T^5}$$

is equal to C_Q, because of the definition of shaft power $P = \Omega Q$, and the propeller efficiency is expressed as

$$\eta = \lambda \frac{C_T}{C_P}$$

where $\lambda = V / \Omega R_T$ is the operating ratio in terms of the angular velocity Ω and the propeller radius R_T, in a form that emphasize the tip speed of the propeller.

In the latter case, $C_P = 2\pi C_Q$ and the propeller efficiency is expressed as

$$\eta = J \frac{C_T}{C_P}$$

4.4   Corrections to the BEMT-based model

One of the most important corrections to BEMT analysis is a tip loss correction. The concept of tip loss was introduced by Prandtl to model the loss of circulation near the tip of the blade, typical of a finite wing. The air flows from the region of higher pressure (lower surface) to the region of lower pressure (upper surface), generating a helicoidal vortex sheet responsible for a loss of lift near the tip and induced drag for the blade. The amount of the loss depends on the radial position of the element, on its 2D aerodynamic characteristics, and on the specific inflow angle seen by the element. Prandtl tip loss factor F is used to modify the momentum of the blade element momentum equations [27].

$$F = \frac{2}{\pi} \arccos \left[exp\Big(\frac{-B(R_{tip} - r)}{2r \sin \phi} \Big) \right]$$

$$\Delta T = 4\pi r \rho F V_\infty^2 (1 + a) a \Delta r$$

$$\Delta Q = 4\pi r^3 \rho_\infty F V_\infty \Omega (1 + a) b \Delta r$$

For the case in exam, the sectional lift and drag coefficient are computed from the Xfoil data for the airfoil NACA4412 at Re=50'000. An interpolation is made from $-12°$ to $15°$, with an angular step of $0.5°$.

At Low Advance Ratio, is observed that small scale propellers experience post-stall behavior in correspondence of higher angles of attack. BEMT method has limited accuracy when the 2-D airfoils are at angles of attack beyond stall [28], resulting in the underprediction of the thrust coefficient C_T. In fact, instead of the assumed 2D airfoil flow, the flow over the stalled blade encounters significant radial components, which are reflected in experiments in a higher $c_{L_{MAX}}$ and in thrust, driven largely by the lift coefficient. For this reason, post-stall corrections are included following the Viterna and Corrigan approach [29]. The lift and drag coefficients for angles of attack greater than the stall angle and less than or equal to 90° are computed as follows:

$$C_L = A_1 \sin 2\alpha + A_2 \frac{\cos^2 \alpha}{\sin \alpha}$$

$$C_D = B_1 \sin^2 \alpha + B_2 \cos \alpha$$

where A_1, B_1, A_2 and B_2 are derived as

$$A_1 = \frac{B_1}{2}, \quad B_1 = c_{D_{MAX}}, \quad c_{D_{MAX}} = 1.11 + 0.018AR$$

$$A_2 = (c_{L_s} - c_{D_{MAX}} \sin \alpha_s \cos \alpha_s) \frac{\sin \alpha_s}{\cos^2 \alpha_s}$$

$$B_2 = c_{D_s} - \frac{c_{D_{MAX}} \sin^2 \alpha_s}{\cos \alpha_s}$$

with the parameters at stall denoted with the subscripts s and AR the aspect ratio of the blade, defined with the chord length at r/R=0.75.

At negative angles of attack after $-\alpha_s$ and beyond the range from the $+\alpha_s$ and 90 deg, flat plate theory can be adopted to extrapolate the lift and drag coefficients [30], which adheres more closely to the experimental data in peak regions for both models **(Figure 4.5)**. The principle of the theory is that at angles of attack following fully separated flow, the flow detects only the lower surface of the airfoil, which behaves like a thin flat plate. To maintain the effect of the flow separation, the stagnation point on the rear side of the airfoil is moved assuming potential flow theory behavior. The curve of lift and drag coefficients can be described using the following equations:

$$c_L = 2 \sin \alpha \cos \alpha$$

$$c_D = 2 \sin^2 \alpha$$

Lift coefficients comparison

Drag coefficients comparison
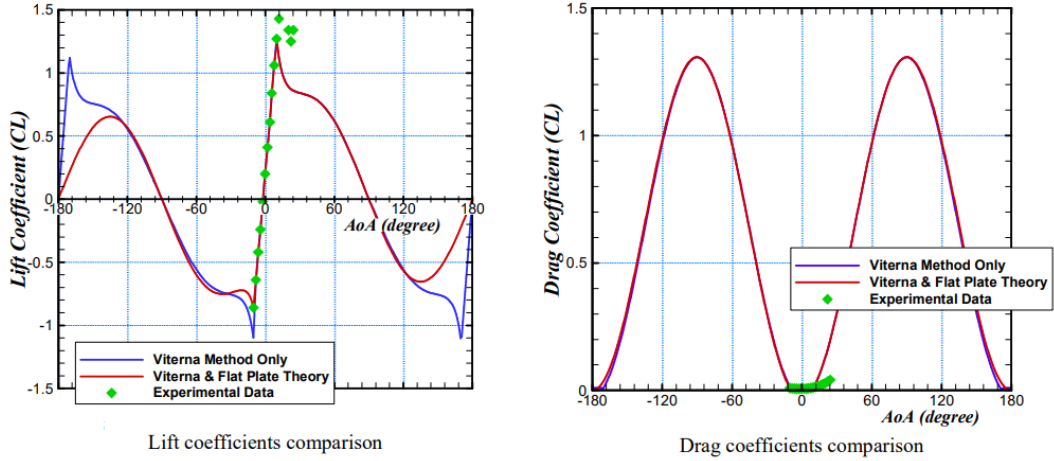
Figure 4.5: NACA 2415 Lift coefficient and drag coefficient from Ref. [30], comparison between Viterna and Flat plate methods

Chapter 5

Aeroacoustics

5.1   Quantifying sound

In this paragraph, a brief introduction about how to describe sound or a sound field is made. Noise is characterized by "pitch", represented by frequency, and "volume", expressed by the amplitude of the sound wave [31]. To describe the amplitude of a sound the root mean square (rms) of the time average pressure $\overline{p}$ is considered:

$$p_{rms} = \overline{p}^{1/2}$$

This measure suffers from the problem that acoustic pressures of interest vary over a huge range. The threshold of human hearing is at $p_{rms} = 20\mu Pa$ while the thresholds of pain and beginning of hearing damage are at $p_{rms} \approx 200mPa$, covering a range of seven orders of magnitude. Therefore, a logarithmic scale is used to manage the obtained values. On this scale, the difference between two acoustic pressures p_1 and p_2 is measured in *Sound Pressure Level*

$$\Delta SPL = 10 \log_{10} \frac{\overline{p_1^2}}{\overline{p_2^2}}$$

When only one pressure signal needs to be expressed, it is captured with respect to the minimum threshold of human hearing $p_{ref} = 20\mu Pa$, defined as the standard reference sound pressure:

$$SPL = 10 \ \log_{10} \frac{\overline{p_1^2}}{p_{ref}^2}$$

The Sound Pressure Level can be referred to a specific frequency range or to an entire spectrum. If the complete spectrum is sampled, the Sound Pressure Level converges with the Overall Sound Pressure Level (OASPL).

Level/dB	Example
140	3m from a jet engine
130	Threshold of pain
120	Rock concert
110	Accelerating motorcycle at 5m
80	Vacuum cleaner
60	Two people talking
10	3m from human breathing

Table 5.1: Some sample approximate noise levels from Ref. [31]

The human frequency range of audibility goes from 16 Hz to 18 kHz. Because human ears are more sensitive to a specific range of frequencies (1 KHz-5 KHz) of those constituting a sound signal, frequency-based curves were created to describe the sound characteristics considering the response of human ears to pure steady tones. A typical expedient for environmental and industrial noise is the application of the A-weighting decibel filter (dbA) to the sound pressure level. It is commonly employed adding listed values by octave or third-octave bands to the measured (or computed) sound pressure levels in dB. It is employed by arithmetically adding a table of values, listed by octave or third-octave bands, to the measured sound pressure levels in dB. The numerical quantities are obtained from the 40-phon Fletcher–Munson curve of equal loudness and reported in the blue curve of **Fig.5.1**. Another noise evaluation metric frequently used is the *A-weighted Equivalent Sound Pressure Level L_{Aeq}* (**Fig.5.2**). It represents the time-averaged measure of the sound pressure level on a period of interest, converted into decibels and frequency weighted in dBA.

$$L_{Aeq} = 10 \log_{10} \frac{1}{t_M} \int_0^{t_M} \left(\frac{p_A(t)}{p_0} \right)^2 dt$$

Commission Delegated Regulation (EU) 2019/945 [4] refers to *Sound Power Level L_{WA}* (dBA) as a measure to compare different UAV designs. The value is obtained by frequency weighting in dBA

$$L_W = 10 \log_{10} \frac{P}{P_{w0}}$$

where P is sound power in watt (W), given for a medium by $P = \frac{Ap^2}{\rho c} \cos\theta$. A represents the area of a surface in m^2, ρ (kg/m^3) and c (m/s) are the mass density

and the sound velocity of the medium, θ is the angle between the direction of propagation of the sound and the normal to the surface and p is the sound pressure in Pa. The reference sound power $P_{W0} = 10^{-12}W$ is equivalent to the threshold of hearing.

5.2   Noise prediction

The direct approach to predict aerodynamic noise consists in the tridimensional and unsteady solution of the Navier-Stokes equations for a compressible flow. Noise corresponds to the part of the field that dominates at great distances from the region occupied by the fluid flow. To simplify the approach, one should think to linearize the equations, nevertheless, for a generic propagation medium, it presents difficulties due to the complex structure of the equations that does not allow the application of the linear acoustic techniques. Moreover, the solution of the equations in waveform contains acoustic fluctuations as well as fluctuations of a different nature. In order to use an analytical approach, approximations should be introduced. For these reasons, aeroacoustics analogies have been proposed, in which the fluid mechanics equations are combined in a wave equation for a homogeneous resting medium. The knowledge of the main features of the flow is necessary for this purpose. [32]
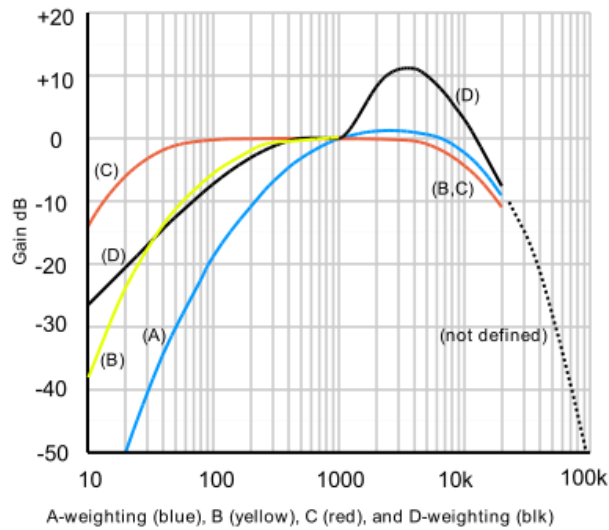
Figure 5.1: A-weighting decibel filter compared to various weighting curves
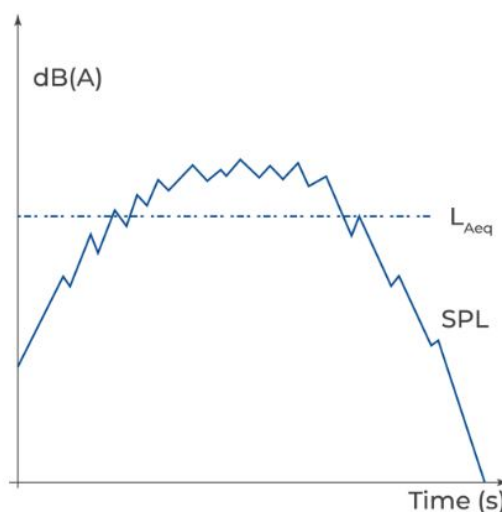
Figure 5.2: A-weighting decibel filter compared to various weighting curves

5.3 Acoustic Radiator Models

In aeroacoustic analogies, sound sources are reduced to simple emitter types. The simplest of these is the monopole or pulsating sphere, which represents a small sphere whose radius alternately expands and contracts, where the variation of mass outflow from the source generates a non-directional sound.

The next simplest elementary solution is the dipole, which consists of two monopole sources of equal strenght but opposite phase, positioned at a small distance compared to the wavelength from each other. An acoustic dipole is comparable to a force applied in a point and varied in magnitude and/or direction. A dipole does not radiate sound equally in all directions. Its directivity pattern has maxima along the 0° and 180° directions, and no sound radiation along the 90° and 270° directions. An example of dipole noise is noise due to propeller thrust.

Momentum transport appears in the appropriate acoustic equation in two parts: one represent direct convection of the momentum component by the velocity component; the other part is the stress between adjoining elements of fluid. The latter part can be represented by a quadrupole, since an element of fluid under stress is subject to equal and opposite forces on opposite sides, each force could be equivalent to a dipole and each pair to a quadrupole. The quadrupole exhibith a symmetrical four-lobed pattern. A turbulent jet is an example of quadrupole noise source.

Decreasing efficiencies of radiation at the lower frequencies are caused by cancellation effects in the dipole and quadrupole. For example, assuming a sphere

deforming at a frequency having a wavelength of twice the circumference of the sphere, the efficiency of a dipole relative to this simple source is 1/3, whereas the quadrupole is characterized by a relative efficiency of 1/1000.
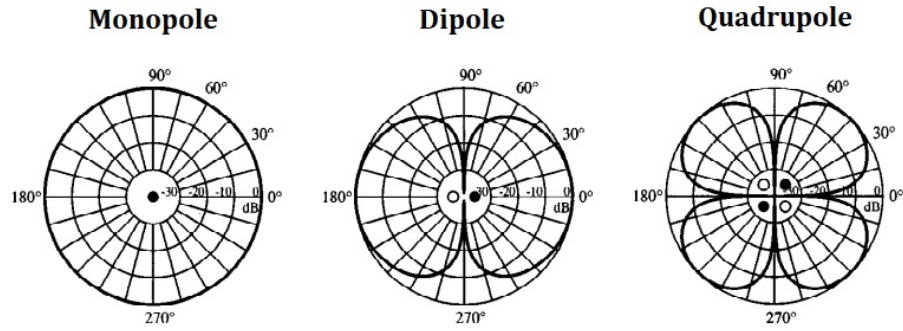
Figure 5.3: Acoustic source types

Chapter 6

Sources of Aerodynamic Noise for propellers

Aerodynamic noise is defined as sound generated as a direct result of relative motion between a solid body or stream of fluid and the surrounding medium. [33] The spectrum associated to a rotating blade has been traditionally separated in two components: the periodic noise and the broadband noise.

The periodic noise is so called because its time signature can be represented by a pulse that repeats at a constant rate. When an ideal propeller with a specific number of blades, denoted as B, is spinning at a constant rotational speed, represented by N, it produces noise that can be perceived as a signal with a fundamental frequency equal to the number of blades times the rotational frequency (NB), called Blade Passage Frequency, The blade-passage period is 1/BN. Typically the generated pulse is not a pure sinusoid: many harmonics occur at integer multiples of the fundamental frequency. The first harmonic is the fundamental frequency, the second harmonic occurs at twice the fundamental frequency, and so on.

Broadband noise contains components at all frequencies, It is visualized as a continuous frequency spectrum, with a shape caused by different amplitudes. For rotating blades, broadband noise describes the modulated sound produced by the unsteady pressure field associated with vortices shed from the trailing edge and tips of the blades, together with noise related to turbulence effects in the air stream. Sources of aerodynamic noise for propellers at low Reynolds Number are structured as shown in **Fig. 6.1**

6.1 Rotational noise

Considering blades as real rotating airfoils with a thickness, the pressure distribution around profiles is moving relative to the surrounding medium. This pressure
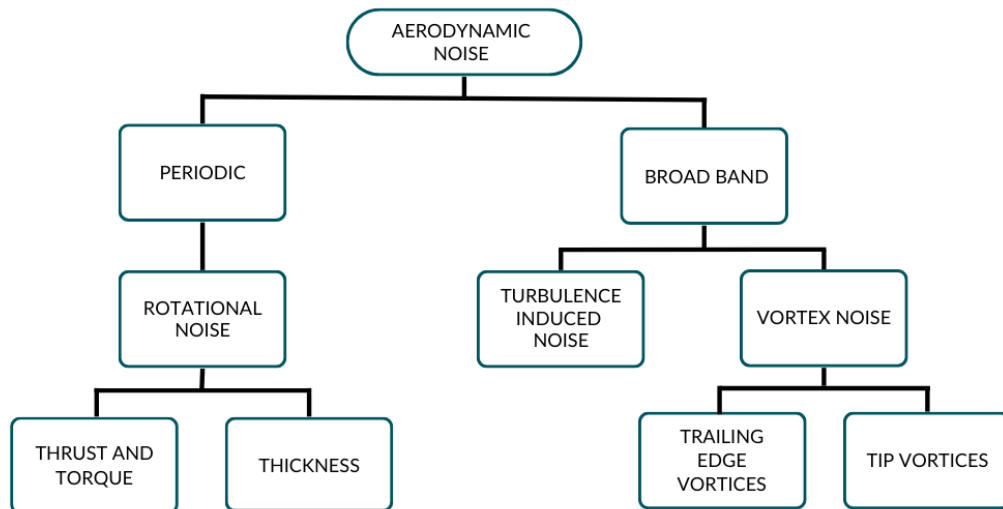
Figure 6.1: Sources of aerodynamic noise for propellers

distribution can be decomposed in a thrust component normal to the plane of rotation and a torque component in the plane of rotation. As a consequence of the Newton's third law, the air in contact with the propeller has a force on it which can be resolved into the thrust and torque vectors. The pressure field on air is steady relative to the blade and rotates with it if the operating condition of uniform inflow is present. Analytically, rotating airfoils generating loading noise may be visualized as an array of stationary dipole sources in the rotor disc activated during blade passage.

In addition, an element of air in the disc is moved aside at the blade passage by the finite thickness of the blade. In a fixed frame of reference, this displacement can be seen as a periodic injection and removal of mass at each air element close to the disc. The rate of mass introduction in a point can be assumed as a simple source, and it depends on the blade profile, incidence and speed. Up to Mach tip speed approaching sonic values, thickness noise is generally small compared with the noise arising with torque and thrust. At higher tip speeds it may assume more importance.

6.2   Vortex noise

The dominant source of broadband noise for propellers is called vortex noise, defined as "that sound which is generated by the formation and shedding of vortices in

the flow past a blade". For the most simple case of an infinite circular cylinder normal to the flow, vortex shedding occurs in the range of Reynolds numbers from 10^2 to 10^5 as an orderly vortex street, described by cylinder diameter and flow velocity. For rotating airfoils with a thickness the process is similar, and because of the different velocities of every chordwise station along the span, it results in a broad band of shedding frequencies. Analytically, it can be schematized as a dipole source whose strength is proportional to the sixth power of the section velocity. Moreover, it is found that the frequencies associated with the area near the tip tend to be of the greatest amplitude. In addition, tip and spanwise vorticity of strength proportional to the generated thrust gradients is produced and shed. This dipole acoustic radiation, combined with that from the trailing edge vortices, constitutes the vortex noise.

In flow fields containing shear layers such as boundary layers, random noise is produced directly by the motion of small scale turbulence. This sound has a quadrupole nature, so it is inefficiently radiated. Unfortunately, it is amplified by the interaction with the pressure field of the moving blade, being translated into more efficient dipole sources. [33] At moderate tip speed, slightly below the effect of compressibility effects, both vortex noise and rotational noise due to thickness are lower than the rotational noise due to thrust and torque. However, in recent studies dealing with the reduction of overall propeller noise, vortex noise is found to be an important contributor.

6.3 Attenuation

Loss of energy during sound propagation in homogeneous air is mainly due to three factors. The first one is the geometric distance between the source and the observer: considering a spherical wave spreading from a point source of uniform intensity, the sound pressure level registered at the observer position varies inversely to the square of the distance from the source. In a first-order approximation, this relation is valid even for non-point sources in the far-field, defined as multiples of the propeller diameter. In terms of logarithmic decibel scale, the sound pressure level falls by 6 dB doubling the distance from the source. The second and third factors deal with atmosphere attenuation. A mechanism is called classical absorption, it regards losses from radiation, viscosity, heat conduction and diffusion, and it is proportional to the square of the sound frequency. However, in the audible range of frequencies, classical absorption has lesser importance than molecular relaxation in the air, function of humidity and frequency. Atmospheric turbulence and wind gradients can also be significant factors.

Chapter 7

Helicoidal Surface Theory

7.1 Acoustic models for propellers

During the past century, many different acoustic models have described the noise emission of propellers. The first and simplest propeller noise prediction model was developed by Gutin, who analyzed the sound produced by a two-bladed airplane propeller. Gutin's frequency-domain model represents the noise emission with a single noise source at the propeller hub. The sound pressure of the specific harmonic order is related to the integrated thrust and the power consumption. At the same time, the geometry of the propeller is included exclusively through the propeller diameter and the blade number. Further important parameters are the tip Mach number, the only representative of the operation condition; the observer-to-hub distance; and the angle between the propeller axis and the observer vector, pointing from the propeller hub to the observer. Noise cancellation effects are simulated through the Bessel function. The field of application of his model was restricted to a limited number of propeller blades ($B < 5$), limited harmonics ($m < 6$), and limited blade tip Mach numbers ($0.3 < M_t > 0.8$) In the 1950s, noise modeling made a significant step forward due to the acoustic wave analogy derived by Lighthill [34]. Subsequently, the Ffowcs-William Hawkings (FW-H) equations described the noise radiation of arbitrary motions of surfaces in a fluid. The FW-H equations require as input unsteady flow quantities, generally derived by unsteady Reynolds Averaged Navier-Stokes (URANS) solvers. The consideration of pressure time history on surfaces ensures a high level of accuracy in noise prediction, together with high-quality aerodynamic data and the computation of retarded blade location for propellers. However, unsteady Computational Fluid Dynamics (CFD) simulation and Computational Aeroacoustic (CAA) methods are demanding and extremely time-consuming. [35, 36] As a result, frequency methods developed in early acoustic theories are considered a valid option in design and optimization

studies, given their proven satisfactory performance, even in the absence of accurate details regarding the propeller geometry lost through the Fourier transform of the wave equation. [37]

7.2 Helicoidal Surface Theory

Hanson proposed a frequency domain method that explicitly displays many of the design variables [38] [39]. Helicoidal Surface Theory is based on Goldstein's version of the acoustic analogy, in which the generation of sound in a moving medium in the presence of solid boundaries is described with three integrals

$$c_0^2 \rho'(x,t) = -\int_{-T}^{T} \int_{A(\tau)} \rho_0 V_n \frac{\partial G}{\partial \tau} dA(y) d\tau + \int_{-T}^{T} \int_{A(\tau)} f_i \frac{\partial G}{y_i} dA(y) d\tau + \int_{-T}^{T} \int_{V(\tau)} T_{ij} \frac{\partial^2 G}{\partial y_i \partial y_i} dy d\tau$$

V_n is the normal surface velocity and defines the monopole source, f_i is the i-th component of the force per unit area exerted by the fluid on the boundaries and represents the dipole source, T_{ij} is Lighthill's stress tensor without the viscosity contribute $\rho u_i u_j + (p - c_0^2 \rho')\delta_{ij}$ and designates the quadrupole source. c_0 and ρ_0 denote respectively the speed of sound and the density in a quiescent fluid, ρ' is the acoustic density disturbance, G is the Green's function, $A(\tau)$ constitutes the impermeable surfaces at the emission time τ which bounds the region $v(\tau)$. The integration is performed over the source time τ in a range $\pm T$.

Hanson assumed that the loading and thickness sources act on the advanced helix, which is the surface swept by a radial line that rotates at a certain angular speed and moves forward with the flight speed. In the Helicoidal Surface Theory, the source strengths take account of the real blade geometry, but the surface boundary conditions are satisfied on a mean surface according to the thin wing approximation. Furthermore, the quadrupole source is omitted, ignoring the nonlinear effects at high Mach numbers. Axial inflow is assumed in the present dissertation to obtain a simplified mathematical expression to describe the steady tonal noise components of the propeller, namely loading noise and thickness noise.

Acoustic pressure can be expressed as an infinite sum over harmonics of the blade passing frequency

$$p(t) = 2Re\left[\sum_{m=1}^{\infty} P_{mB} exp(-imB\Omega_D t)\right]$$

where P_{mB} is the Fourier transform of the pressure at the mth harmonic of the BPF, *Re* refers to the real part of the Fourier coefficients, B is the number of blades. The summation is performed for positive harmonics numbers and the first factor

is used to account for the negative harmonics. Ω_D is the frequency related to the angular speed with the Doppler effect accounted

$$\Omega_D = \frac{\Omega}{(1 - M_x \cos\theta)}$$

Ω is the angular speed, M_x is the axial Mach number, θ is the angle between propeller axis and the observer. Forward flight is included in Hanson's model in the form of Doppler effect

$$Dop = \frac{1}{1 - M \cos\theta_{ret}}$$

It is necessary to say a few words about the current reference system to explain the meaning of the term θ_{ret}. In [39] reference is made to a source moving at speed V, while the observer position and the fluid are fixed with the reference system. Consequently, the visual source position is defined as the position at the time the sound is heard, while the retarded source position, θ_{ret}, represents the location of the source when it produced the sound heard at the present time. The retarded radiation angle is shown in **Fig. 7.1** and is defined as

$$\cos\theta_{ret} = \cos\theta\sqrt{1 - M^2 \sin^2\theta} + \sin^2\theta$$

In **Fig. 7.2** the relationship between the visual angle and the retarded angle is depicted, showing that the flight mach number M plays a central role in differentiating the two parameters.

The noise harmonic P_{mB} can be written as the sum of different contributions $p_{mB} = p_{Vm} + p_{Lm} + p_{Dm}$ where the components are due to

- p_{Vm} volume displacement or thickness component

- p_{Lm} lift component of the loading noise

- p_{Dm} drag component of the loading noise

The noise contributions can be calculated using the following equations derived in [38] and [39]. The implementation of far-field equations is justified when the distance from the observer to the propeller is multiple of the propeller diameter.

$$p_{mV} = -Dop \cdot \frac{\rho c^2 B \sin(\theta_{ret}) exp\left[imB\left(\frac{\omega_D r}{c} - \frac{\pi}{2}\right)\right]}{8\pi \frac{|O1|}{D}}$$
$$\cdot \int_{hub}^{tip} M_i^2 exp[i(\phi_0 - \phi_S)] \cdot J_{mb}(x_B) \cdot (k_x^2 t_b \Psi_V(kx)) \, dr_n \tag{7.1}$$
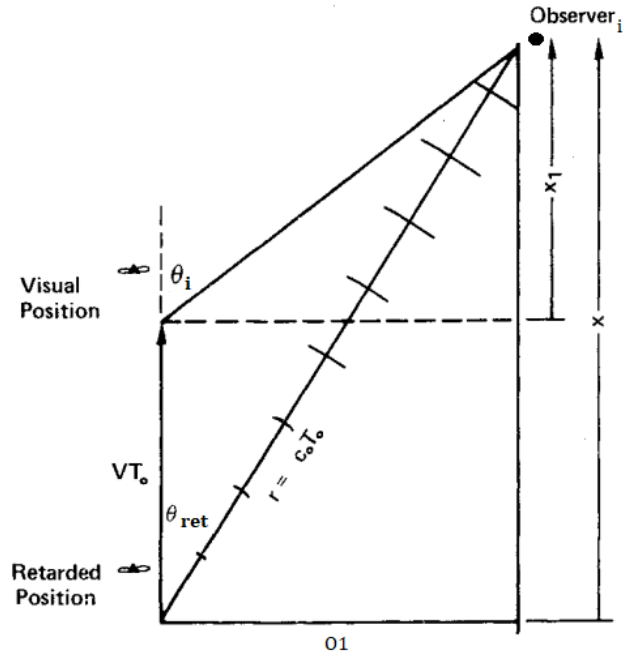
Figure 7.1: Sketch of retarded and visual angle
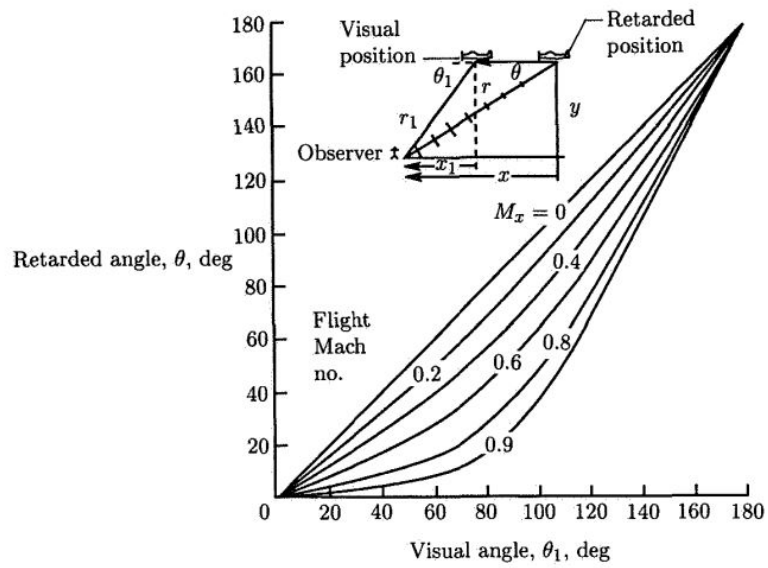
Figure 7.2: Relationship between visual and retarded angle

$$p_{mL} = -Dop \cdot \frac{\rho c^2 B \sin(\theta_{ret}) exp\left[imB\left(\frac{\omega_D r}{c} - \frac{\pi}{2}\right)\right]}{8\pi \frac{|O1|}{D}}$$

$$\cdot \int_{hub}^{tip} M_i^2 exp[i(\phi_0 - \phi_S)] \cdot J_{mB}(x_B) \cdot \left(-k_y \frac{c_L}{2} \Psi_L(kx)\right) dr_n$$

$$(7.2)$$

$$p_{mD} = -Dop \cdot \frac{\rho c^2 B \sin(\theta_{ret}) exp\left[imB\left(\frac{\omega_D r}{c} - \frac{\pi}{2}\right)\right]}{8\pi \frac{|O1|}{D}}$$

$$\cdot \int_{hub}^{tip} M_i^2 exp[i(\phi_0 - \phi_S)] \cdot J_{mB}(x_B) \cdot \left(k_x \frac{c_D}{2} \Psi_D(kx)\right) dr_n$$

$$(7.3)$$

Hanson describes the noise resulting from the acting forces lift and drag and the displacement or volume V noise of each blade element. The lift and the drag force are replaced by the blade section lift and drag coefficients C_L and C_D. O1 is the sideline (or vertical) distance between the observer position and the propeller axis, r is the distance from the hub of the propeller to the observer point, D is the propeller diameter, t_b is the maximum thickness to chord ratio and is dependent on the airfoil selected for each the blade sections. The non-dimensional wave numbers k_x and k_y are defined as

$$k_x = Dop \cdot \frac{2mB}{M_r} \cdot b_c M_t$$

$$k_y = Dop \cdot \frac{2mB}{M_r} \cdot \frac{b_c}{r_n} \cdot (M_r^2 \cos\theta_{ret} - M_x)$$

where b_c is the chord-to-diameter ratio and the different subscripts of the Mach numbers designate

- M_x flight Mach number, $M_x = V_\infty/c_0$

- M_t tip rotational Mach number, $M_t = \Omega \cdot R_{tip}/c_0$

- M_r effective Mach number, dependent on the radial normalized position $x = r/R$, $M_r = \sqrt{M_x^2 + x^2 M_T^2}$

The aeroacoustic non-compactness is considered in the functions Ψ_v, Ψ_D, and Ψ_L of k_x, in order to describe the influence of thickness, drag, and lift distribution from the leading edge to the trailing edge of every section. The exact form of the distributions should be inserted after performing a normalization step, in such a

way that the maximum value of $H(x)$ is 1, while $f_D(x)$ and $f_L(x)$ are normalized for unit area.

$$\Psi_V(k_x) = \int_{-0.5}^{0.5} H(x)e^{ik_x x}dx$$

$$\Psi_D(k_x) = \int_{-0.5}^{0.5} f_D(x)e^{ik_x x}dx$$

$$\Psi_L(k_x) = \int_{-0.5}^{0.5} f_L(x)e^{ik_x x}dx$$

As per Hanson's suggestion [40], a parabolic thickness distribution and a uniform shape for lift and drag could be employed if it is not necessary to investigate the proper configuration of load coefficients and thickness along the chord, resulting in the following implementation, accurate enough for a low harmonic order analysis.

$$\Psi_V(k_x) = \begin{cases} 2/3 & \text{for } k_x = 0 \\ \frac{8}{k_x^2}\left[\frac{2}{k_x}\sin\frac{k_x}{2} - \cos\frac{k_x}{2} \right] & \text{for } k_x \neq 0 \end{cases}$$

$$\Psi_L(k_x) = \begin{cases} 1 & \text{for } k_x = 0 \\ \frac{2}{k_x}\sin\frac{kx}{2} & \text{for } k_x \neq 0 \end{cases}$$

$$\Psi_D(k_x) = \begin{cases} 1 & \text{for } k_x = 0 \\ \frac{2}{k_x}\sin\frac{kx}{2} & \text{for } k_x \neq 0 \end{cases}$$

Propeller sweep and lean influence the phase shift of the propeller section noise emission. The latter acts weakly usually, but it will mentioned for the sake of completeness. They could be taken into account by the factors mid-chord alignment MCA and the face alignment FA. The former describes the displacement of the radial station in the direction of the chord, while the latter constitutes the displacement in the axis direction. The displacements are defined as the local position of the mid-chord point relative to the propeller fixed coordinate system. Therefore, the equations for the phase lags are the following.

$$\Phi_S = Dop \cdot \frac{2mB}{M_r} \cdot M_t \cdot \frac{MCA}{D}$$

$$\Phi_0 = Dop \cdot \frac{2mB}{M_r} \cdot \frac{1}{rn} \cdot (M_r \cos\theta_{ret} - M_x) \cdot \frac{FA}{D}$$
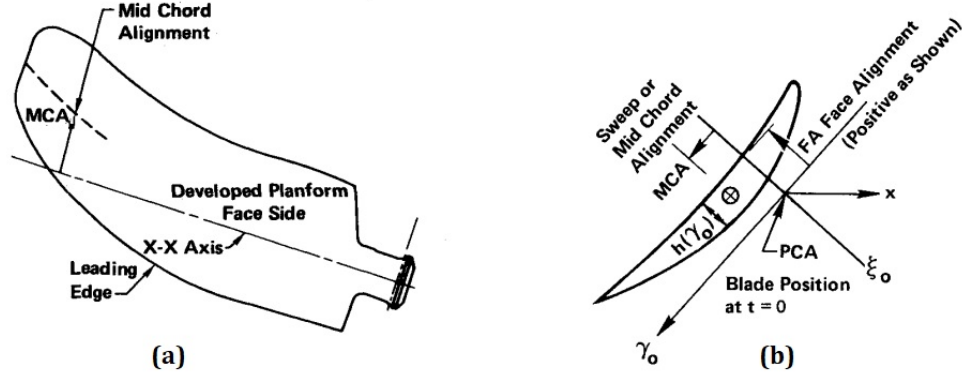
Figure 7.3: Mid-chord alignment (a) and Face alignment (b) from Ref. [38]

The radiation efficiency role is performed by the factor J_{mB}, which represents the Bessel function of the first kind of argument x_H and order mB, expounded in (**Fig.7.4**) for a generic x and contained in the MATLAB function 'besselj'. The Bessel function is valued for each section of the blade. The argument of the function in the Helicoidal surface theory is

$$x_H = Dop \cdot mBr M_t sin(\theta_{ret})$$

An additional precaution is given in [40] about the lift and drag coefficients that should be used in this acoustic model. In fact, the lift and drag forces should be defined as the sectional local components acting parallel and perpendicular to the local advance direction, as depicted in Fig. **Fig.7.5**. Therefore, the effect of the induced flow components on the resultant velocity vector and in the description of the angle of attack should not be considered. With reference to the parameters defined in Section 4.2 and in Figure 4.4, the shift in coefficients is computed as follows, where Θ is the induced angle :

$$C_L = \frac{V_{R0}^2}{V_\infty^2 + (\Omega r)^2}(C_l' \cos\Theta - C_d' \sin\Theta)$$

$$C_D = \frac{V_{R0}^2}{V_\infty^2 + (\Omega r)^2}(C_l' \sin\Theta - C_d' \cos\Theta)$$
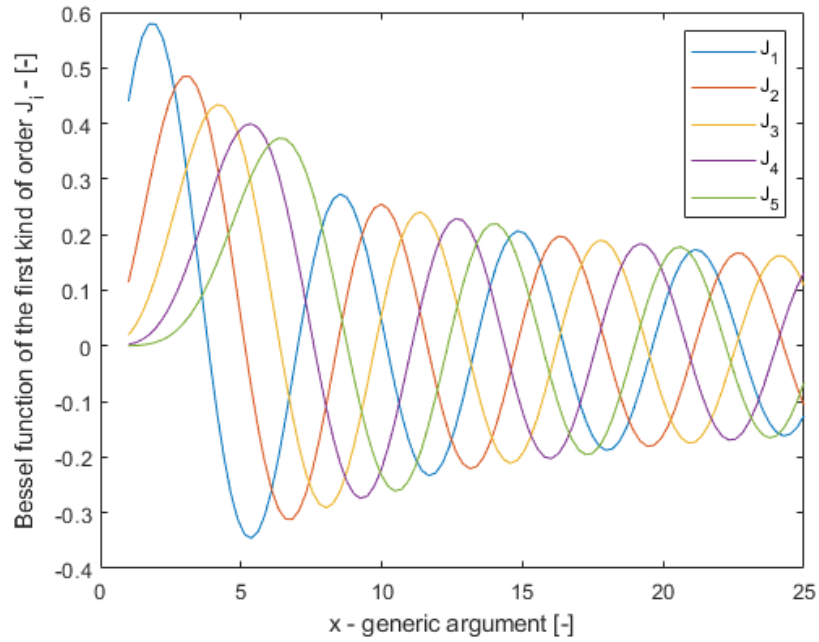
Figure 7.4: Bessel function of the first kind
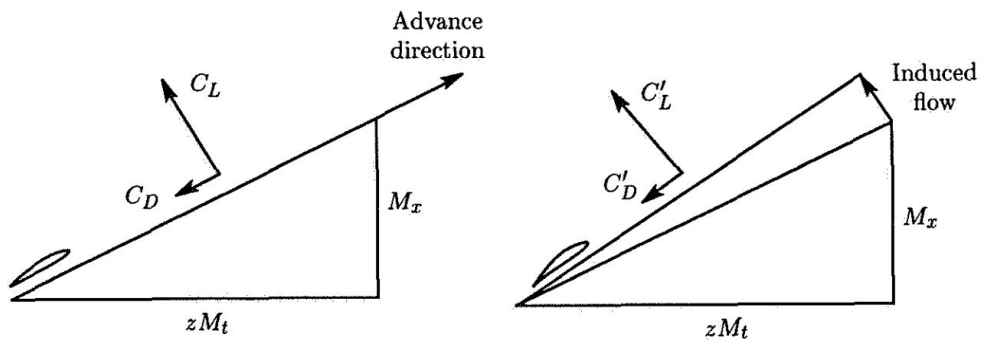
Figure 7.5: Reference axes for lift and drag definition from [40]

Chapter 8

Methodology

8.1   Sensitivity Studies in Literature Review

A search for sensitivity studies in the literature is conducted to determine the optimization variables among the parameters that describe a propeller and the propeller blade. Most of the literature that deals with propeller performance does not include results for low advance ratios. Benedict et al. [41] tested more than 30 different airfoil sections, which included high-performance low Reynolds number airfoils (such as Eppler-63, FX-63, AH-7-47-6, etc.,) and conventional airfoil sections for a MAV-scale helicopter rotor. The ones with the lower thickness-to-chord ratio and moderate camber (4.5 % to 6.5 % in **Fig. 8.1**) produced the highest rotor figure of merit and significantly higher Cl/Cd. The figure of merit of the baseline rotor varied from 0.45 while using a NACA0012 blade section up to 0.59 for a thin circular cambered plate (max camber= 6.1 %, $t/c = 2.3\%$).

Chusseau et al. [42] carried out a parametrical study analysing the influence of the number of blades, diameter, and shape of a light aircraft propeller. At constant shaft power and rotation speed, thrust, torque and the efficiency of the propeller are calculated for each geometry modification. The variation in thrust is presented as the most significant parameter to track the performance evolution. A first observation is done by scaling the blade of a factor a , therefore modifying the diameter and the chord. The reduction of the blade scale leads to excessive blade loading so the propeller efficiency falls. If simultaneously the number of blades is increased to carry an identical load, the thrust of the single blade decreases by about -60 N (**Fig.8.2**). A large number of blades provides a rise in the drag force, as a consequence the thrust and the propeller efficiency decrease.

In the same work, in order to modify the spanwise repartition of the loads, the chord distribution is changed. The taper ratio is altered by increasing the chord value at the root (at station 20 %) of a percentage of the chord length and a
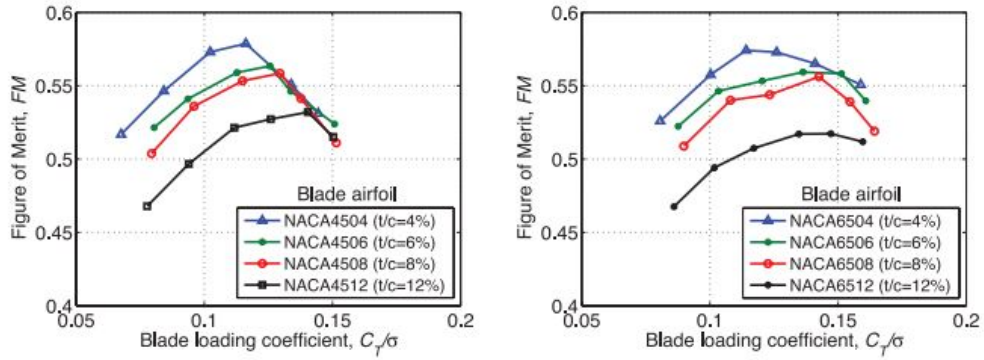
a) 4.5% circular camber and varying thickness to chord **b)** 6.5% circular camber and varying thickness to chord ratios.

Figure 8.1: Influence of section thickness-to-chord ratios in Figure of Merit vs blade loading coefficient for Micro Air Vehicles in Hover [41]
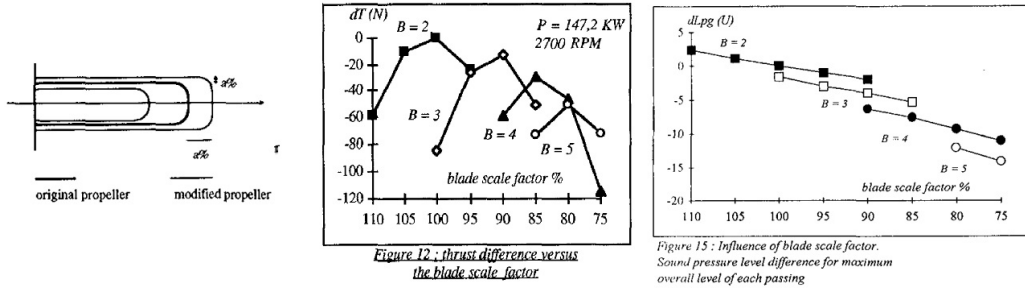
Figure 8.2: Influence of number of blades and blade scale factor on thrust and sound pressure level from [42]

reduction at the tip of the same percentage, realizing a spanwise modification that is a linear combination of the two parts, as shown in **Fig. 8.3**. The chord reduction near the tips leads to lower drag at the blade tip. Due to constant absorbed shaft power, the pitch angle and the total thrust outcomes are more important. As a consequence, the loads of the blade move toward the hub. In addition, the increased chord near the hub positively affects the root structural stresses.

As regards the aeroacoustic effects, the variation in the number of blades affects the relative contributions of each source component. An increase in propeller surface area results in more surface in motion, consequently leading to an increase in thickness noise. On the other hand, the best repartition of the loads on each blade gives a weaker loading noise. Therefore, the maximum radiated sound pressure level decreases with a larger number of blades (**Fig.8.2**), reaching -15 dB with five blades.

47
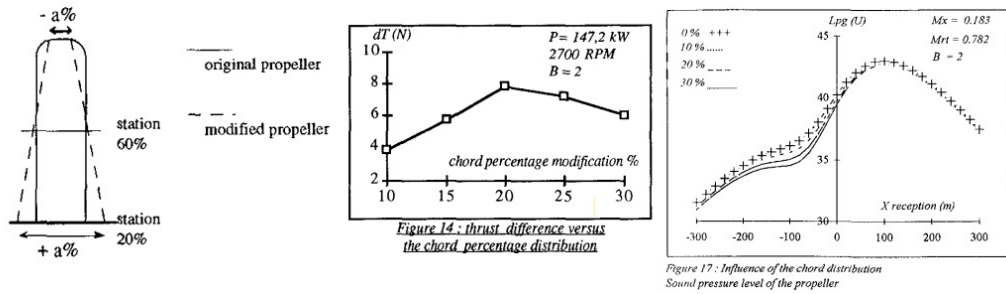
Figure 8.3: Influence of chord distribution on thrust and sound pressure level from [42]

If the increase in the number of blades is connected to a size diminution, the thickness noise diminishes with the scale factor but increases with the number of blades. On the other hand, the loading noise decreases for each modification. The diminution of both the chord and the diameter leads to a lower tip Mach number and lower surface in motion: all these modifications have a positive effect on sound generation.

The same modification of the chord applied for aerodynamic studies is applied for acoustic calculation. Both tip and root modifications have two opposite effects: the positive one, created by the new spanwise distribution of the loads towards the hub, partially disappears due to the increased loads; so the new chord distribution has no influence on the loading noise. On the other hand, the thickness noise decreases. The chord change from the middle of the blade to the tip provides a slight improvement in the loading noise.

Hanson [43] concluded that decreasing diameter, reducing tip speed, and increasing the number of blades are all effective but have strong impacts on aerodynamic efficiency. Therefore the work was addressed in the effect of non-acoustic compactness related to parameters like airfoil section shape, sweep, twist and chords distributions in different operating conditions. For the following consideration we are referring at the lower tip rotational Mach (0.6), proper of the condition of Large Conventional propeller at takeoff. The only recommendation for thickness noise for straight blades is to minimize the area of the blade while staying within structural and aerodynamic bounds. A swept blade has two effects on propeller noise: the former is the reduction of the quadrupole source strength related to transonic compressibility, which is not the case of interest in the present dissertation, since it is expected to find a Mach number in every section of the blade lower than 0.3; the latter is to cause destructive interference between signals from different radii. The same outcome related to phases might be achieved to a lesser extent by an offset of the blade, defined as bending the blade perpendicular to the chord.
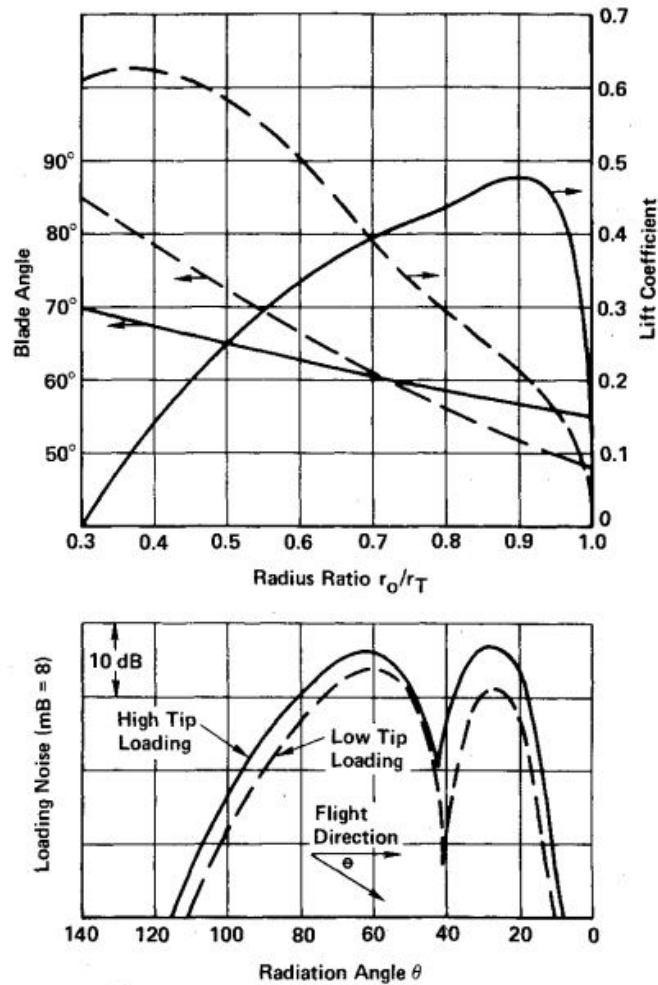
Figure 8.4: Influence of twist distribution on tonal noise from [39]

Considering that varying the angle of attack in a range of ten degrees could lead from zero lift to stall, necessarily small changes in twist can cause large changes in radial load distribution. The difference in loading noise in **Fig. 8.4** shows the acoustic benefits of relocating the load away from the high-speed portion of the blade. Noise can be decreased by 3 dB by moving the load inboard to a radius where it radiates less efficiently. However, the loss in aerodynamic efficiencies must be considered.

Thickness noise is proportional to the cross-sectional area of the propeller: Geyer et al [44] and Feng Huanhuan et al [45] proved that the thickness of airfoils with the same curvature has a strong impact on the generation of tonal noise at Low Reynolds Number. The increase in airfoil thickness could enlarge pressure

fluctuation and produce a larger scale of vortices. As a consequence, the tone noise gradually disappears from the sound pressure level spectrum and the noise spectrum displays broadband features. In addition, data analysis shows that the generation of tone noise is closely related to the vortex shedding of the trailing edge of the airfoil.

Given the complexity of the framework, in this study we preferred to prioritize our focus initially on the effect of the chord distribution and the variation of the twist along the span, as suggested by Hanson, setting as constant the number of blades and the propeller diameter.

8.2   Baseline propeller geometry

The blade taken as a baseline is firstly acquired from the CAD model of a rotor widely tested in the A-Tunnel of TU-Delft. It derives from a two–blade propeller APC 9×6, namely with a diameter of 9 in (22.86 cm) and a pitch of 6 in (15.24 cm). The diameter of the propeller has been scaled up to D=30 cm, the radius of the hub is 1.25 cm, and each profile has been reshaped with an NACA 4412 airfoil, suitable for low Reynolds number flow and low advance ratio of the propeller [46].
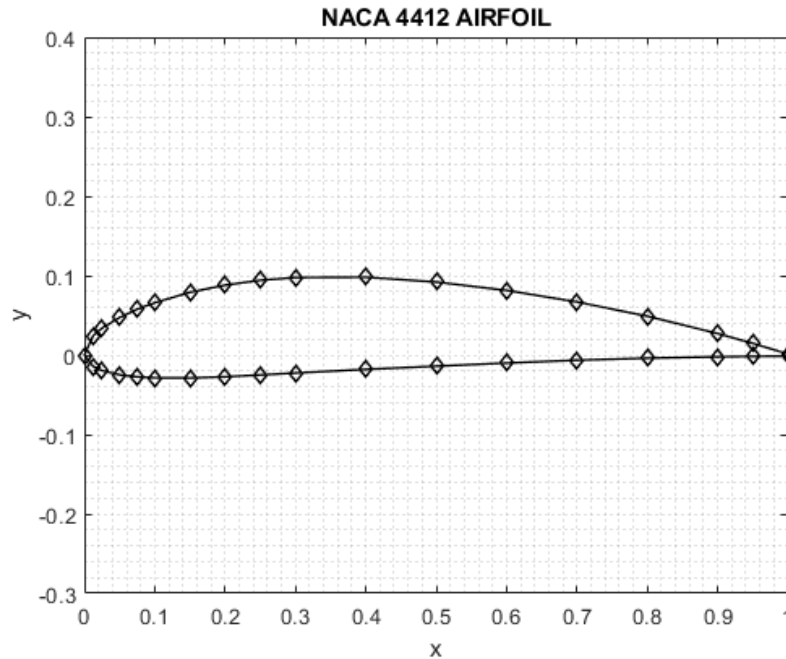
Figure 8.5: Airfoil NACA 4412

The NACA 4412 is a four-digit airfoil: the first digit expresses the camber in

percent chord, the second digit gives the location of the maximum camber point in tenths of chord, and the last two digits give the thickness in percent chord. Thus the selected airfoil manifests a moderate maximum camber of 4% of chord, located at 40% chord back from the leading edge, and results to be 12% thick.

This airfoil is recognized as convenient for low advance ratios because the propeller is expected to be in a highly stalled condition. Hence, an opportune airfoil shape should exhibit not only a large CL_{max} to achieve a high thrust level but also a significant lift coefficient at larger angles of attack.

The blade is further reshaped to obtain a third-degree polynomial interpolation in four points to describe the radial twist law; while, for the chord-length distribution, a second-degree polynomial interpolation in three points is used. The first aerodynamic section is taken at a normalized radius $r/R = 0.222$. The three points for the chord interpolation in the sense of minimum squares are collocated at the normalized radial stations $r/R = 0.222$, $r/R = 0.344$, and $r/R = 1$; while the four points for the cubic interpolation are taken at $r/R = 0.222$, $r/R = 0.344$, $r/R = 0.7627$ and $r/R = 1$. These points represent the nearest stations at the data set in the quarter and at three-quarters of the working length of the blade.
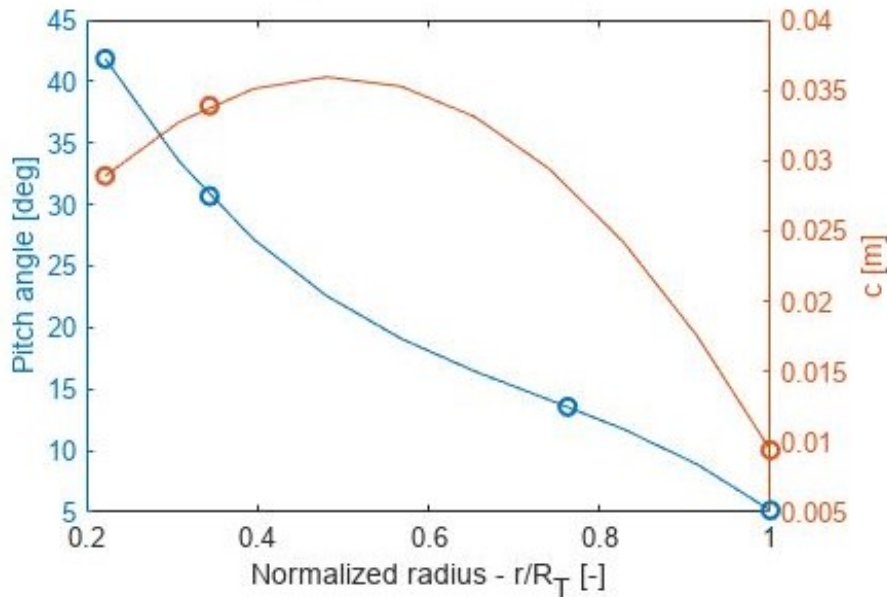
Figure 8.6: Chord and twist distribution of the baseline blade

The coefficients of the polynomials found by the described interpolations are written in the following distributions, stating that x is the normalized radius $x = r/R$ and $0.222 \leq x \leq 1$:

$$c(x) = -0.1006x^2 + 0.0979x + 0.0121$$
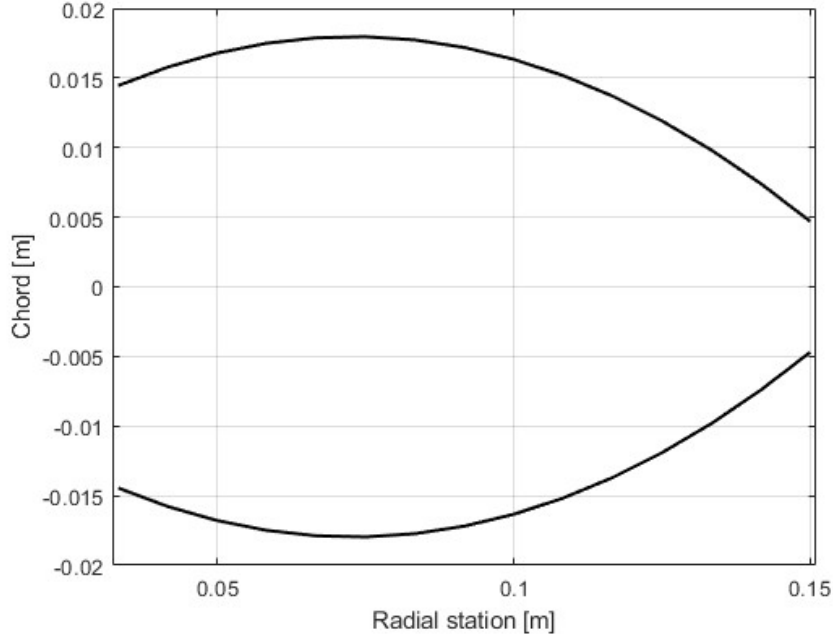
Figure 8.7: Blade planform of the baseline propeller

$$\beta(x) = -109.3502x^3 + 238.6695x^2 - 199.8027x + 75.6259$$

The values of the coefficients will be scaled later in order to create new blade designs, in which the search for the optimum geometry can be operated. For that purpose, the polynomial distributions found will be presented as

$$c(x) = p_{c2}x^2 + p_{c1}x + p_{c0}$$

$$\beta(x) = p_{\beta3}x^3 + p_{\beta2}x^2 + p_{\beta1}x + p_{\beta0}$$

The maximum chord length of the obtained distribution is $c_{max} = 3.5$ cm, while the maximum twist angle is $\beta_{max} = 41.8$ deg (**Figures 8.6 8.7**).

It is important to mention that the blade is fully defined if the Leading Edge location of each section is determined. Instead of providing this information, the center-chord line is given, since the mid-chord alignment is required for the tonal noise prediction. Hence, all the blade sections are considered aligned to the first one with respect to the mid-chord point, resulting in a symmetrical planform.

8.3 Input parameters and operative conditions

Once the geometrical parameters with significant aerodynamic and aeroacoustic contributions for the optimization of a UAV propeller have been selected for this

study, it becomes necessary to define the remaining dimensional features of the baseline propeller that remain unchanged and summarize the characteristics of the operational condition to analyze, as well as the acoustic setup of observers.

- Two-blade propeller B=2

- Blade radius R_{tip}=0.15 m

- A single airfoil for every blade section (NACA 4412)

- Aerodynamic data for a single Reynolds number $Re = 5x10^4$ are employed at the first instance

- Constant propeller rotational speed n=4000 RPM

- Freestream axial velocity $V_0 = 0.001 m/s - 20 m/s$, with focus on the 2m/s case (J=0.1) in the optimization to analyze the operative condition at Very Low Advance Ratio

Reference atmospheric conditions are considered as indicated by EASA Guidelines on Noise Measurement of Unmanned Aircraft Systems Lighter than 600 kg. [5]

- sea level atmospheric pressure of 101325 Pa;

- ambient air temperature of 25° C

8.3.1 Setting for the aeroacoustic predictions

The acoustic prediction is configured with 15 observers in the xy plane arranged in an arc, from 11.25 deg to 168.75 deg with respect to the propeller axis, at 2m distance from the propeller hub (**Fig.8.8**). Observers along the propeller axis are avoided in the computation of the average Sound Pressure Level, because the too-large values of the SPL for Matlab representation (*-Inf*) inhibit the calculation of the average. In deciBel scale (*-Inf*) represents the complete absence of sound, modeled in the Bessel function as explained in the following section. In the low fidelity approach, the influence of the propeller holding structure is not taken into account, as well as the diameter of the jet nozzle that provides the uniform flow condition. These represent fundamental precautions for any experimental setup.
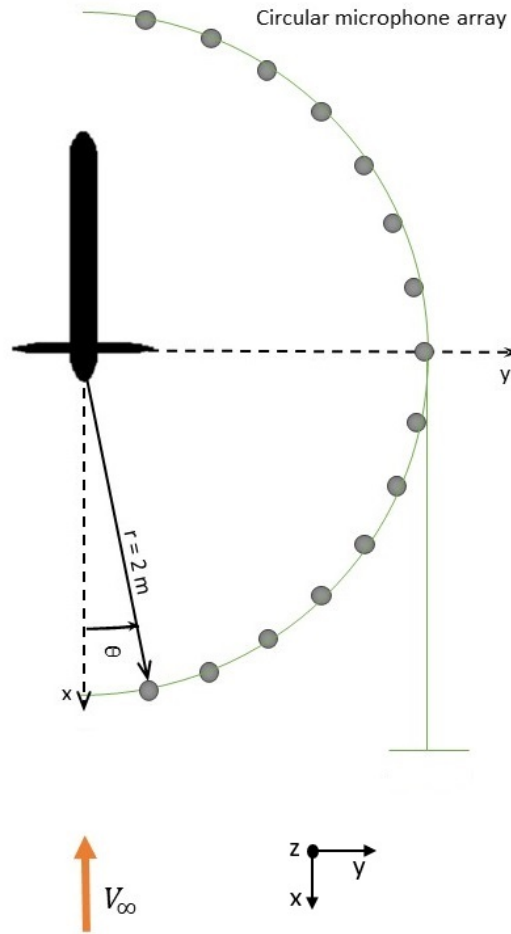
Figure 8.8: Observer locations for aeroacoustic predictions

#	Angle from propeller axis [deg]
-	0
1	11.25
2	22.50
3	33.75
4	45
5	56.25
6	67.50
7	78.75
8	90
9	101.25
10	112.50
11	123.75
12	135
13	146.25
14	157.50
15	168.75
-	180

Table 8.1: Angular location of the observers from the axis of the propeller

8.4   Aerodynamic study

Each blade of the propeller is divided into a set of 15 elements. The BEMT analysis is conducted for eleven different axial velocities in the range $V_0 = 0.001 m/s - 20 m/s$ at 4000 rpm, so the Mach number at the tip of the propeller results in $M_t = 0.1832$.

For the considered advance ratios, the lift coefficient stays in the range from -0.6 to 1.5 (**Fig. 8.12**) and the angle of attack distribution varies between -12 deg and 35 deg, shown in **Fig. 8.11**. The largest variation in the curves occurs for very low advance ratio (J≈0, J=0.1) near the hub, specifically from r/R_T =0.22 to r/R_T=0.4, when the angle of attack is included between 15° and 35°, as expected from the behavior of the aerodynamic curves for post-stall angles of attack at Re=50'000. (**Fig. 8.14**). Therefore, the inner part of the blade at low advance ratios represents an entire stalled region, as evidenced by the very high drag coefficients. (**Fig.8.13**).

Because of the stall, the required torque at low advance ratios is nearly constant at a maximum value. At J=0.3, when the angle of attack over the blade is inferior to the stall angle, and thus the drag coefficients assume more regular values, the torque needed to spin the propeller starts to decrease (**Fig.8.10**). The maximum thrust coefficient occurs in the condition very close to hovering (**Fig.8.9**), as expected, where a thrust of T=4.55 N is achieved. Hence, a mass of 464 grams can be lifted.

The propeller efficiency at 4000 rpm is depicted in **Fig. 8.15**, reaching a maximum value of $\eta = 0.64$ at J=0.5. The propeller is characterized by a figure of merit in hover condition equal to 0.58, while the figure of merit calculated for various advance ratios is illustrated in **Fig. 8.16**.

Table 8.2 reports the performance parameters of the propeller at J=0.1. **Fig. 8.18** and **Fig. 8.19** show the elemental thrust and the elemental torque radial distribution at J=0.1, while in **Fig.8.17** geometric, inflow and attack angles at J=0.1 are illustrated.

Thrust	Torque	Power	Efficiency	Ct	Cq	FM
4.24 N	0.1001 Nm	41.78 W	0.2030	0.0124	0.0020	0.5027

Table 8.2: Performance parameters for the baseline propeller at J=0.1 (freestream axial velocity V=2 m/s and 4000 rpm)
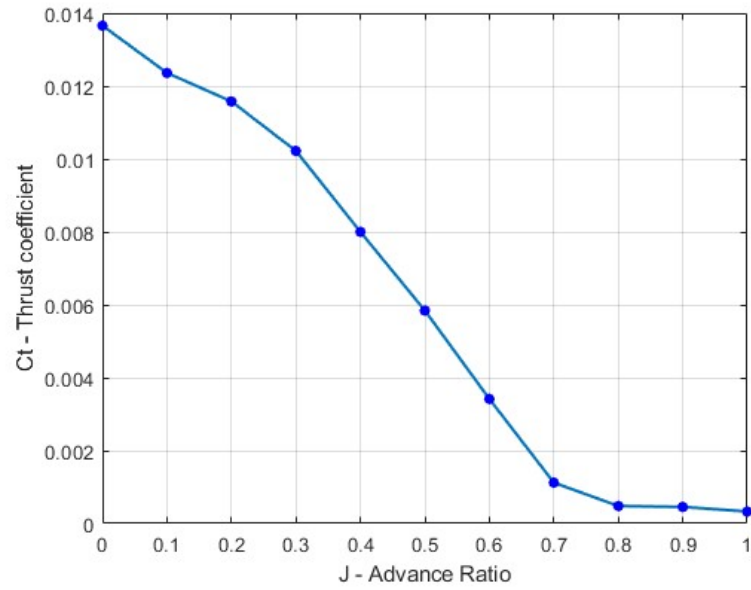
Figure 8.9: Thrust coefficient at different advance ratio
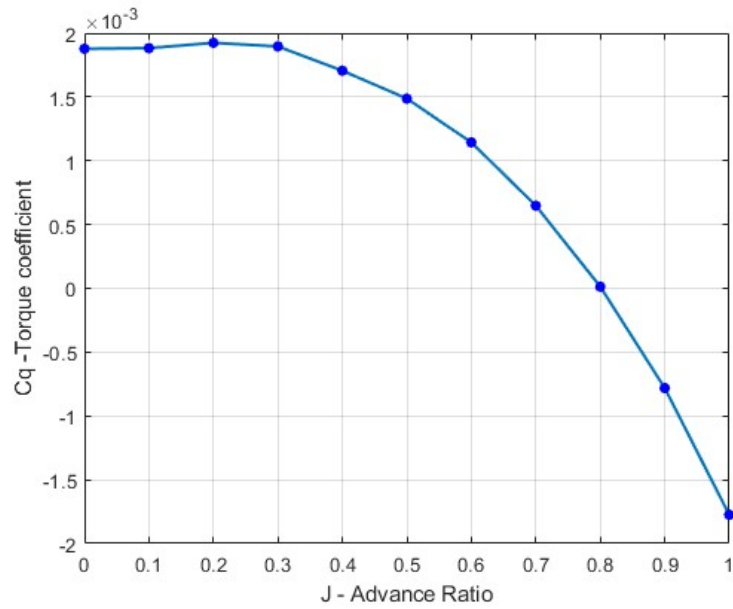
Figure 8.10: Torque coefficient at different advance ratio
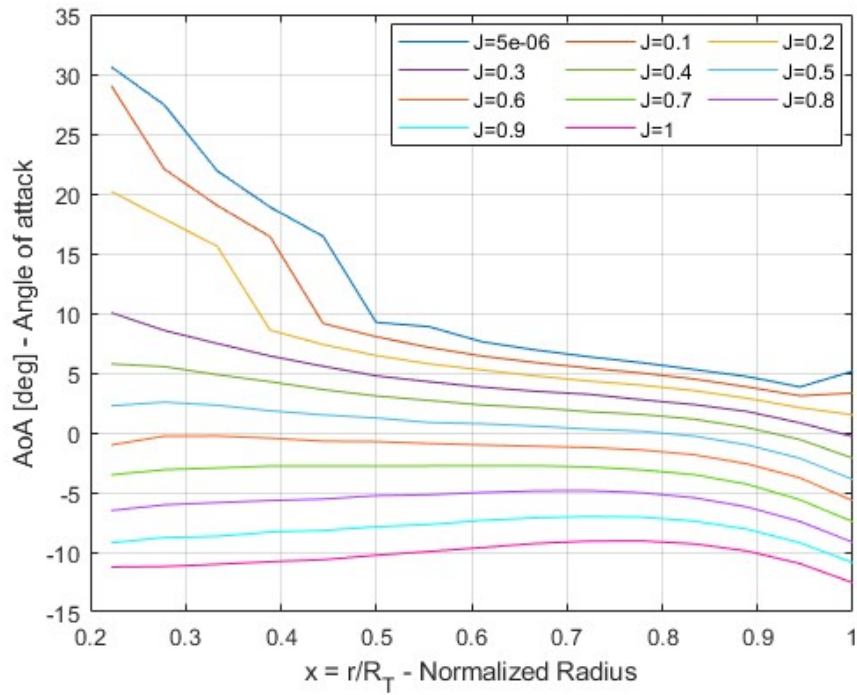
Figure 8.11: Angle of attack distributions for different Advance Ratios
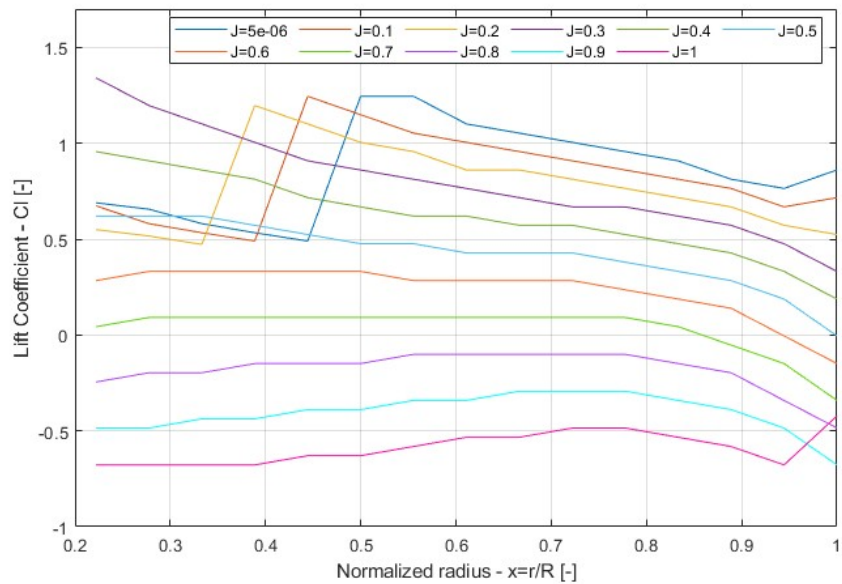
Figure 8.12: Lift coefficient distribution for different Advance Ratios
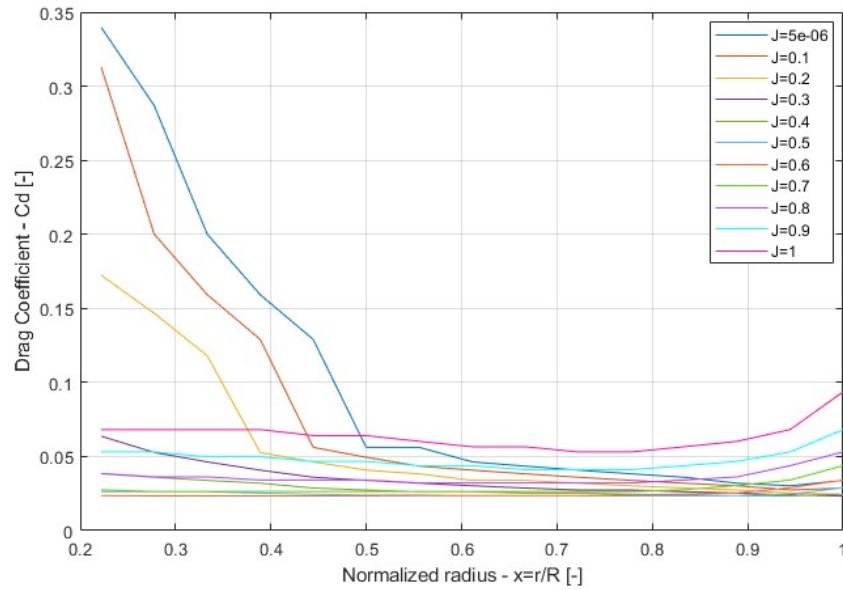
Figure 8.13: Drag coefficient distribution for different Advance Ratios
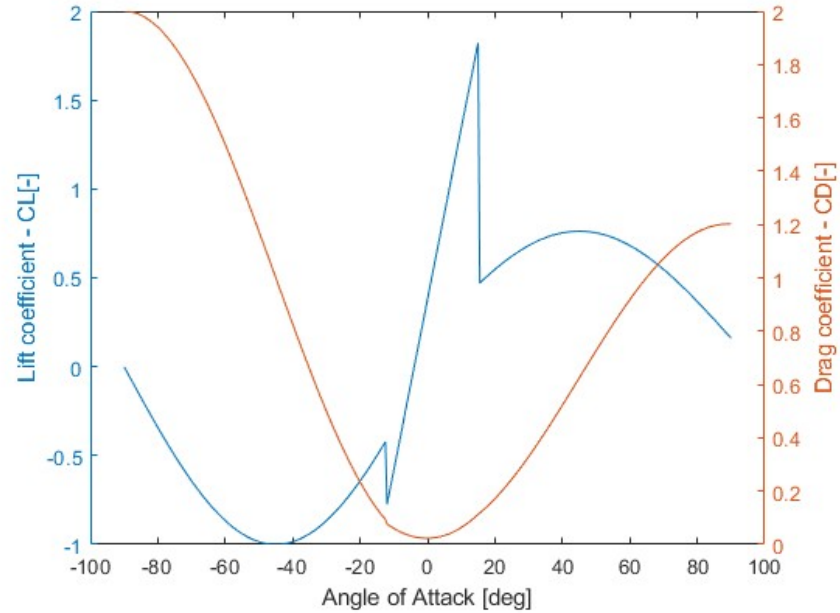
Figure 8.14: Aerodynamic coefficients for NACA 4412 airfoil at Re=50,000 with Post stall and flat plate correction ad described in Chapter 3
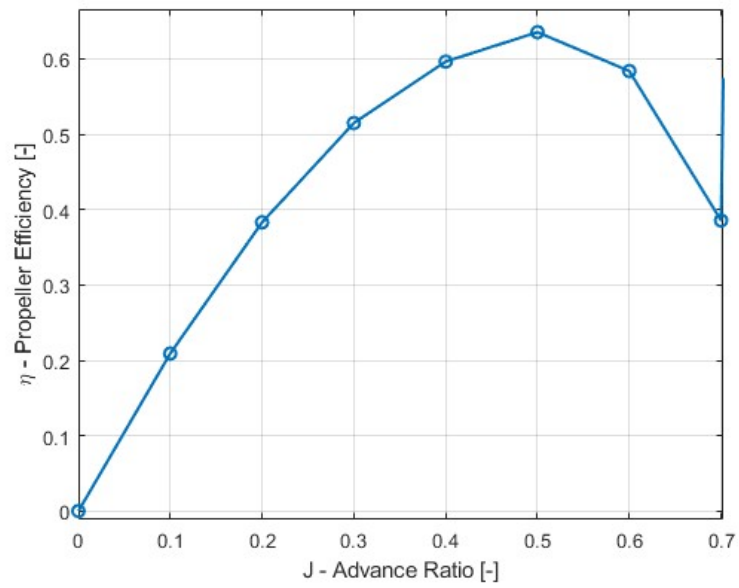
Figure 8.15: Propeller efficiency at different Advance Ratios
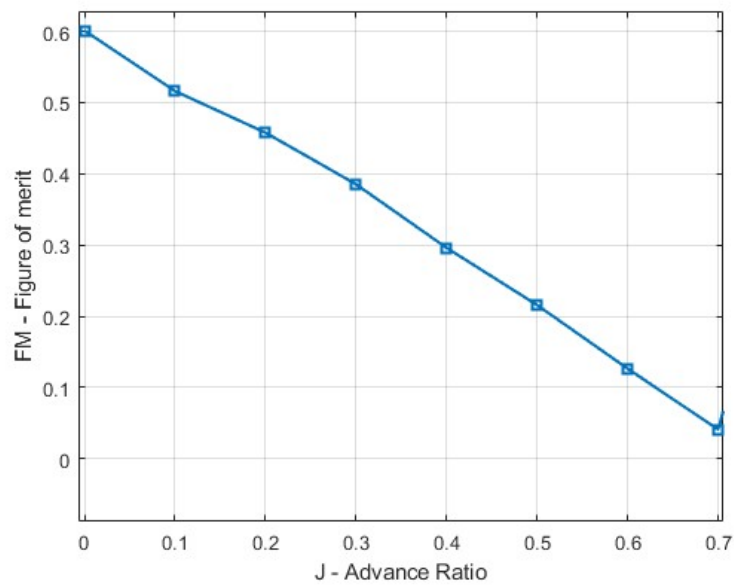
Figure 8.16: Propeller figure of merit calculated at different advance ratio
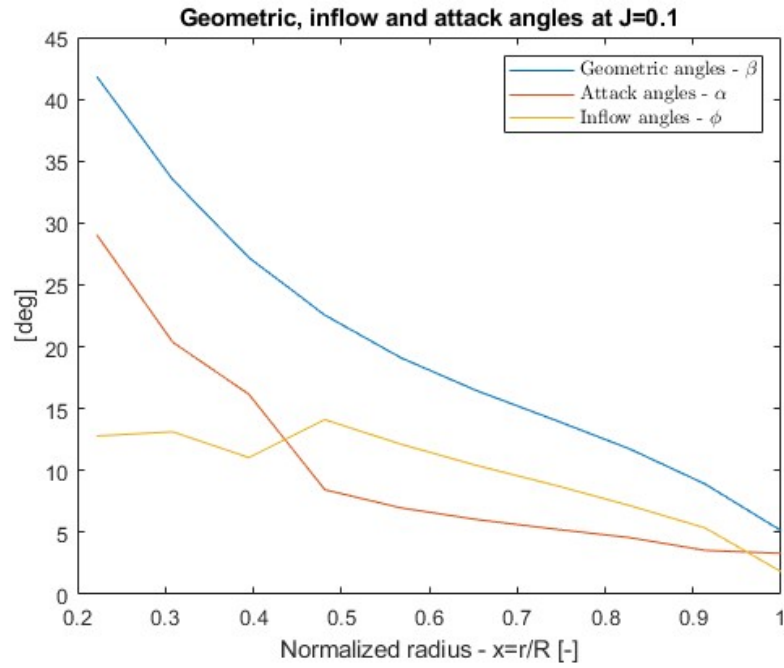
Figure 8.17: Geometric, inflow and attack angles at J=0.1
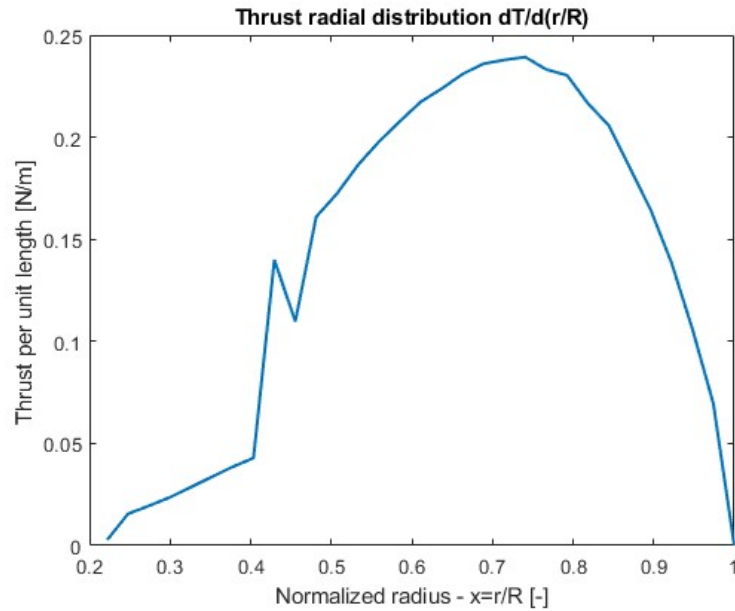
Figure 8.18: Thrust radial distribution at J=0.1
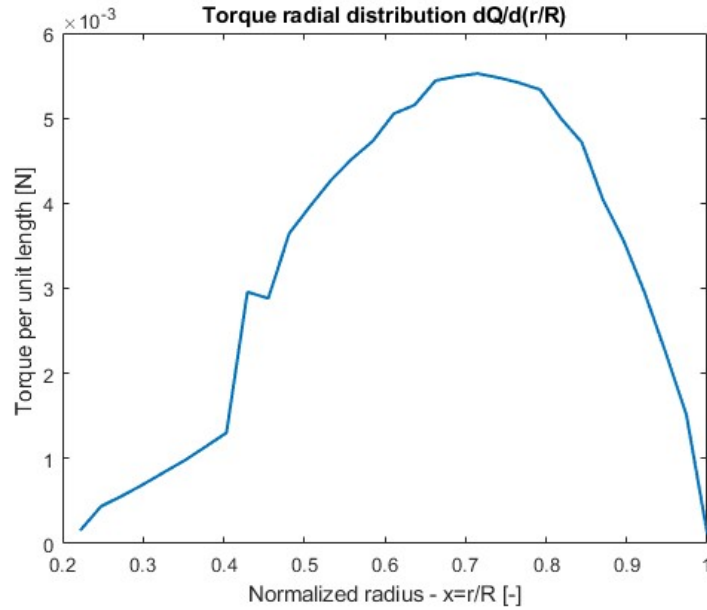
Figure 8.19: Torque radial distribution at J=0.1

8.5   Aeroacoustic study

In this paragraph, the Sound Pressure Level perceived by observers at frequencies of 1 BPF, 2 BPF, and 3 BPF, as well as the Overall Sound Pressure Level, is analyzed. The noise at 2 BPF remains approximately 30 dB lower compared to the noise at the blade passing frequency. The output at 3 BPF is the last detected between the harmonics and assumes values between -10^{-1} and -10^{-2} dB, therefore it does not appear in the images, prioritizing the study of the trends of the various noise components.

The thickness noise curve (**Fig.8.20**) and the drag noise contribution (**Fig.8.21**) appear to have a maximum at a directivity angle of 90 deg, equivalent with the propeller plane, as expected from the radiation efficiency pattern proper of the $\sin\theta$ term of the Bessel function J_{Bm}. In the same way, the noise declines rapidly toward the front and the rear axis of the propeller. The lift component (**Fig.8.22**) of the loading noise shows a two-lobe pattern configuration, with a node at the angle $\theta = 67.5$ deg. In fact, Hanson noise model predicts effectively the decrease in the frontal lobe of the loading noise with the increase of the advance ratio. [47] The location of the node depends on the operating conditions of the propeller. In the far-field model of Hanson, these information are contained in the adimensional wavenumber k_y, proper of the lift term of pressure noise, which hosts the

numerator $M_r^2 \cos\theta_{ret} - M_x$, where M_r is the section Mach number and M_x is the axial Mach number. Hence, for a blade element, the node is located at an angle $M_r^2 \cos\theta_{ret} - M_x = 0$. [39].

From **Fig. 8.23** it is visible the effect of destructive interference in the frontal lobe and constructive interference in the backward lobe of loading noise. The frontal lobe of the lift noise interferes destructively with the drag noise, while the backward lobe interferes constructively. [47]. This asymmetry is caused by the constructive interference between loading perpendicular to the propeller plane (which radiates equally above and below the rotor plane, but with opposite phase) and the loading in the plane of the rotor (which, driven by the motion of the source, radiates with equal amplitude and the same phase above and below the rotor plane). In the present case, the dominant source of loading noise is the drag noise.

The analogous interference pattern is visible for the dipole configuration of the loading noise and the monopole source of thickness noise **(Fig. 8.24)**. Furthermore, because of the low advance ratio, the thickness noise is an important source of noise, enough to mitigate the backward directivity of the overall tonal noise (**Fig. 8.25**) . Investigation of the noise components at different advance ratio is provided in **Fig.8.26**. The inspection of the tonal noise curve at J=0.1 indicates that the maximum far-field SPL of 57.93 dB occurs at a directivity angle of 101 deg.
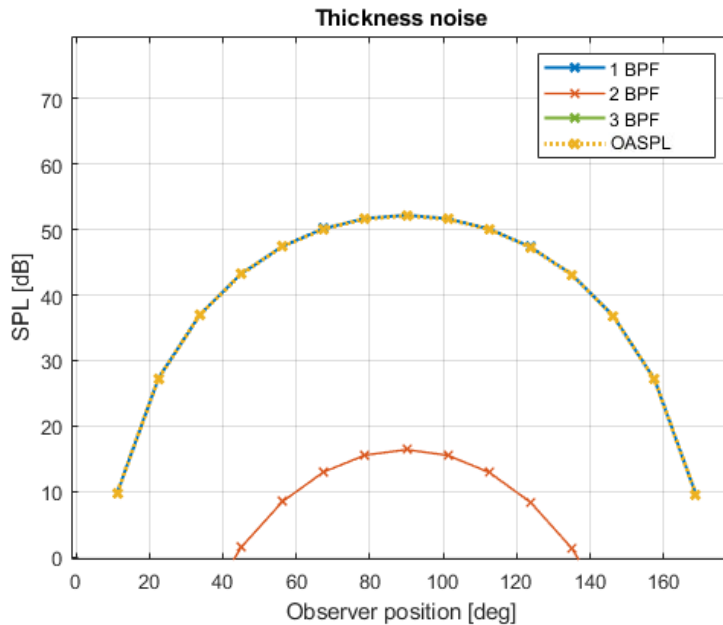
Figure 8.20: Thickness noise
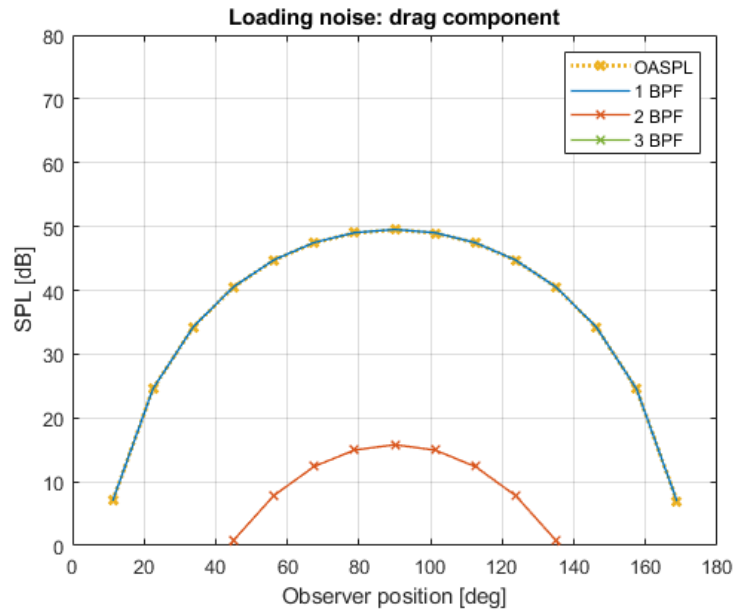
Figure 8.21: Drag noise
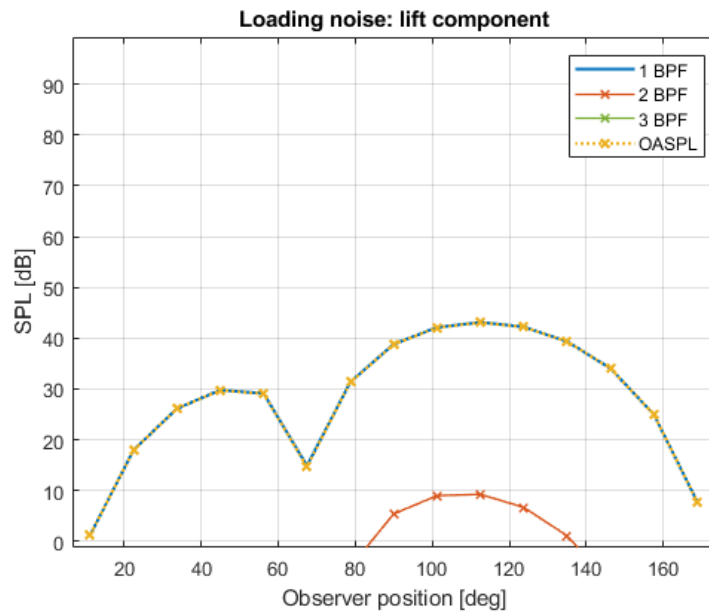
Figure 8.22: Lift noise

63
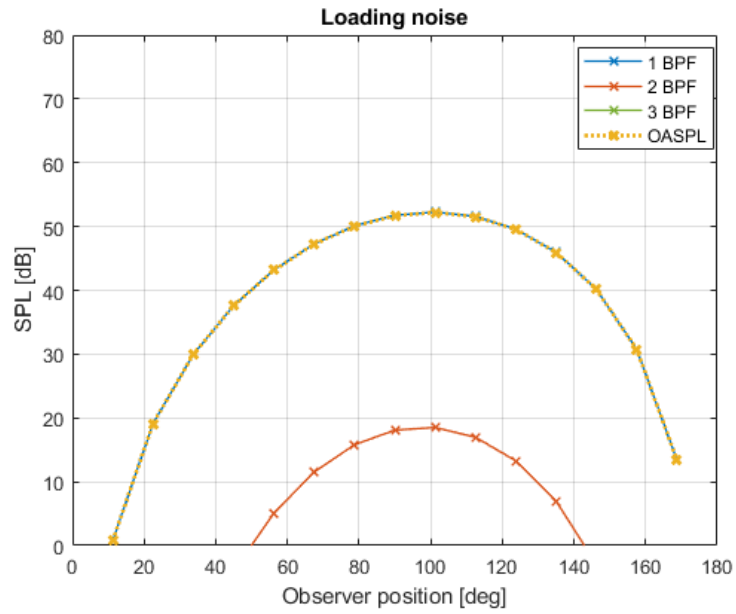
Figure 8.23: Loading noise
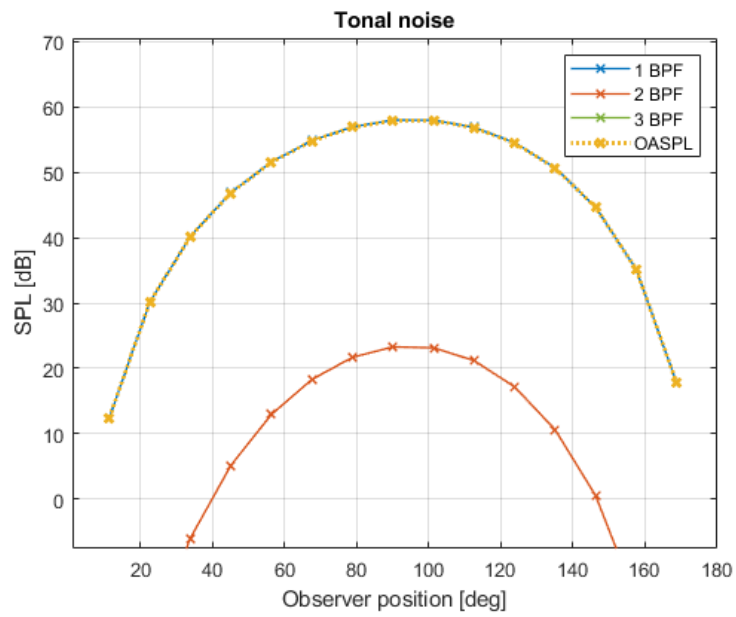
Figure 8.24: Tonal noise
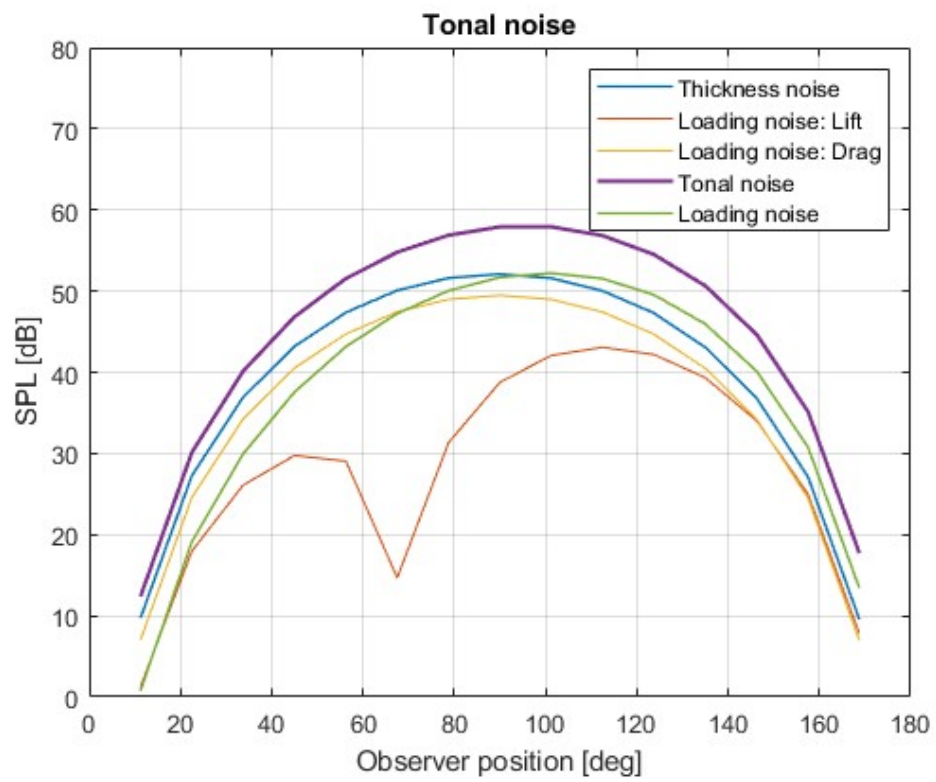
Figure 8.25: OASPL Tonal noise components
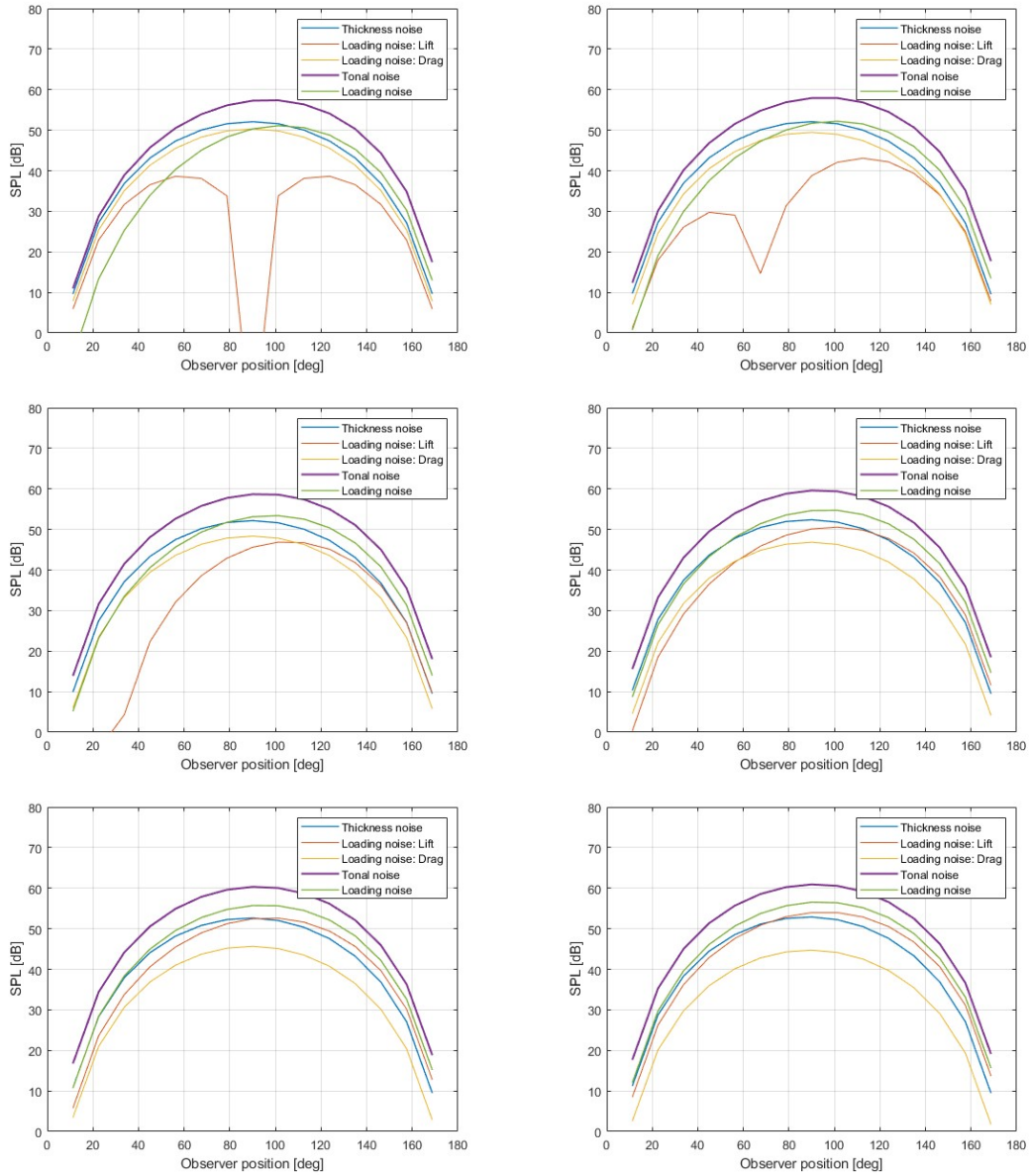
Figure 8.26: Tonal noise components of the Overall Sound Pressure Level at V=0.001 m/s - V=2 m/s - V=5 m/s- V= 10 m/s V=15 m/s V=20 m/s (from left to right)

8.6 Parameterization of Blades

Because the loading coefficients and the noise contributions must be valued in multiple sections of the blades, it is crucial to be able to describe every considered geometry in an efficient way. Direct interpolation, polynomial curve fitting and Bézier curve fitting are examples of general parametric techniques usually adopted to describe the distributions of geometrical variables. In particular, Bézier curves or B-spline are often favored for the capability to work in a large design space, with the disadvantage of requiring a proportionally large number of design variables. The approach followed in this thesis consists in scaling the constructive parameters of the geometry distributions attributed to the baseline propeller. The blade geometry of the baseline propeller is interpolated in Sec. 8.2.

The pitch distributions are obtained by multiplying the twist cubic law of the baseline with the ratio of the desired pitch angle in the inner section of the blade, β_r, to the corresponding value at the reference, β_{r0}.

$$twist\ law\{i\} = @(x)\ \frac{\beta_r(i)}{\beta_{r0}} \cdot p_{\beta 3} \cdot x^3 + \frac{\beta_r(i)}{\beta_{r0}} \cdot p_{\beta 2} \cdot x^2 + \frac{\beta_r(i)}{\beta_{r0}} \cdot p_{\beta 1} \cdot x + \frac{\beta_r(i)}{\beta_{r0}} \cdot p_{\beta 0}$$

where $p_{\beta k}$ are the coefficient of the baseline twist distribution.
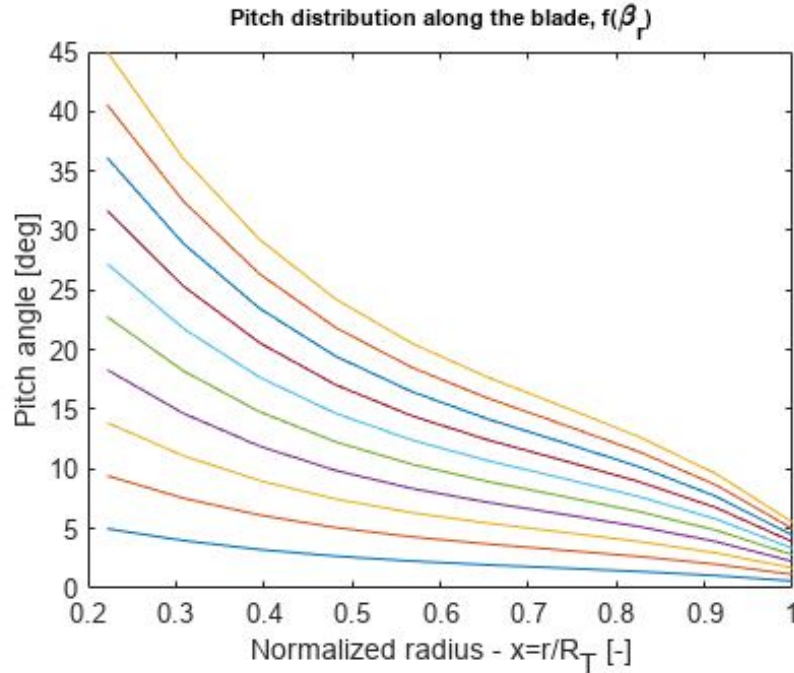
Figure 8.27: Ten twist distributions along the blade, with β_r, selected between 5 deg and 45 deg

The chord-length distributions are derived from the quadratic law of the baseline propeller. In particular, the coefficient of the second-order term, p_{c2}, is scaled with the ratio of the variable chord value at the root station c_r and the baseline value c_{r0}, while the remaining coefficients are identified forcing the passage of the parabola $f(x) = ax^2 + bx + c$ at the inner chord value, c_r, and at the variable chord length of the tip station, c_t.

$$a = \frac{c_r(i)}{c_{r0}} \cdot p_{c2}$$

$$\begin{cases} x = 0.222 : & a(0.222)^2 + b(0.222) + c = c_r(i) \\ x = 1 : & a + b + c = c_t(i) \implies c = c_t(j) - a - b \end{cases}$$

$$a(0.222)^2 + b(0.222) + c_t(j) - a - b = c_r(i)$$

$$a(0.222^2 - 1) + b(0.222 - 1) = c_r(i) - c_t(j)$$

$$(0.222 - 1)(0.222 + 1)a + b(0.222 - 1) = c_r(i) - c_t(j)$$

$$b = \frac{c_r(i) - c_t(j)}{0.222 - 1} - a(0.222 + 1)$$

$$chord\ law\{i, j\} = @(x)\ \frac{c_r(i)}{c_{r0}} \cdot p_{c2} \cdot x^2 + \frac{c_r(i) - c_t(j)}{0.222 - 1} - \frac{c_r(i)}{c_{r0}} \cdot p_{c2}(0.222 + 1) \cdot x$$
$$+\ c_t(j) - \frac{c_r(i)}{c_{r0}} \cdot p_{c2} - \frac{c_r(i) - c_t(j)}{0.222 - 1} - \frac{c_r(i)}{c_{r0}} \cdot p_{c2} \cdot (0.222 + 1)$$

$$(8.1)$$
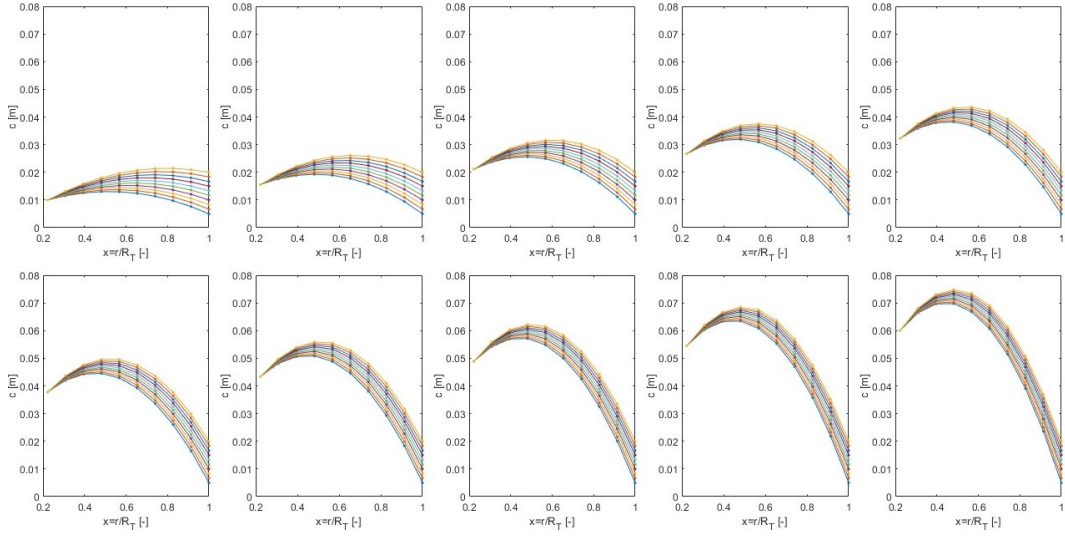
Figure 8.28: Chord distributions along the blade, with $0.01m < c_r < 0.06m$ and $0.005m < c_t < 0.02m$

As for the original design, the thickness of the blade elements is kept constant and it is not modified in the optimization process. All the mid-chord points of the blade sections are aligned with each other, resulting in symmetrical planforms.

8.6.1 Design Space Exploration

Because of the black-box nature of the optimization process, a design space exploration is conducted in advance. The design space is discretized generating 1000 blades defined by the combination of the following design parameters:

- 10 chord lengths of the first section, equally spaced in the range $0.01\,m < c_r < 0.06\,m$

- 10 chord lengths of the last section, equally spaced in the range $0.005\,m < c_t < 0.02\,m$

- 10 local pitch angles of the first section, equally spaced in the range $5\,deg < \beta_r < 45\,deg$

Each blade is divided into 15 elements. Where the number of iterations in the computation of coefficients a and b exceeds the threshold of 500, blades have been discarded by setting $Ct = 0$, $Cp = 0$ and $FM = 0$. This especially happens for negative angles of attack leading to negative thrust, and represents the cause of the singularities in **Figures 8.29, 8.32** into the subplots at $\beta_r = 5$ deg.

The following subfigures, from left to right, will therefore refer to the distributions starting with $\beta_r = 5$ deg, 9.4 deg, 13.8 deg, 18.3 deg, 22.7 deg, 27.2 deg, 31.6 deg, 36.1 deg, 40.5 deg, and 45 deg.

The propulsive efficiency is a key measurement for comparing propellers with different geometry at the same advance ratios.

$$\eta_{climb} = \frac{V_{climb} C_T}{\Omega R_T C_P}$$

Considering that the baseline efficiency is $\eta = 0.2030$, improvements of up to 10% can be observed from $\beta_r = 13.8$ deg to $\beta_r = 36.1$ deg in **Fig.8.29**. Moreover, enhancements of up to 40% are possible for the thinnest blades, for twist angle starting from β_r=22.7 deg. The efficiency trend of the blade is conditioned by the efficiency of the airfoil profile Cl/Cd at the analyzed Reynolds number $Re = 50000$ in **Fig. 8.30**. Therefore, a count along the elements of each blade has been conducted to visualize how many sections are positioned at an angle of attack corresponding to a suitable range of maximum efficiency of the airfoil. 8.31. The contour is not rendered for constant ZData, as the null values for $\beta_r = 5$ deg, 9.4 deg.

The second parameter analyzed is the Figure of Merit.

$$FM = \frac{C_T^{3/2}}{\sqrt{2} C_P}$$

The figure of merit is usually defined as the ratio of the ideal power required to hover to the actual power required. However, it provides a useful description of the capabilities of a propeller even at low speed in vertical climb.

The most significant variation of the figure of merit in **Fig. 8.32** is given by the twist angle, so that it is possible to achieve higher figures of merit compared to the baseline from β_r=31.6 deg. Moreover, wider blades at the root and tip are favored. Some contour lines of FM reflect those of thrust and power at the propeller hub, particularly the higher lines in the subplot $\beta_r = 45 deg$ of **Fig. 8.33, 8.34**.

Regarding the reduction of the maximum sound pressure level for tonal noise (**Fig.8.35**), the minimum values are observed for extremely thin blades at the tip. The variation in chord length at the tip assumes much greater significance compared to the cases seen previously. This occurs especially for relatively low twist angles, beginning from 5 degrees, where the load component is minimal. Indeed, the blade benefits from the reduction in tip area, precisely because the radiative efficiency of each blade section of the propeller depends on the local radial station. Therefore, as propeller tips possess the highest radiation efficiency, an appropriate distribution of loads on the blade is fundamental to minimize propeller noise.
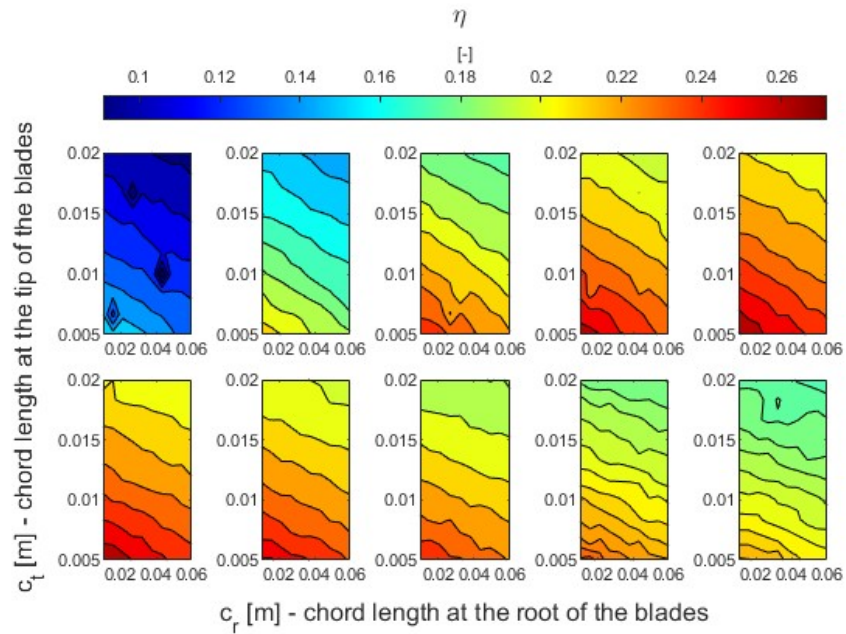
Figure 8.29: Propeller efficiency η at J=0.1 for ten twist distributions $\beta_r = 5deg - 45deg$ varying c_r and c_t
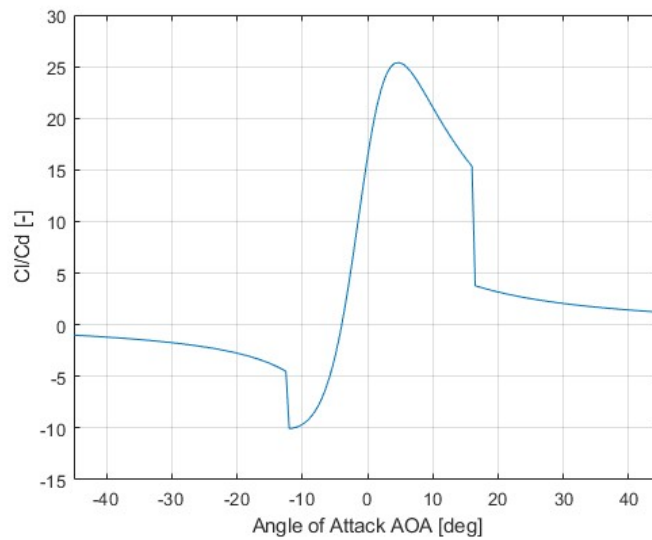
Figure 8.30: Cl/Cd vs AoA at Re=50000 between -45 deg and +45 deg

71
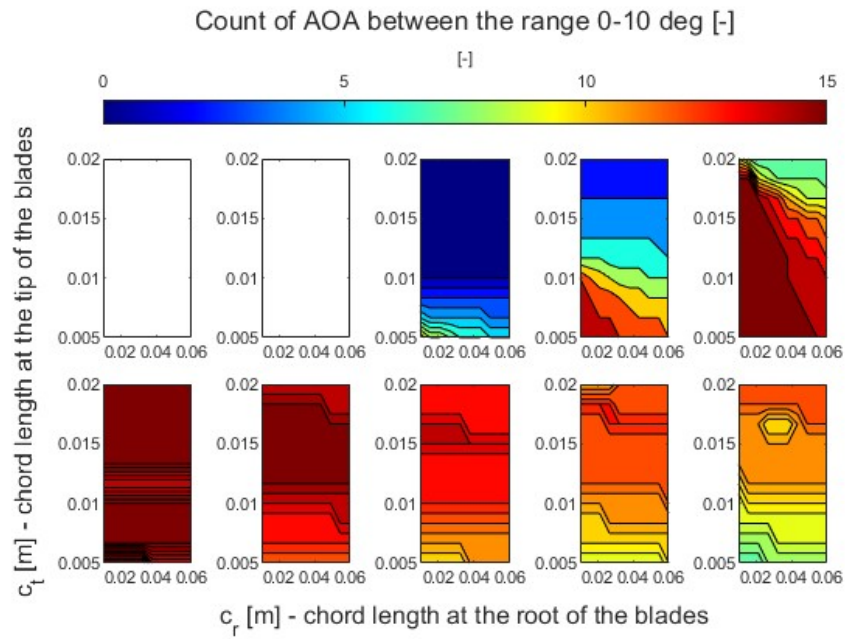
Figure 8.31: Count of AoA between the range of Cl/Cd:20-25 at J=0.1 for ten twist distributions $\beta_r = 5deg - 45deg$ varying c_r and c_t
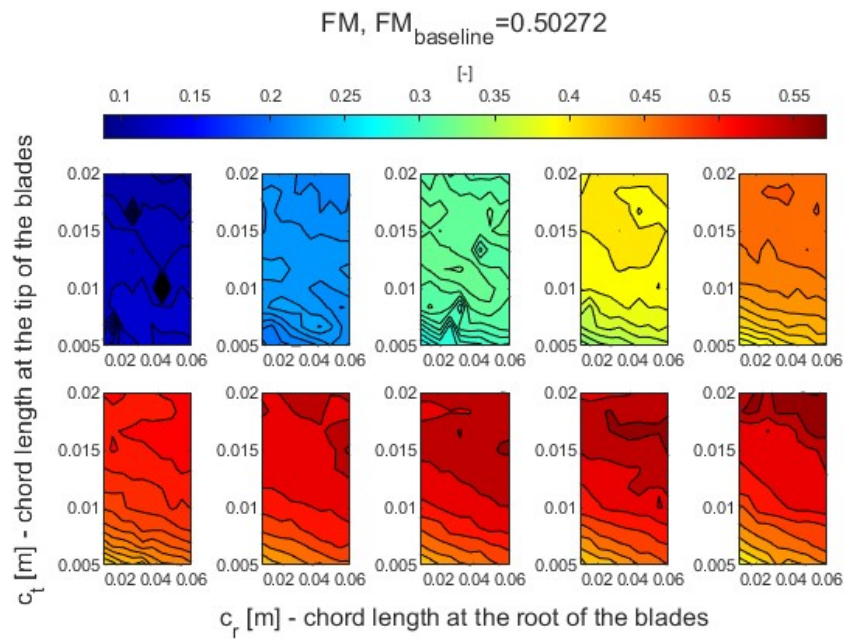
Figure 8.32: Propeller figure of merit FM at J=0.1 for ten twist distributions $\beta_r = 5deg - 45deg$ varying c_r and c_t

Thrust [N], Thrust$_{baseline}$=4.24N
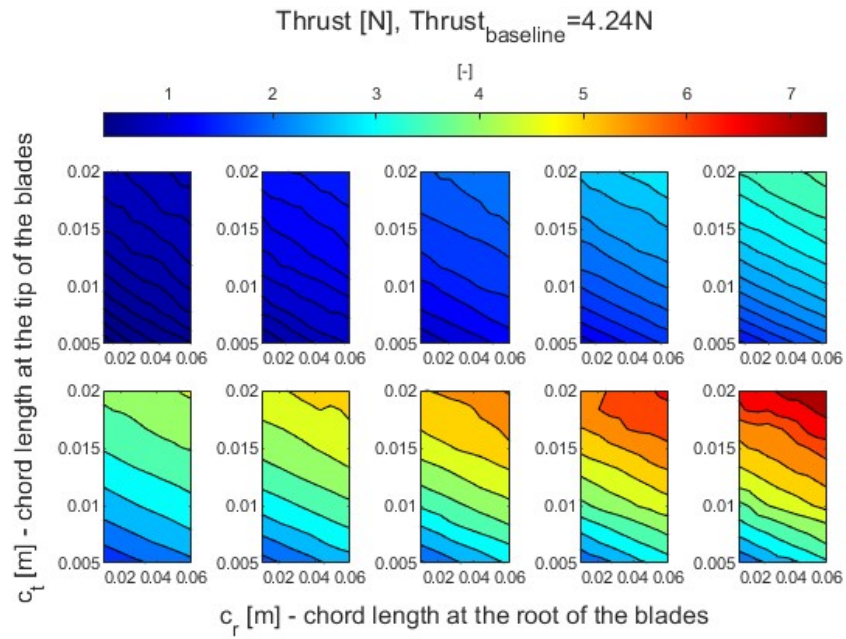
Figure 8.33: Power required by the propeller at J=0.1 for ten twist distributions $\beta_r = 5deg - 45deg$ varying c_r and c_t of the blade

Power [W], Power$_{baseline}$=41.783W
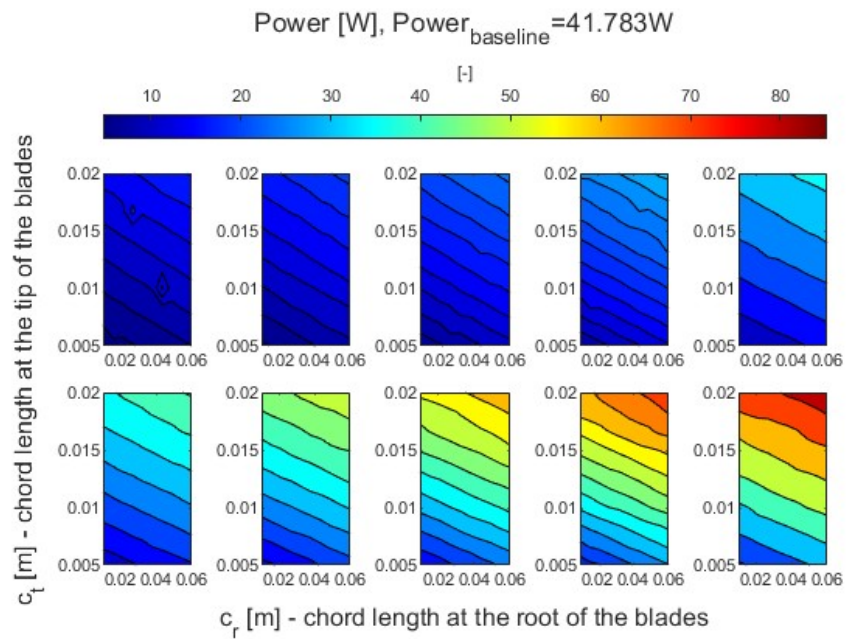
Figure 8.34: Thrust generated by the propeller at J=0.1 for ten twist distributions $\beta_r = 5deg - 45deg$ varying c_r and c_t of the blade
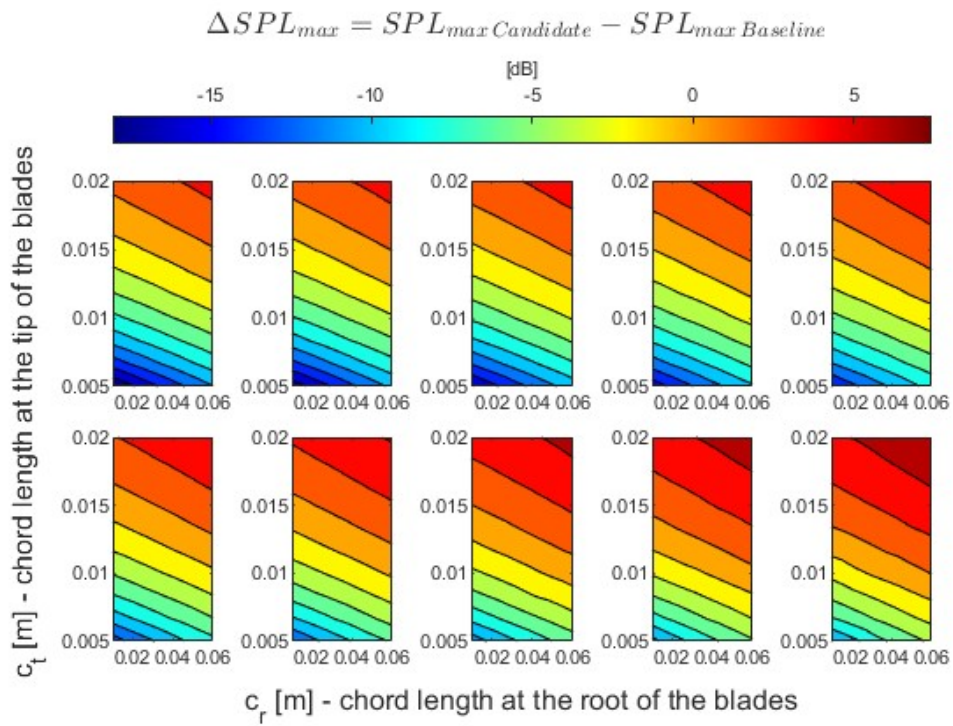
Figure 8.35: Variation of ΔSPL_{max} at J=0.1 for ten twist distributions $\beta_r = 5deg - 45deg$ varying c_r and c_t

Chapter 9

Verification

In this chapter, it will be verified whether the BEMT model and the Helicoidal Surface Theory are implemented correctly on the baseline propeller. For this purpose, a comparison is executed with the BEMT-based model applied in a time-domain FW-H noise computation for the benchmark of Casalino [14]. The validation is performed by correlating the high-fidelity numerical data and the experimental measurements of the same reference for both the acoustic and the aerodynamic prediction.

The verification is conducted in the following working conditions: the propeller operates at 5000 RPM, subjected to axial flow velocities ranging from 0 to 20 m/s and advance ratio from 0 to 0.8.

In the following lines, a general overview of the experimental setup is provided. The propeller was manufactured in aluminum alloys and tested in the low-speed semi-anechoic aeroacoustic wind tunnel of Delft University of Technology (TU-Delft A- Tunnel). The variation in the advance ratio was achieved by changing the jet wind tunnel velocity. A convergent nozzle of contraction ratio 15:1 and exhaust diameter of 0.6 m is used to realize the incoming flow. The propeller is located at about 1.2 nozzle diameter from the nozzle, in the potential core of the jet. The turbulence intensity is 0.14% at 2.5 m/s and decreases below 0.1% from 10 m/s. The propeller performance was measured using a load cell and a torque cell embedded with the motor and the encoder in a nacelle that supports the propeller. The signals were acquired by a National Instruments acquisition board with a sampling frequency of 5 KHz and an acquisition time of 15 s.

The acoustic measurements were performed with a linear array of 13 analog free-field microphones located perpendicular to the propeller plane. The array is mounted at a distance of 1.2 m from the propeller axis (4D). The distance between each microphone is 0.15 m. Microphone n° 1 is 0.9 m (3D) above the propeller plane while microphone n° 7 is located in correspondence on the propeller plane,

as in **Fig.9.11**. Pressure data were collected by a National Instruments acquisition board with a sampling frequency of 51.2 KHz and a recorded time of 30 seconds for each measurement. The acoustic signals are divided into 1197 Hanning-widowed Welch blocks with 50% overlap, so that a signal is assigned to a bandwidth of 20 Hz.

9.1 Aerodynamic verification
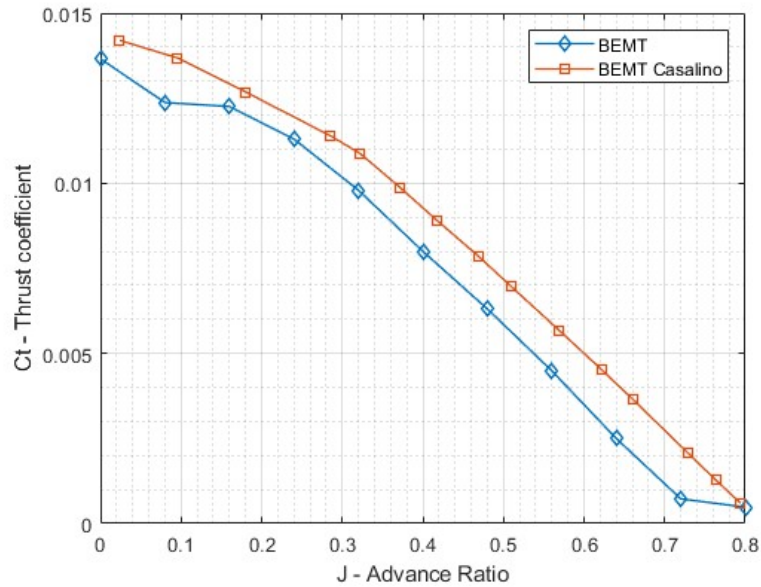
Figure 9.1: Thrust coefficient

From the comparison between the two BEMT models, an offset of about -0.001 emerges in the thrust coefficient curves, while the torque coefficient curve is predicted with good accuracy. The offset is attributable to the fact that in the present thesis, the Reynolds number variation along the radius in the load prediction is not considered, and only the coefficients at $Re = 50,000$ are extrapolated. Conversely, in [14] five Reynolds numbers cover the range of radial variation, whose extension is depicted in **Fig.9.3**.

A note must be made regarding the CL-alpha and CD-alpha curves at $Re = 50,000$ utilized in this thesis. The curves were generated using the tool Opty∂B, which employs the boundary layer Drela and Giles method combined with a second-order panel method. These two techniques are integrated through an iterative process, which takes into account the transpiration velocity within the boundary
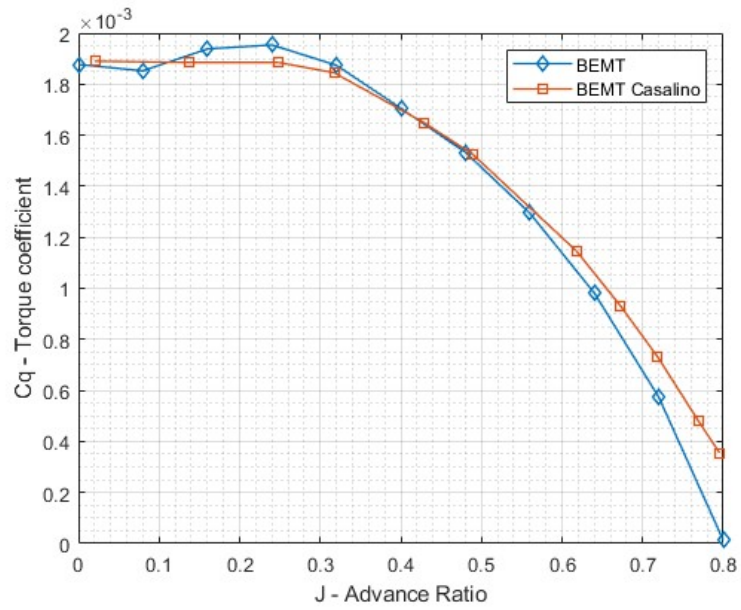
Figure 9.2: Torque coefficient
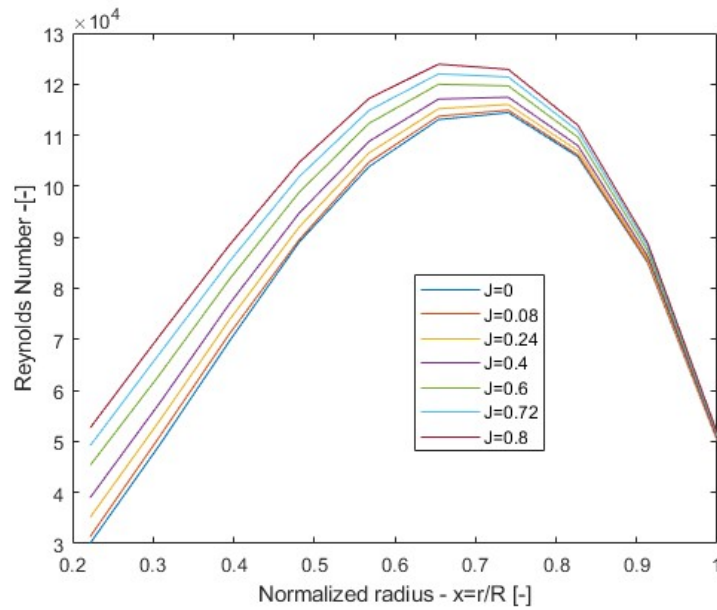
Figure 9.3: Radial variation of Reynolds number for different Advance Ratio

layer. A peculiarity of the algorithm is in handling Lighthill's singularity close to laminar separation. [14] In this case, similar results to Xfoil at Ncrit=5 with a

2-degree offset are achieved. This is attributed to the different characteristics of the boundary layer predicted by Xfoil and Opty∂B. Due to a loss of data regarding the boundary layer characteristics, reference is made to the investigation explored by the authors at $Re = 80{,}000$, where the outputs of Opty∂B overestimate the drag curve at positive angles of attack compared to Xfoil results. The analysis is conducted at $\alpha = 4$ deg and $\alpha = 12$ deg. At a lower angle of attack, it emerged that the extension of the laminar separation bubble is smaller for the Opty∂B case and characterized by a lower growth rate of displacement thickness. At $\alpha = 12$ deg the trends are found to be similar, even if the influence of the laminar separation bubble after reattachment is smaller. A trailing-edge turbulent separation is observed and a faster growth of the momentum thickness was predicted by Opty∂B-Bemt.
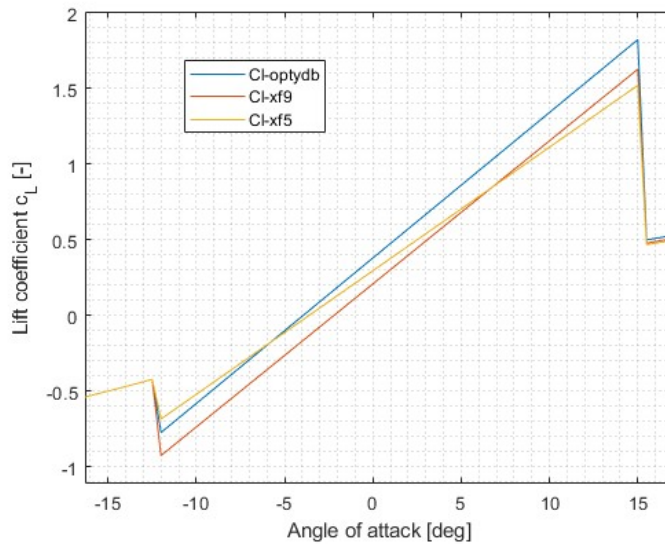
Figure 9.4: Lift coefficient from Optydb vs Xfoil at Re=50,000

Results for thrust and torque coefficient obtained with Opty∂B-Bemt are compared to measurements and LBM/VLES in Ref. [14] (**Fig. 9.6 9.7**) and shown in **Fig. 9.8 9.9**. The thrust and torque coefficient distributions from the low-fidelity approach are predicted adequately throughout the entire advance ratio range compared to the high-fidelity results, even close to hovering conditions and in zero-thrust conditions at J=0.8. Numerical results are in good agreement with measurements.

The low-fidelity and the high-fidelity methods produce reliable output since both effectively account for turbulence. Xfoil data from Drela combines a panel method with an integral formulation of the boundary layer and successfully manages to predict the flow for low Reynolds number thanks to reliable laminar, turbulent and
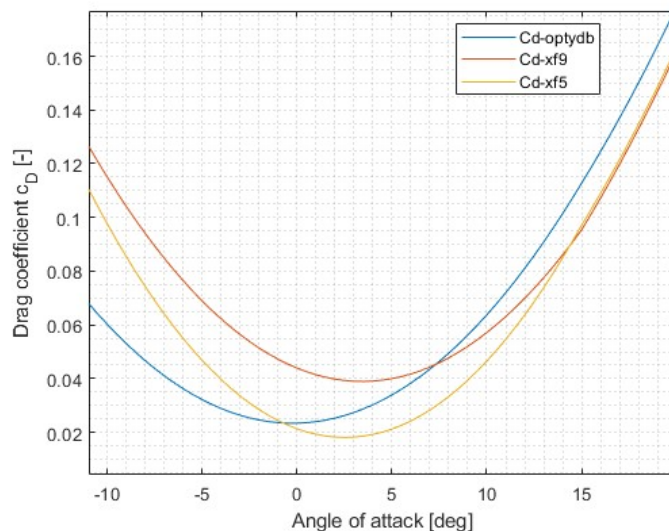
Figure 9.5: Drag coefficient from Optydb vs Xfoil at Re=50,000
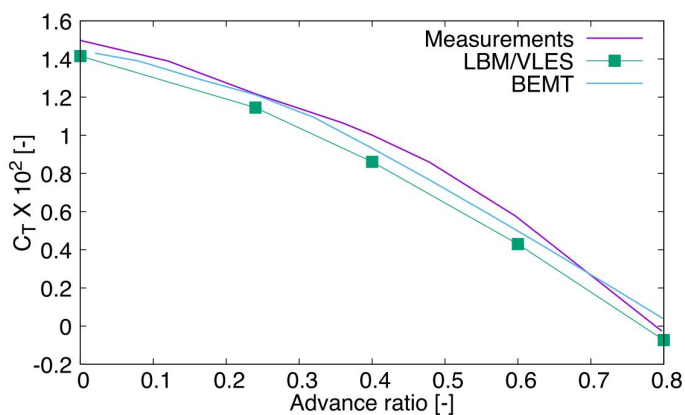
Figure 9.6: Thrust coefficient

transition formulations. The lattice Boltzmann method (LBM) is predicated on the concept of statistically tracking the advection and collision of fluid particles, through distribution functions aligned along predefined directions. Turbulence is introduced by defining the parameters of equilibrium distributions, which are tailored to the turbulent scales of the resolved flow, computed via a two-equation transport model based on $\kappa - \epsilon$ re-normalization group theory. Gas relaxation properties drive the system towards a state of dynamic equilibrium. In contrast to RANS, Reynolds stresses are not explicitly incorporated, as the Boltzmann distribution generates
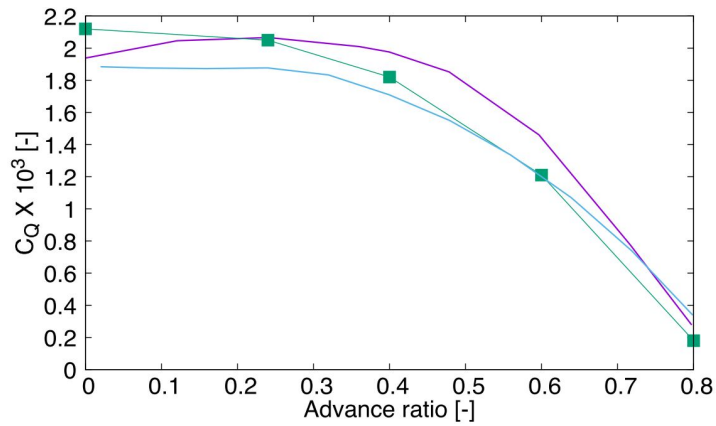
Figure 9.7: Torque coefficient

functions capable of producing all moments of the fluctuations.
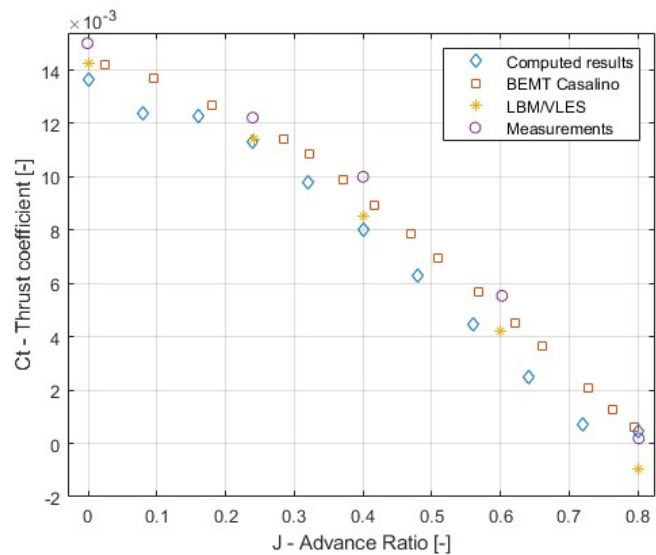
Figure 9.8: Thrust coefficient vs Advance Ratio, verification of data at 5000 RPM

9.2 Aeroacoustic verification

In light of the availability of noise power spectral density at two observer positions (Mic.1 at the left side and Mic. 7 at the right side) in **Fig. 9.10**, the agreement of the obtained sound pressure levels is analyzed at the blade passing frequency
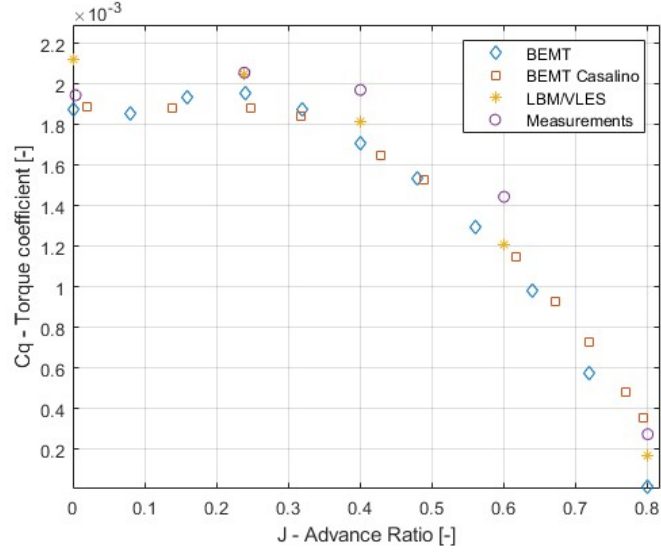
Figure 9.9: Torque coefficient vs Advance Ratio, verification of data at 5000 RPM

and the next two harmonics at $\theta = 90\,deg$ and $\theta = 126.8\,deg$. The first BPF can be observed in the power spectral density as a peak at 166.67 Hz, while the first higher harmonic of the BPF corresponds to 333 Hz and the second to 500 Hz.

In order to compare the predicted noise with the experimental and numerical results in **Fig. 9.10,** the Sound Pressure level at each frequency is computed by adding the logarithm of the bandwidth (20 Hz) at the power spectral density of the signal, stating that

$$SPL(dB) = 10\log_{10}\frac{P(f)\Delta f}{p_{ref}^2}$$

where $P(f)$ is the power spectral density of the signal, Δf is the width of the band.

The tonal noise derived from the frequency-domain helicoidal surface theory is compared to the tonal component obtained by a time-domain FW-H noise computation, based on a compact dipole and monopole formulation described in Ref. [48], where the BEMT-based approach constitutes the aerodynamic input. The acoustic outcomes are verified by comparing the tone peaks with measurements and LBM/VLES prediction for several values of the advance ratio, as in **Fig.9.10**.

81
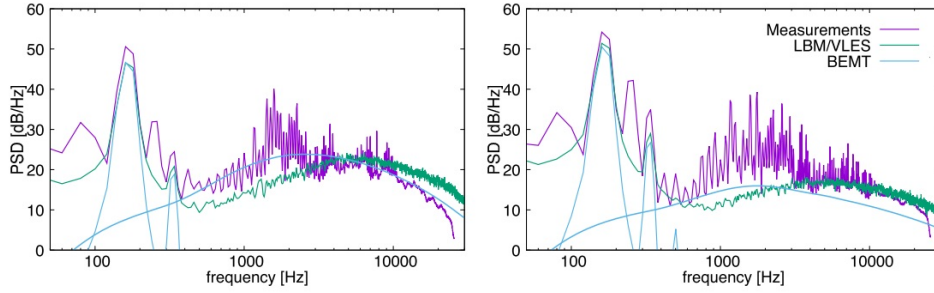
Figure 9.10: Noise power spectral density at J=0.24 at microphone 1 (left) and 7 (right). Comparison between measurements, BEMT tonal results, semi-analytical broadband results based on corrected Schlinker & Amiet's wall pressure model and PowerFLOW/PowerACOUSTICS results

Propeller rotational speed [rpm]	5000
Axial Flow Velocity [m/s]	6
Advance Ratio - J	0.24
Blade Passing Frequency - BPF [Hz]	166.67
Distance of the mic. array from propeller axis [m]	1.2
Distance from propeller plane Mic. 7 [m]	0
Distance from propeller plane Mic. 1 [m]	0.9
Directivity angle from propeller axis Mic.7 [deg]	90
Directivity angle from propeller axis Mic. 1 [deg]	126.8

Table 9.1: Parameters set for the comparison of Fig. 9.13

Previous evidence of analogous verification is found in Ref. [49], where the authors compare the frequency domain acoustic formulation derived by Hanson with the time-domain compact dipole/monopole formulation and high-fidelity simulations conducted with the CFD solver SIMULIA Poweflow.

A first observation from the authors which is corroborated here is that the noise level predicted by the frequency domain approach is found to decay more rapidly at higher harmonics, as the harmonic number m is included in the Bessel function term, which governs the radiation of both thickness and loading components.

A remarkable agreement is found between the time-domain and the frequency-domain methods at BPF1 in [49]. Moreover, in the present thesis, differences emerge at BPF1 in favor of the frequency domain with the increase of the advance ratio, especially at the propeller plane. At J=0.6 (**Fig. 9.16**) about 7 dB of disparity is observed. This is likely because starting from J=0.4 a significant portion of the blade from x=0.5 to x=0.8 finds itself at Reynolds numbers exceeding 10^5, at
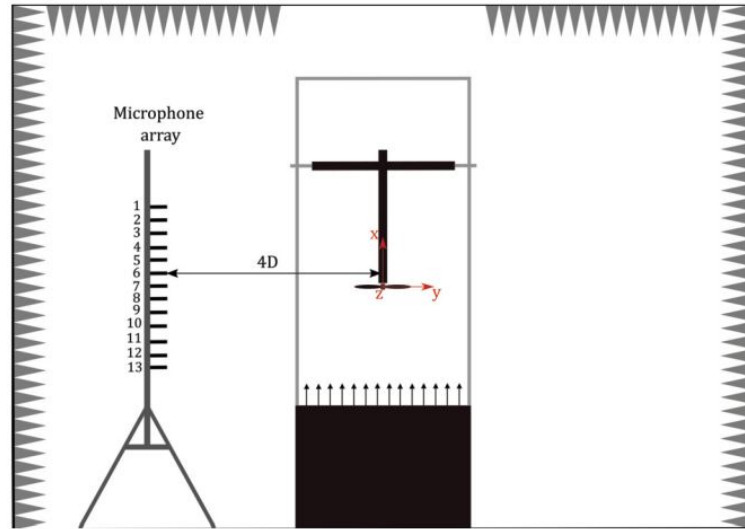
Figure 9.11: Linear microphones array configuration [14]

angles of attack close to 0 deg, where drag is minimum with respect to the case at $5 \cdot 10^4$. Hence, a good prediction of the aerodynamic coefficients is a requirement to obtain faithful noise computation results.
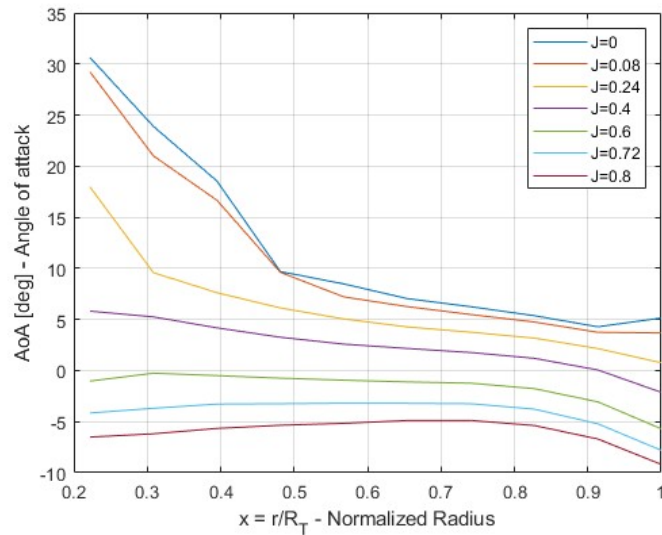
Figure 9.12: Angles of attack of the blade elements at various advance ratio

This difference is consistent with the results of multiple test cases in Ref. [50, 37], where the prediction of the maximum tonal noise at the BPF with Hanson's

frequency method exhibits an average error of 7.2 dB compared to other prediction methods at $M < 0.6$, while the discrepancy with experimental results remains in the range of 5-10 dB. Despite consistent errors, the frequency formulation developed by Hanson is considered suitable for preliminary design and optimization studies, so even the implementation put into effect in the present thesis results to be appropriate.
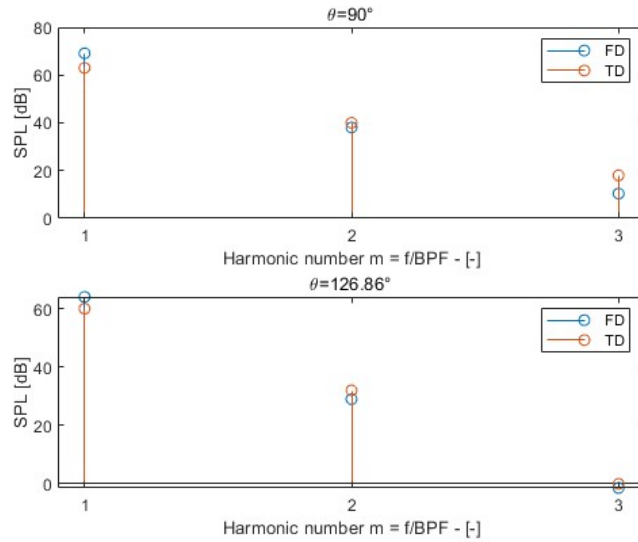
Figure 9.13: SPL at the first three harmonics, comparison between the frequency domain and the time domain results at J=0.2 (V_∞=6 m/s)

With regards to the comparison with experimental results, in Ref. [14], uncertainty is expressed regarding measurement at BPF1, because it is located below the cut-off frequency of 200 Hz introduced to account for the background wind-tunnel noise.
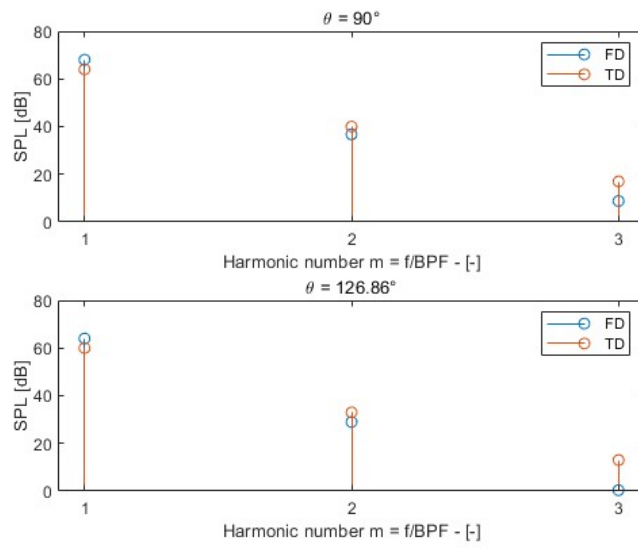
Figure 9.14: SPL at the first three harmonics, comparison between the frequency domain and the time domain results at J=0 ($V_\infty = 0$ m/s)
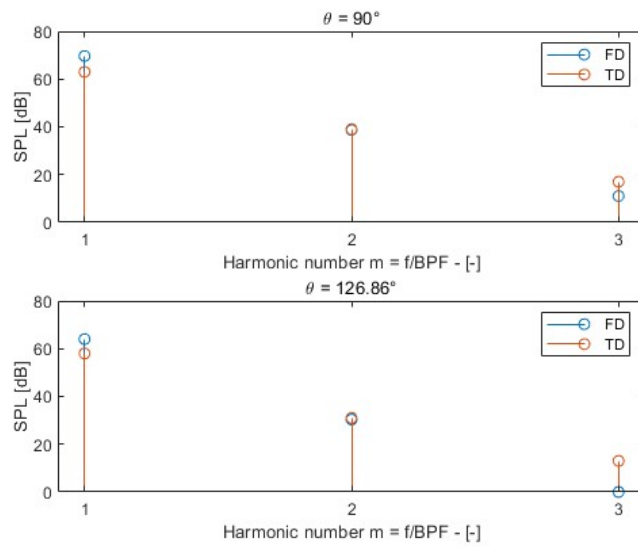
Figure 9.15: SPL at the first three harmonics, comparison between the frequency domain and the time domain results at J=0.4 ($V_\infty = 10$ m/s)
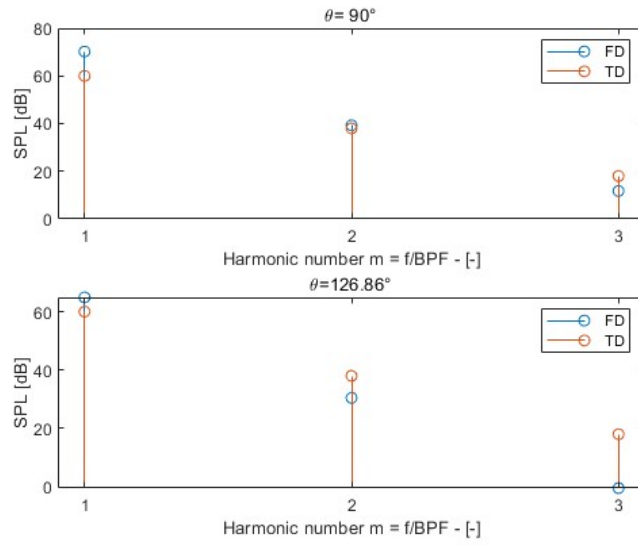
Figure 9.16: SPL at the first three harmonics, comparison between the frequency domain and the time domain results at J=0.6 ($V_\infty = 15$ m/s)
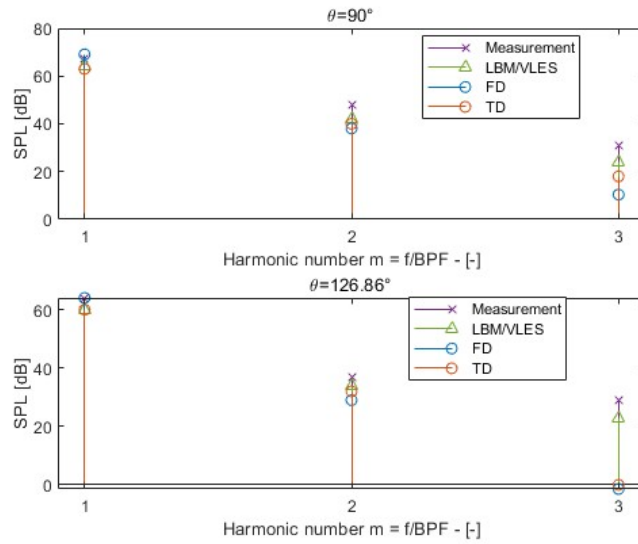
Figure 9.17: SPL at the first three harmonics, validation with high-fidelity and measurement at J=0.24 ($V_\infty = 6$ m/s)
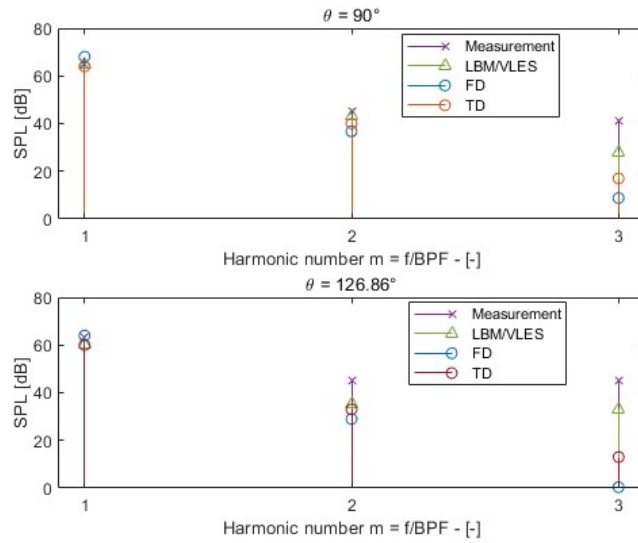
Figure 9.18: SPL at the first three harmonics, validation with high-fidelity and measurement at J=0 ($V_\infty = 0$ m/s)
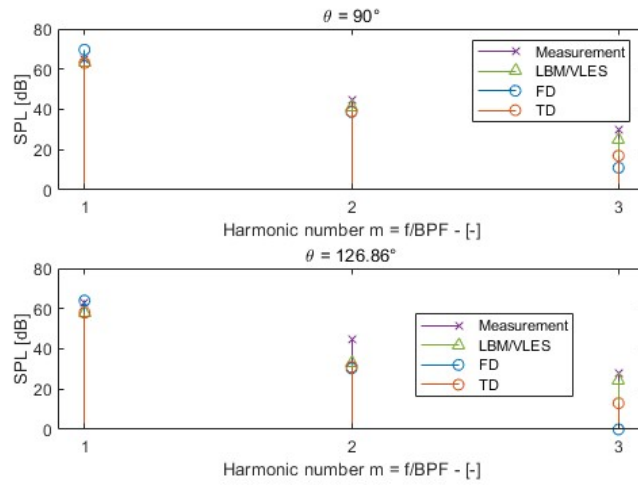
Figure 9.19: SPL at the first three harmonics, validation with high-fidelity and measurement at J=0.4($V_\infty = 10$ m/s)
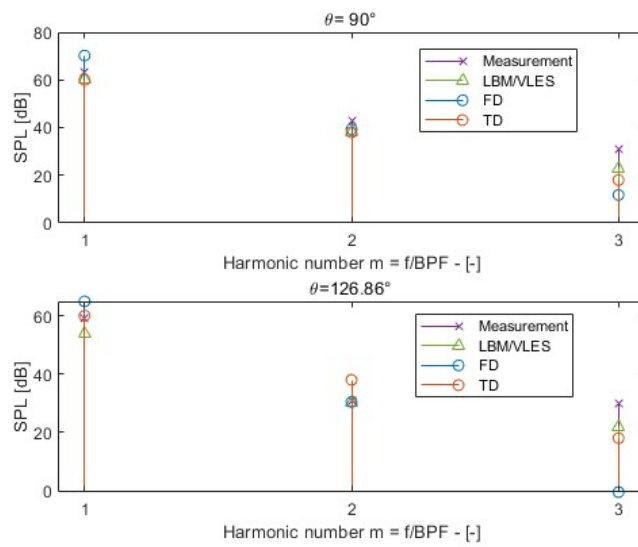
Figure 9.20: SPL at the first three harmonics, validation with high-fidelity and measurement at J=0.6 ($V_\infty = 15$ m/s)

Chapter 10

Optimization Framework

The aim of this thesis is to find an optimum blade design characterized by the maximum Figure of Merit obtainable at the minimum Sound Pressure Level generated by the propeller. The statement falls between the field of multi-objective optimization. Generally, optimization techniques are used to find a set of design parameters $x = x_1, x_2, ...x_N$ that minimize or maximize the value of an objective function. The objective function $f(x)$ might be subject to constraints in the form of equality constraints, inequality constraints, or parameter bounds. Therefore, the suitable variables are contained in a feasible search region where all the constraints are satisfied. Mathematically, the optimization problem is stated as:

$$minimize \quad f(x)$$

$$by\ varying \quad x = x_1, x_2, ...x_N$$

$$subject\ to \quad G_i(x) = 0 \quad i = 1, ..., m_e$$

$$G_i(x) \leq 0 \quad i = m_e + 1, ..., m$$

$$x_l \leq x \leq x_u$$

where the vector function $G(x)$ returns a vector of length m containing the values of the equality and inequality constraints evaluated at x. [51]

When the optimization statement consists of the maximization of the objective function, for some optimization solvers the problem must be rewritten as

$$max(f(x)) = min(-f(x))$$

10.1   Optimization algorithms

Optimization algorithms can be classified into two categories depending on their approach: deterministic or metaheuristic. Deterministic algorithms require the

knowledge of the analytical properties of the problem, like the derivatives of the objective function, to generate a sequence of points that converge to an optimal solution. The two main disadvantages of this type of optimization are:

- the convergence speed is very slow compared to metaheuristic methods

- the gradient-based methods tend to converge into local optima.

Within metaheuristic methods, some initial points (i.e., initial population) are randomly generated. Each point has a search direction, which is determined by the information acquired from previous results. The optimization process is continued by updating the search directions until the convergence criterion is met. Metaheuristics algorithms are often based on swarm intelligence or biology principles and provide great robustness (capability to detect near-optimal solutions) to find the global optima. On the other hand,

- the computation time of optimization is excessive because of exploring most of the area under consideration randomly

- some of the results may not be appropriate and should be discarded.

Furthermore, there is a third type of algorithm that uses a mixture of deterministic and stochastic approaches, using the deterministic method for refining the solution obtained by the heuristic one. [52]

10.2   Genetic algorithms

Genetic algorithms are metaheuristic search methods based on the mechanism of natural selection and natural genetics. The main steps of the algorithm are selection of parents, recombination and mutation, as summarized in the flowchart in **Fig. 10.1**.

First, a random initial population is created. The population is composed by several candidate solutions, designated as individuals or chromosomes. Each chromosome consists of vector entries and is scored by computing its fitness value, which coincides with the optimization criteria. The individuals showing better fitness values are chosen as parents. The higher ranking individuals are selected as *elite* and passed on to the next generation. Other children for the next generations are produced from the remaining parents, either by *mutation* or *crossover*. Mutation implies making random changes to a single parent, while for crossover the vector entries of a pair of parents are combined. Both processes are essential to the algorithm: crossover enables the algorithm to extract the best genes from different individuals and recombine them into potentially superior children; mutation adds to
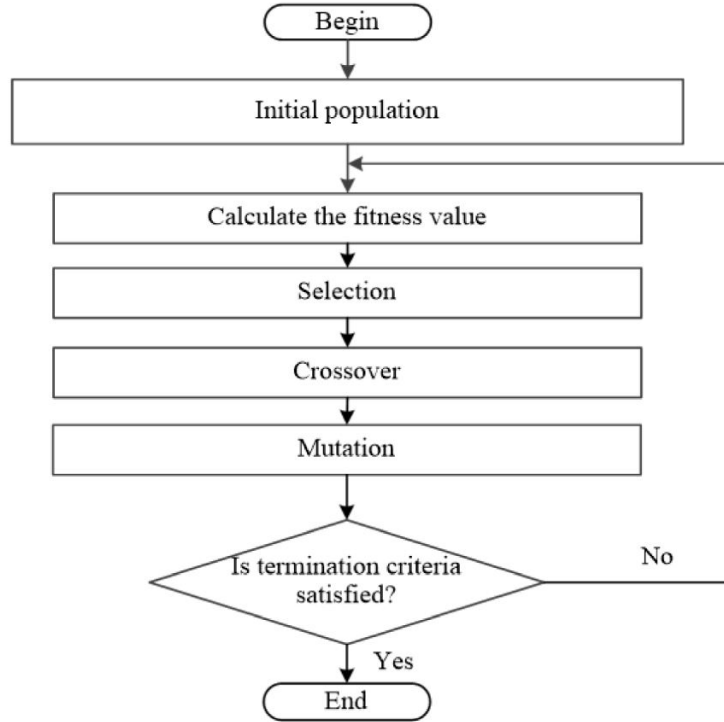
Figure 10.1: Flowchart of the standard genetic algorithm [53].

the diversity of a population and thereby increases the likelihood that the algorithm will generate individuals with better fitness values. The new generation replaces the current population, which will be utilized in the next iteration. The iterations will stop if there is convergence of results, or the number of iterations exceeds the maximum threshold. A drawback of the genetic algorithm as described is that the same individual can appear more than once in the population, requiring a further evaluation.

The employed algorithm in this study is *gamultiobj* embedded in MATLAB Global Optimization Toolbox. The solver adopts a variant of the elitist genetic algorithm NSGA-II, a procedure characterized by an explicit mechanism to preserve diversity [54] [55]. With each generation, the operators of the optimization algorithm drive the population toward the Pareto front, thus selecting 35% Pareto points.

10.3   Pareto front

A multi-objective optimization problem involves finding a set of optimal solutions for different and often competing (or conflicting) objectives. The Pareto curve

91

is defined as the set of all solutions that strictly dominate the feasible choices of the optimization algorithm. Pareto optimality requires that no alternative state exists where improvements can be made to at least one objective function without reducing any other objective. Not all designs plotted in the Pareto frontier chart provide a good trade-off between the two objective functions, thus the developer should compare all feasible designs to determine the most profitable.
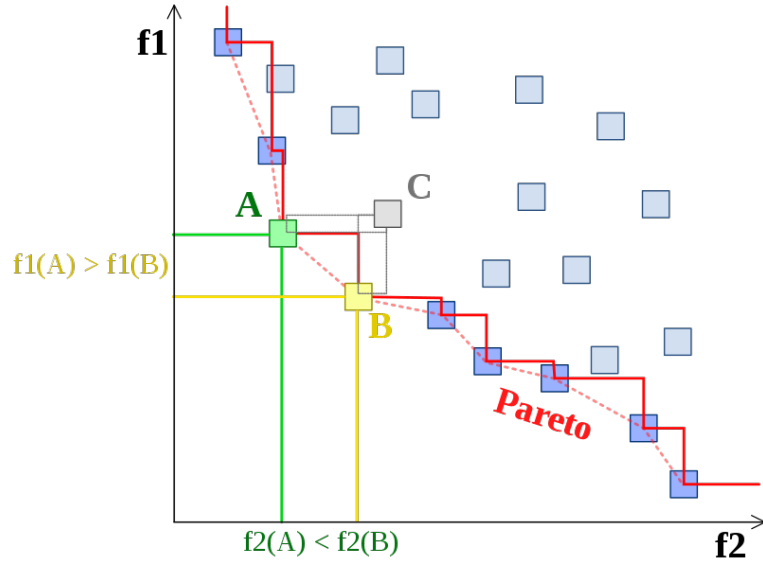
Figure 10.2: Example of a Pareto frontier

10.4 Framework description of the multi-objective optimization

For the aerodynamic optimization, it has been considered to take into account the Figure of Merit of the propeller as the first objective function.

$$FM = \frac{C_T^{3/2}}{\sqrt{2}C_P}$$

The figure of merit is defined as the ratio of the ideal power required to hover to the actual power required. The formula takes into account the ideal power coefficient $C_P = \frac{C_T^{3/2}}{\sqrt{2}}$, derived from the simple momentum theory, and the trend determined from empirical data where $C_P \approx C_T^{3/2}$ [56] . The Figure of Merit is regularly adopted to quantify the performance of propellers in hovering flight, that is at zero velocity of advance, considering that the propeller efficiency would result

in zero because of its definition. The comparison between the figures of merit of different rotors must be conducted at the same blade loading, C_T/σ. The use of the figure of merit in vertical climb analysis of the propeller at low airspeed conditions is documented when true hover is not possible in testing facilities [57] representing near static conditions.

From the design of the experiment in section 8.6.1, it appears that to increase efficiency, versions of the baseline with narrower blades are preferred, while to increase FM, a wider blade span is targeted. Therefore, it is interesting to discover the influence of optimizing FM on η and vice versa, by conducting a secondary optimization for η and comparing the results.

Since the target of the aeroacoustic optimization is to minimize the tonal noise emitted by the propeller, the average value of the Sound Pressure Level over the monitored points is identified as the second objective function,

$$SPL_{avg} = \frac{\sum_{i=1}^{N} SPL_i}{N}$$

where N is the number of radiation angles taken into account. Is it worth mentioning that a similar objective function is found in [10].

10.4.1   Design constraints

Design variable	Lower bound	Upper bound
Chord length of the first section [m]	0.01	0.06
Chord length of the last section [m]	0.005	0.02
Local pitch angle of the first section [deg]	5	45

Table 10.1: Design constraints of the multi-objective optimization

With regard to the strength of the propeller, the minimum possible chord length is placed at the blade tip and equals the 3% of the propeller radius. This value is lower than the recommended threshold cited in Ref. [11], corresponding to the 5% of the propeller radius. However, implementing the selected constraint in the optimizations does not interfere with the primary objective of the current study, which focuses on investigating the physical effects of the geometry of the propeller on the aerodynamic performance and the noise levels generated.

Furthermore, a minimum thrust constraint is imposed at 85% of the thrust computed for the baseline propeller. This allows for accounting for variations in the blade area. By doing so, a more efficient propeller is found in terms of how effectively the rotor converts power into useful work.

It is crucial to emphasize that the restriction of the domain will not negatively impact the efficiency of the procedure. The code will only generate an optimized blade when a physically viable solution exists. When the optimizer finds a possible solution that does not respect the constraints, the blade will be discarded.

Nonlinear constraints are applied to the objective functions in the Optimization Toolbox, in addition to the limitation on thrust, by requiring that the Figure of Merit of the optimized propeller should be greater than the Figure of Merit of the baseline and the average and the maximum Sound Pressure level at the observer points should be less than the emissions of the original propeller.

In the context of the present considerations, the problem statement results in:

$$minimize \quad F(x) = [F_1(x), F_2(x)]$$

$$F_1(x) = -FM \qquad F_2(x) = SPL_{avg}$$

$$by \ varying \quad x = [c_r, c_t, \beta_r]$$

$$subject \ to \quad F_1(x) \leq -FM_{baseline}$$

$$F_2(x) \leq SPL_{avg \ baseline}$$

$$SPL_{max}(x) \leq SPL_{max \ baseline}$$

$$T(x) \geq 0.85 \ T_{baseline}$$

$$x_l \leq x \leq x_u$$

$$x_l = [0.01, \ 0.005, \ 5]$$

$$x_u = [0.06, \ 0.02, \ 45]$$

SPL_{max} is the maximum sound pressure level related to the tonal noise emitted by the propeller, which occurs in correspondence with the propeller plane or at an axial directivity angle in its proximity.

A configuration of 300 generations and a population size of 50 individuals per generation has been specified in the Optimization Toolbox, in order to achieve a good compromise between computational time and genetic variability. A constraint tolerance of 10^{-5} is set for the average change in the spread of Pareto solutions, as recommended for the 'gamultiobj' algorithm.

10.5 Analysis of the multi-objective optimization results

The solver stopped after 108 generations because the average change in the spread of Pareto solution was less than the fixed tolerance.
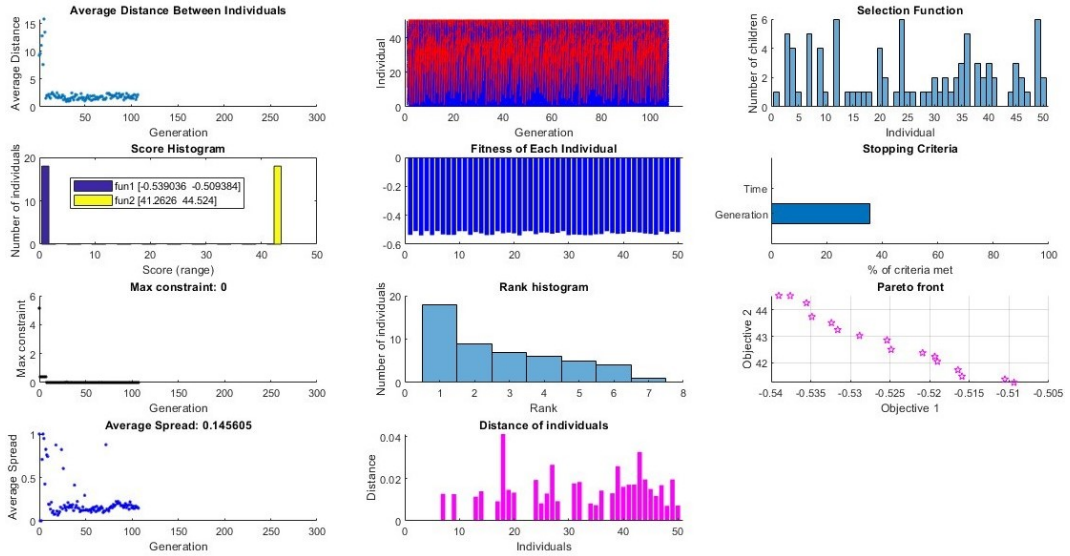
Figure 10.3: Example of genetic algorithm plots for the first optimization in Appendix A

Table 10.2 reports the 18 combinations of chord distributions and pitch angles selected by the optimizer, marked by c_r, c_t and β_r, along with the values of the corresponding objective functions (FM and SPL_{avg}). A disadvantage of the genetic algorithm is that some individuals are analyzed multiple times, so that it occurs that duplicate values also appear in the Pareto front (Opt1 and Opt15).

Three optimized designs are analyzed. 'Opt1' exhibits the maximum Figure of Merit, 'Opt5' refers to the configuration that emits the minimum average sound pressure level over the monitored area, whereas 'Opt14' represents a fair trade-off between the two objectives. The points on the Pareto front and the baseline location are marked in **Fig.10.4.** Comparisons of the optimized configurations in pitch angle and chord distribution with the baseline propeller are shown in **Fig. 10.5 10.6 10.7.**

Table 10.2: Geometric variables and objective values at the Pareto Front

#	c_r [m]	c_t [m]	β_r	FM [-]\	SPL_{avg} [dB]
Bsln	0.0289	0.0094	41.8359	0.5027	44.69
Opt1	0.027098	0.014728	36.009	0.53636	44.505
Opt2	0.027122	0.013865	36.02	0.53485	44.309
Opt3	0.025257	0.013921	36.641	0.53447	43.827
Opt4	0.022138	0.013624	35.959	0.52512	42.627
Opt5	0.021307	0.012658	35.846	0.51448	42.061
Opt6	0.022564	0.015084	36.411	0.53133	43.184
Opt7	0.025462	0.014184	36.703	0.5348	43.958
Opt8	0.022357	0.013936	36.065	0.52688	42.761
Opt9	0.024303	0.014037	36.414	0.53227	43.484
Opt10	0.021358	0.013051	35.966	0.51838	42.223
Opt11	0.021819	0.015278	36.32	0.5273	42.931
Opt12	0.021448	0.014016	35.859	0.52455	42.432
Opt13	0.024294	0.014702	36.433	0.53336	43.648
Opt14	0.021587	0.015714	36.362	0.53006	42.996
Opt15	0.027098	0.014728	36.009	0.53636	44.505
Opt16	0.027108	0.014577	36.015	0.53541	44.472
Opt17	0.021355	0.012854	35.889	0.51786	42.138
Opt18	0.021307	0.012658	35.846	0.51448	42.061
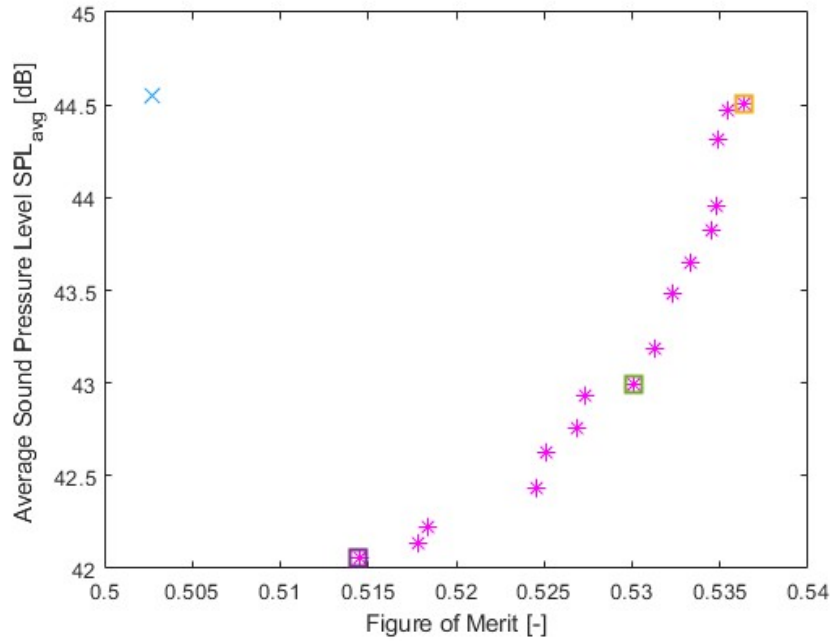
Figure 10.4: Points along the Pareto front (X baseline, □ Opt1, □ Opt5, □ Opt14)

	$c_r[m]$	$c_t[m]$	$\beta_r[deg]$	$A_b[m^2]$	σ [-]
Bsln	0.0289	0.0094	41.8359	0.0068	0.0966
OPT1	0.0271	0.0147	36.0091	0.0071	0.1003
%	-6.22	56.38	-13.93	4.41	3.830
OPT5	0.0213	0.0127	35.8463	0.0057	0.0807
%	-26.29	35.10	-14.32	-16.18	-16.45
OPT14	0.0216	0.0157	36.362	0.0061	0.0865
%	-25.26	67.02	-13.08	-10.29	-10.45

Figure 10.5: Comparison of chord and pitch angle distribution between optimized design 'Opt1' (Continuous lines) and the baseline blade (Dashed lines)

All configurations opt for lower values of the pitch angle at the root, selecting an angle β_r of approximately 36 degrees. The resulting angle of attack distributions are visible in **Fig.10.8**, where it is evident that already at x = 0.3, the optimized blades are effectively lifting surfaces outside of the stall.

Changes in the planform of the blade are represented in **Fig. 10.9.** All three cases choose for a reduction in chord length at the root station (-26% in the case of min SPL, -6% in the case of max FM), while surprisingly the tip is made wider (particularly by $+56\%$ for the max FM case, and $+35\%$ for min SPL), despite being the part that radiates most noise.
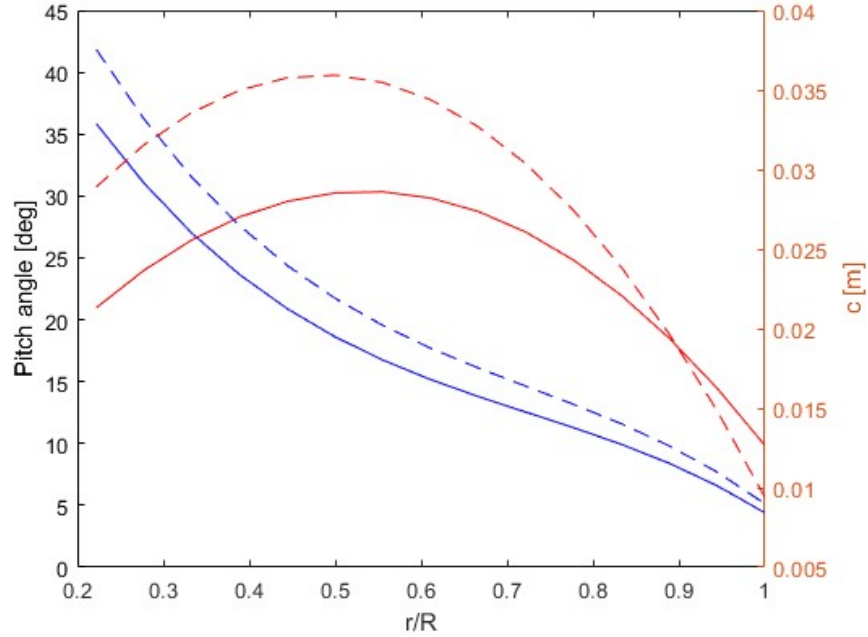
Figure 10.6: Comparison of chord and pitch angle distribution between optimized design 'Opt5' (Continuous lines) and the baseline blade (Dashed lines)

Radial loading distributions in terms of elemental thrust and torque are shown in **Fig. 10.10,10.11**, while the distribution of thrust and torque coefficients are depicted in **Fig. 10.12, 10.13**. The Ct and Cq coefficients shown here are multiplied by the Prandtl tip correction function. It is interesting to note that the blade exhibiting the highest FM is not the one with the highest Ct distribution. The distributions of dT and dQ are similar to the distribution of chord-based Reynolds numbers in Fig. **9.3**, depending also on the chord length and blade velocity. Therefore, the increased thrust for Opt1 is attributed to the increase in chord compared to the baseline, starting from the mid-blade to the tip.

Consequently, this is reflected in a greater increase in aerodynamic noise due to the volume of the blade for Opt1 compared to the baseline (+0.66 dB at the maximum value), shown in **Fig. 10.14.** On the contrary, the area of the blade decreases of the 16% for Opt 5, so that the corresponding maximum thickness noise value decreases of -2.7 dB. This is the design of the minimum noise emitted, with -2.08 dB for the maximum loading noise detected (-1.37 dB for the lift component and -2.44 dB reached in the drag component).

Comparing the results for BPF1 (**Fig. 10.19**) and BPF2 (**Fig. 10.20**), it is observed that attenuation levels of up to -3.5 dB are achieved for BPF1, while for
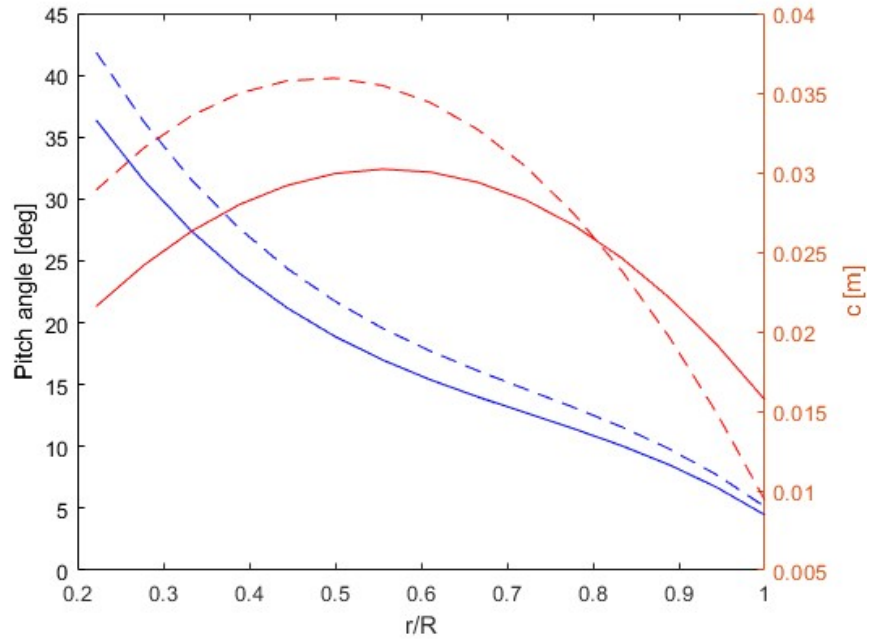
Figure 10.7: Comparison of chord and pitch angle distribution between optimized design 'Opt14' (Continuous lines) and the baseline blade (Dashed lines)

BPF2, they reach about -2.5 dB. Additionally, a slight increase in the sound of the second harmonic is observed for Opt1; however, given its very low levels, it does not raise concern.
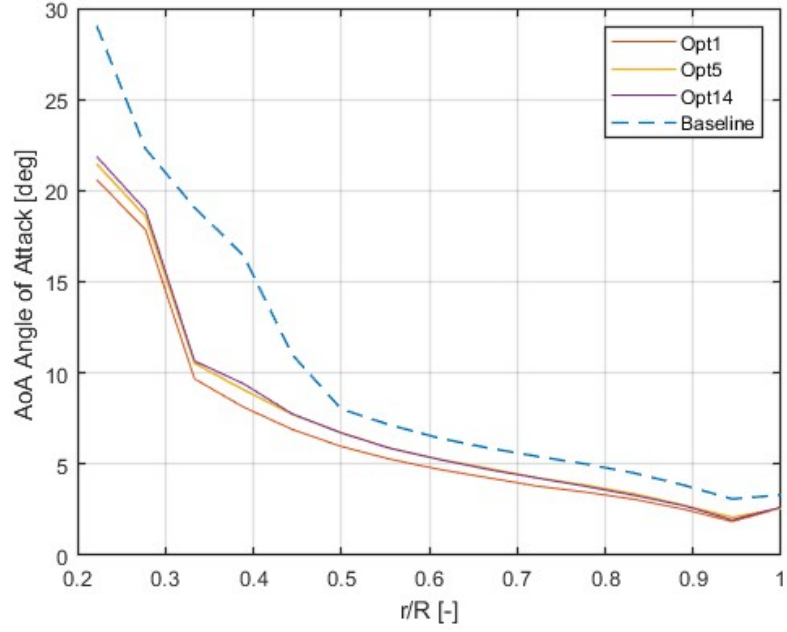
Figure 10.8: Distribution of Angles of Attack over the blade

	SPL_{avg} [dB]	SPL_{max} [dB]	$\max(SPL_V)$[dB]	$\max(SPL_{loading})$ [dB]	$\max(SPL_L)$ [dB]
Bsln	44.69	58.22	52.1	52.21	43.08
OPT1	44.5	57.86	52.76	51.38	42.67
Δ	-0.19	-0.36	0.66	-0.83	-0.41
OPT5	42.06	55.54	49.4	50.13	41.71
Δ	-2.63	-2.68	-2.7	-2.08	-1.37
OPT14	42.99	56.45	50.54	50.65	42.15
Δ	-1.7	-1.77	-1.56	-1.56	-0.93

	$\max(SPL_D)$ [dB]
Bsln	49.48
OPT1	48.45
Δ	-1.03
OPT5	47.04
Δ	-2.44
OPT14	47.62
Δ	-1.86
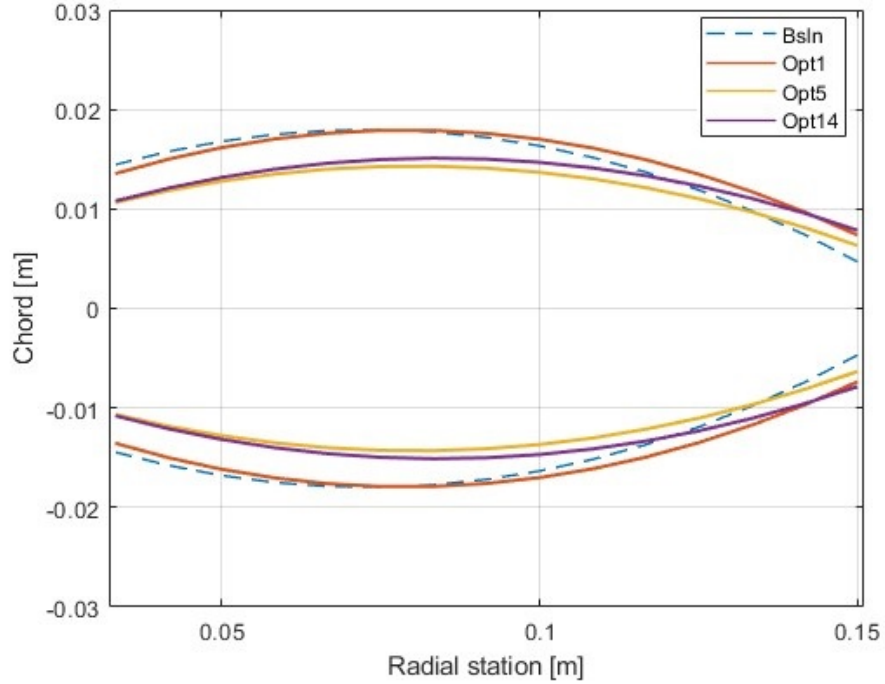
Figure 10.9: Comparison of blade planforms

	η [-]	FM [-]	Ct/σ
Bsln	0.2030	0.5027	0.1287
OPT1	0.2188	0.5364	0.1214
%	7.78	6.70	-5.67
OPT5	0.2252	0.5145	0.1311
%	10.93	2.35	1.86
OPT14	0.2249	0.5301	0.1302
%	10.78	5.45	1.16

10.5.1 Analysis of the Influence of Figure of Merit Optimization on Efficiency and Vice Versa

A second optimization was carried out by setting the propulsive efficiency η_{climb} as the aerodynamic objective function, with the results presented in Appendix A. Regarding the relationship between optimizing η and optimizing the figure of merit, it can be observed from the selected cases that optimizing the figure of merit (+6.70% for Opt1, +2.35% for Opt5, +5.45% for Opt14) consistently leads to an improvement in efficiency (+7.78% for Opt1, +10.93% for Opt5, +10.78% for
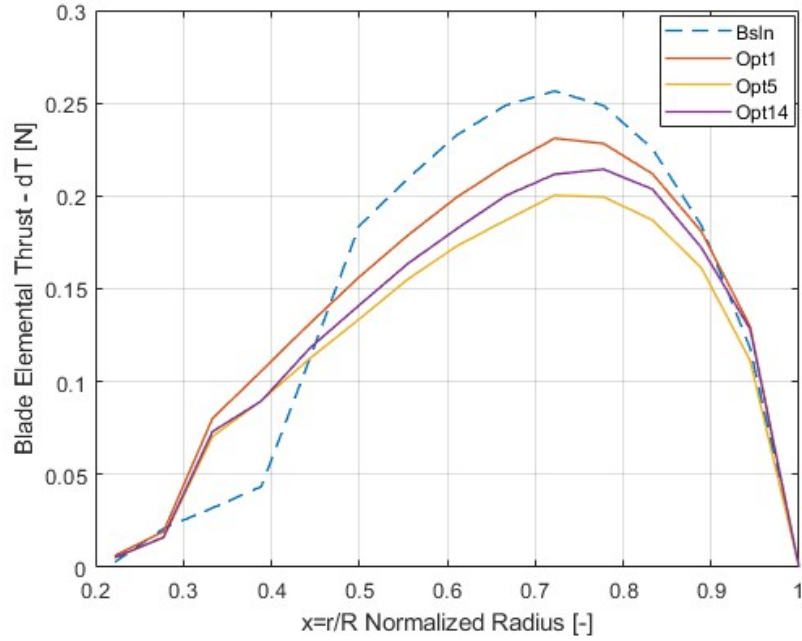
Figure 10.10: Elemental Thrust distribution per blade

Opt14). Conversely, optimizing η (+13.15% for Opt10, +10% for Opt7, +12% for Opt8) does not yield a similar improvement in the figure of merit (+4.83%, +1.95%, -0.06%). This could have been anticipated from the design of the experiment, which revealed that the characteristics for a blade with better propulsive efficiency were similar to those sought for sound optimization. Therefore, seeking a blade among those generatable with the described parameterization with fewer sound emissions also increases propulsive efficiency.
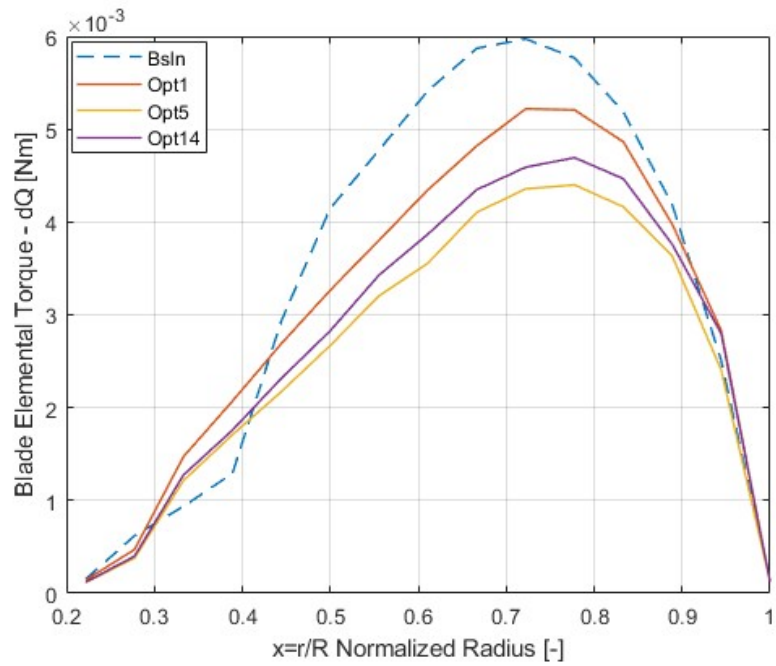
Figure 10.11: Elemental Torque distribution per blade
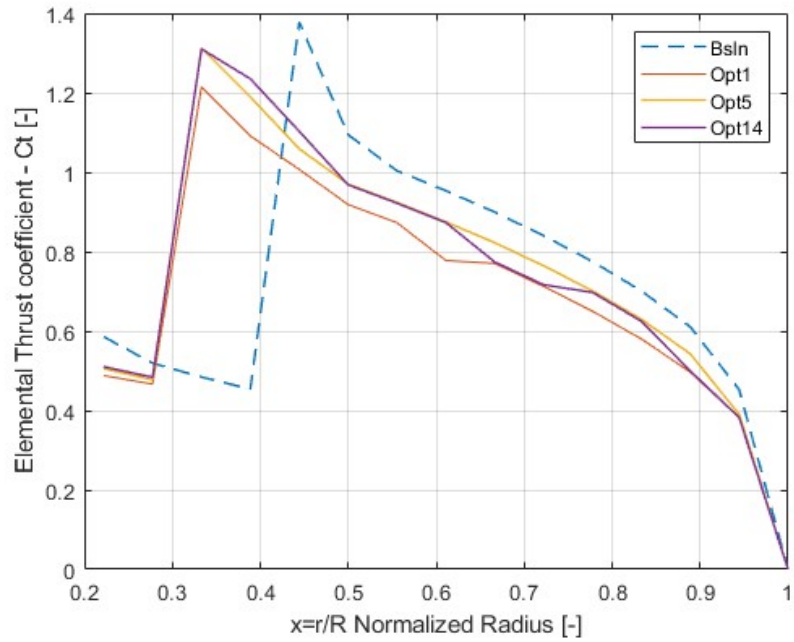
Figure 10.12: Elemental thrust coefficient distribution per unit length

103
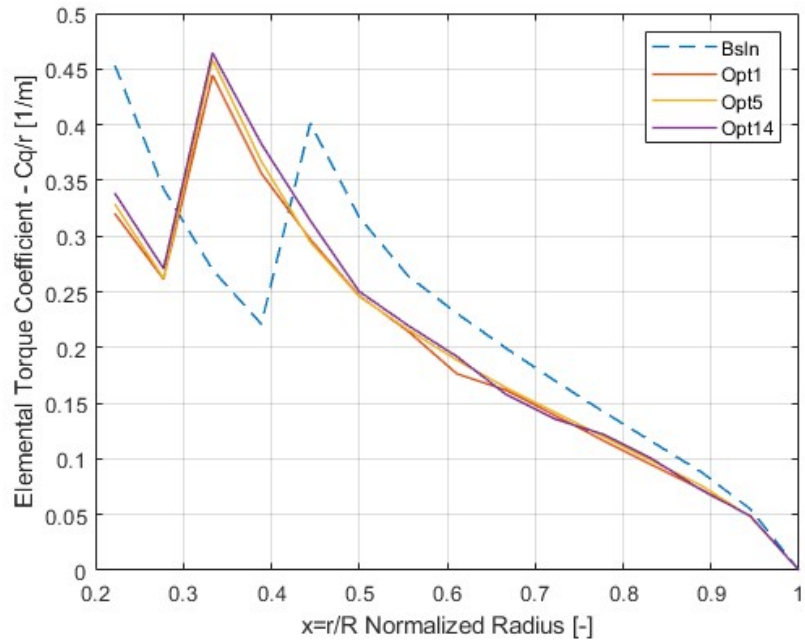
Figure 10.13: Elemental torque coefficient distribution per unit length
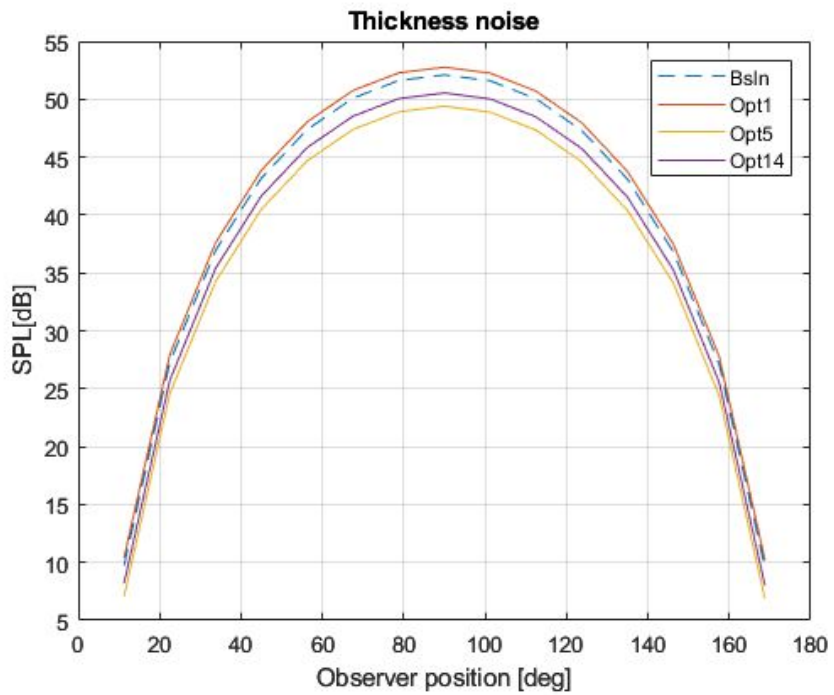
Figure 10.14: Comparison of thickness noise for different blade designs

104
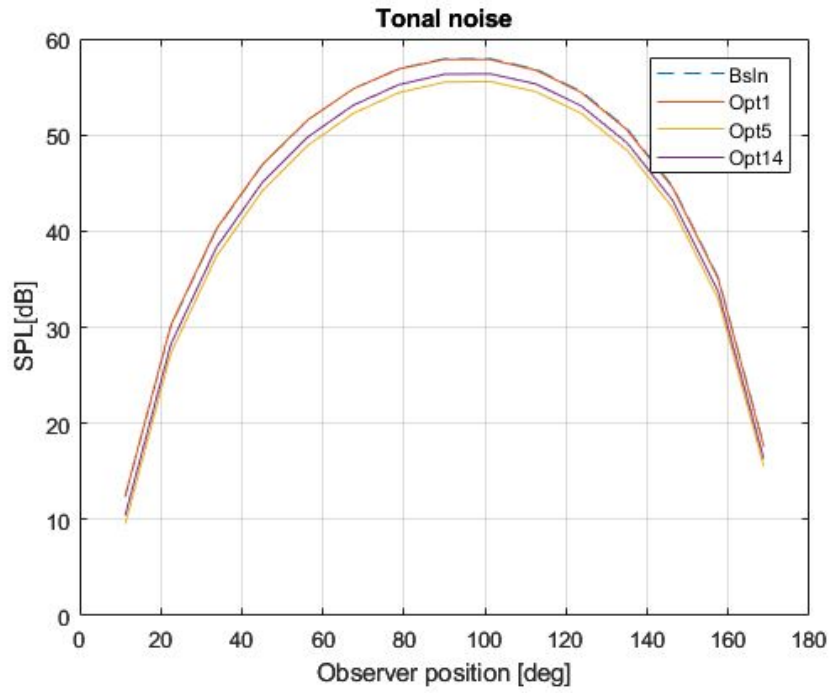
Figure 10.15: Comparison of tonal noise for different blade designs
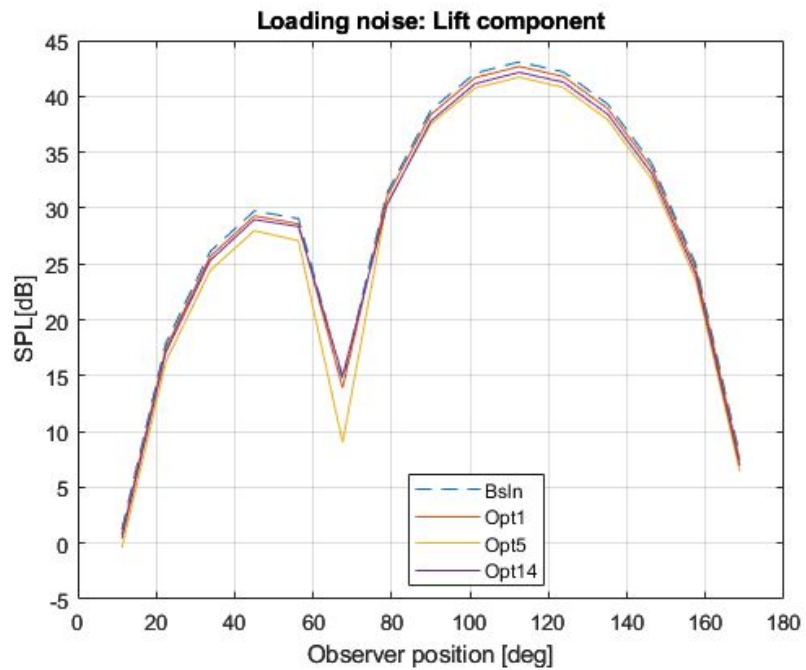
Figure 10.16: Comparison of loading noise due to Lift for different blade designs

105
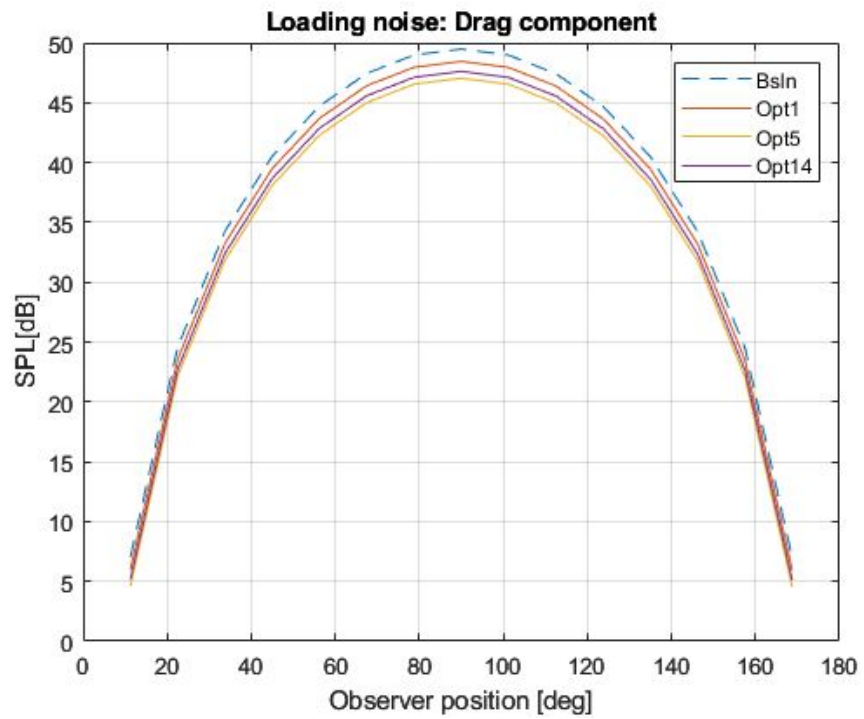
Figure 10.17: Comparison of loading noise due to Drag for different blade designs
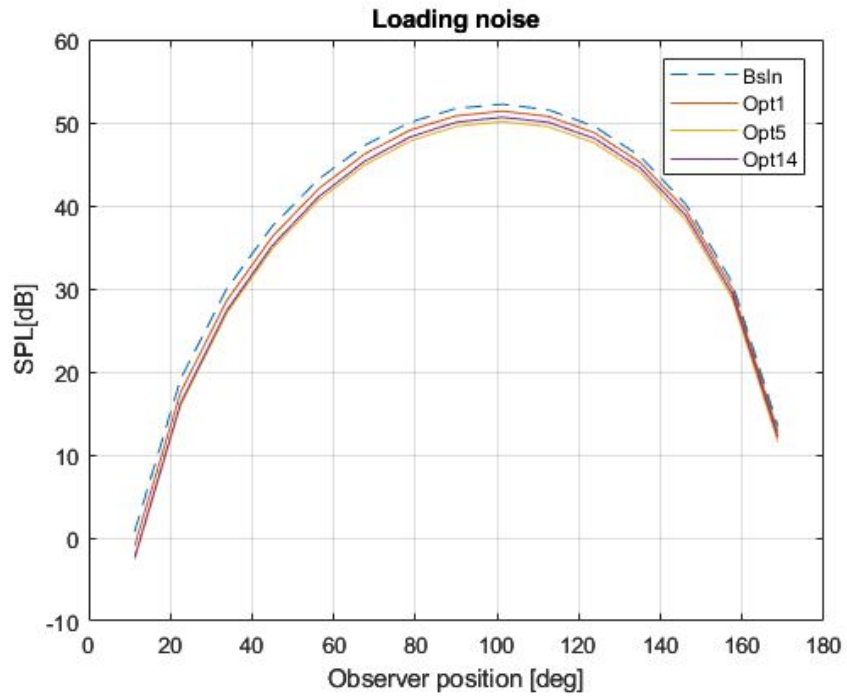
Figure 10.18: Comparison of loading noise for different blade designs
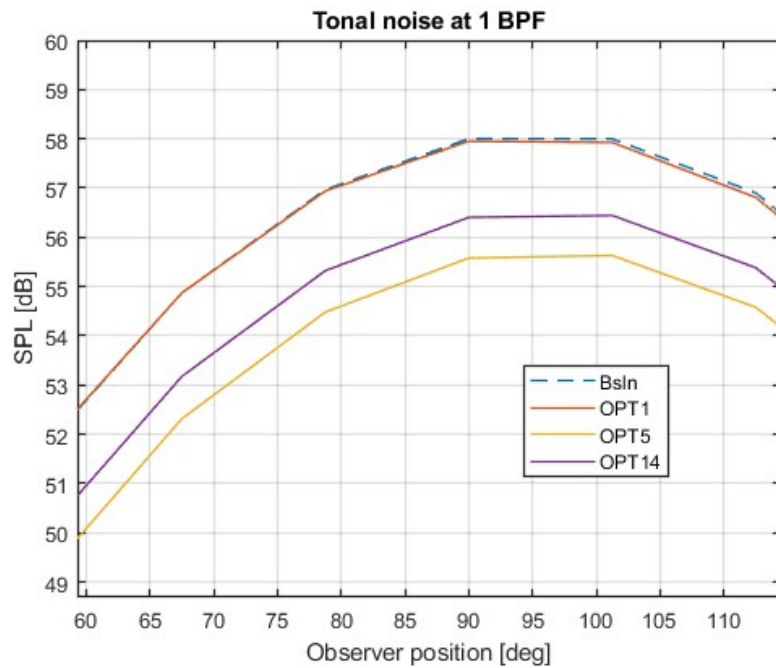
Figure 10.19: Tonal noise for BPF1
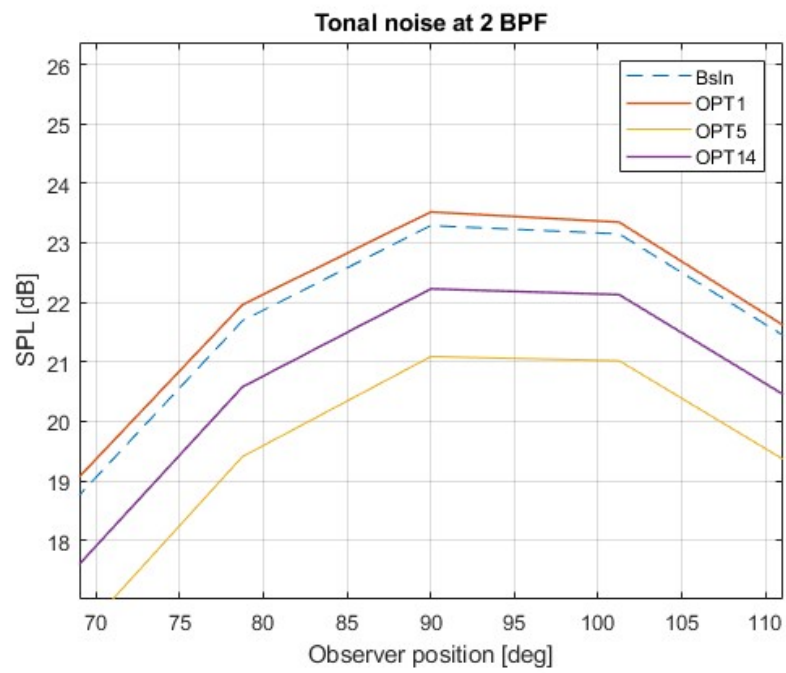
Figure 10.20: Tonal noise for BPF2

Chapter 11

Conclusions and Future Work

11.1 Conclusions

An optimization process combining aerodynamics and aeroacoustics has been carried out at an educational level. Several blades with an increased Figure of Merit of the order of 5% and a maximum -2.5 dB of tonal noise are obtained. The not-very-large gains are reasonable considering that they come only from planform shape modifications of the blade.

11.2 Future work

The current section provides several suggestions for further work that emerged during the development of the thesis.

1. Aerodynamic data of the airfoil at a minimum of five different Reynolds numbers should be incorporated in the BEMT algorithm, as outlined in the research employed in the verification procedure, for a detailed comparison and a more precise prediction of thrust and torque coefficients [14, 15].

2. Coriolis effects and centrifugal forces are not taken into account in the BEMT algorithm as developed in the present thesis, as they were not mentioned in the literature of reference for the comparison of the radial load distributions. They are found to be influential for the boundary-layer characteristics in near-stall conditions, as the Coriolis force acts as a favorable pressure gradient and increases the lift coefficient (+0.1). Moreover, the thickness of the boundary layer is reduced because of the centrifugal force, which causes a displacement of fluid particles outwards. These effects are investigated in Ref. [58, 47].

3. A high-fidelity analysis should be conducted to verify the radial loading distribution prediction and the acoustic outcome, and semi-anechoic wind tunnel tests on a manufactured propeller should be performed to validate the performance of the optimized design. Moreover, when experiments are carried out, the circular array where microphones are mounted on should be replaced with a linear array, to avoid reflection effects and meddling with the jet flow. The computational acoustic setup of observers should be amended accordingly.

4. A structural analysis should be performed to ensure the integrity of the optimized propellers when subject to centrifugal force and aerodynamic load, and so the propeller dynamic response, meaning that the working frequency of the propeller should not correspond to the structural dynamic characteristic frequency.

5. Parameterizations that permit more articulated geometries are widely found and should be employed.

6. An additional research objective could be the comparison of optimizations including and excluding the laminar separation bubbles prediction.

Appendix A

Optimization results across different objective functions and constraints

$c_r[m]$	$c_t[m]$	$\beta_r[deg]$	$A_b[m^2]$	σ [-]
0.0289	0.0094	41.8359	0.0068	0.0966

J=0.1

Thrust [N]	Torque [Nm]	Power [W]	Ct[-]	Cq [-]
4.24 N	0.1001 Nm	41.78 W	0.0124	0.002

η [-]	FM [-]	Ct/σ
0.203	0.5027	0.1287

SPL_{avg} [dB]	$SPL_{\max}$ [dB]	$\max(SPL_V)$[dB]	$\max(SPL_{loading})$ [dB]	$\max(SPL_L)$ [dB]
44.69	58.22	52.10	52.21	43.08

$\max(SPL_D)$ [dB]
49.48

J=0.00001

Thrust [N]	Torque [Nm]	Power [W]	Ct[-]	Cq [-]
4.4054	0.0951	39.83	0.0129	0.0019

η [-]	FM [-]	Ct/σ
1.10E-06	0.5585	0.1337

SPL_{avg} [dB]	$SPL_{\max}$ [dB]	$\max(SPL_V)$[dB]	$\max(SPL_{loading})$ [dB]	$\max(SPL_L)$ [dB]
44.69	58.23	52.09	52.79	39.24

$\max(SPL_D)$ [dB]
52.17

Figure A.1: Output for the baseline propeller at J=0.1 and J=0.00001

Optimization for J=0.1 ; Obj. Functions: FM, SPL_{avg} ;

Obj. Constraints: FM>FM_{bsln}, SPL_{avg}<$SPL_{avg_{bsln}}$, $SPL_{max} < SPL_{max\,bsln}$

	$c_r[m]$	$c_t[m]$	$\beta_r[deg]$	$A_b[m^2]$	σ [-]
Bsln	0.0289	0.0094	41.8359	0.0068	0.0966
OPT1	0.0261	0.0156	37.0605	0.007	0.0991
%	-9.68	65.95	-11.41	2.94	2.59
OPT2	0.0215	0.012	31.9364	0.0057	0.08
%	-25.60	27.65	-23.66	-16.17	-17.18
OPT8	0.0222	0.0136	35.605	0.006	0.0847
%	-23.18	44.68	-14.89	-11.76	12.32

	Thrust [N]	Torque [Nm]	Power [W]	Ct[-]	Cq [-]
Bsln	4.24	0.1001	41.78	0.0124	0.002
OPT1	4.2202	0.0926	38.8	0.0124	0.0018
%	-0.47	-7.492	-7.13	0	-10
OPT2	3.2153	0.065	38.7991	0.0094	0.0013
%	-24.17	-35.06	-7.13	-24.19	-35
OPT8	3.6813	0.0773	32.3912	0.0108	0.0015
%	-13.18	-22.78	-22.47	-12.90	-25

	η [-]	FM [-]	Ct/σ
Bsln	0.2030	0.5027	0.1287
OPT1	0.2175	0.5376	0.1249
%	7.14	5.55	-2.95
OPT2	0.2361	0.5094	0.1179
%	16.30	0.019	-8.39
OPT8	0.2273	0.5246	0.1275
%	11.97	3.00	-0.93

	SPL_{avg} [dB]	SPL_{max} [dB]	max(SPL_V)[dB]	max($SPL_{loading}$) [dB]	max(SPL_L) [dB]
Bsln	44.69	58.22	52.10	52.21	43.08
OPT1	44.52	57.88	52.06	51.5	42.77
Δ	-0.17	-0.34	-0.04	-0.71	-0.31
OPT2	41.26	54.69	49.26	48.59	40.46
Δ	-3.43	-3.53	-2.84	-3.61	-2.61
OPT8	42.50	55.93	50.17	50.16	45.33
Δ	-2.18	-2.28	-1.92	-2.04	2.25

	max(SPL_D) [dB]
Bsln	49.48
OPT1	48.59
Δ	-0.89
OPT2	41.70
Δ	-7.77
OPT8	47.09
Δ	-2.39

Figure A.2: Optimization in favor of FM and SPL_{avg} at J=0.1, without Thrust constraint

Optimization for J=0.1 ; Obj. Functions: FM, SPL_{avg} ;

Obj. Constraints: FM >FM_{bsln}, SPL_{avg}<$SPL_{avg_{bsln}}$, SPL_{max} < $SPL_{max\,bsln}$, Thrust>$Thrust_{bsln}$ *0.85

	$c_r[m]$	$c_t[m]$	$\beta_r[deg]$	$A_b[m^2]$	σ [-]
Bsln	0.0289	0.0094	41.8359	0.0068	0.0966
OPT1	0.0271	0.0147	36.0091	0.0071	0.1003
%	-6.22	56.38	-13.93	4.41	3.830
OPT5	0.0213	0.0127	35.8463	0.0057	0.0807
%	-26.29	35.10	-14.32	-16.18	-16.45
OPT14	0.0216	0.0157	36.362	0.0061	0.0865
%	-25.26	67.02	-13.08	-10.29	-10.45

	Thrust [N]	Torque [Nm]	Power [W]	Ct[-]	Cq [-]
Bsln	4.24	0.1001	41.78	0.0124	0.002
OPT1	4.1517	0.0906	37.94	0.0122	0.0018
%	-2.082	-9.49	-9.191	-1.61	-10
OPT5	3.6048	0.0764	32.01	0.0106	0.0015
%	-14.98	-23.67	-23.38	-14.52	-25
OPT14	3.8398	0.0815	34.15	0.0113	0.0016
%	-9.43	-18.58	-18.26	-8.87	-20

	η [-]	FM [-]	Ct/σ
Bsln	0.2030	0.5027	0.1287
OPT1	0.2188	0.5364	0.1214
%	7.78	6.70	-5.67
OPT2	0.2252	0.5145	0.1311
%	10.93	2.35	1.86
OPT8	0.2249	0.5301	0.1302
%	10.78	5.45	1.16

	SPL_{avg} [dB]	SPL_{max} [dB]	max(SPL_V)[dB]	max($SPL_{loading}$) [dB]	max(SPL_L) [dB]
Bsln	44.69	58.22	52.1	52.21	43.08
OPT1	44.5	57.86	52.76	51.38	42.67
Δ	-0.19	-0.36	0.66	-0.83	-0.41
OPT2	42.06	55.54	49.4	50.13	41.71
Δ	-2.63	-2.68	-2.7	-2.08	-1.37
OPT8	42.99	56.45	50.54	50.65	42.15
Δ	-1.7	-1.77	-1.56	-1.56	-0.93

	max(SPL_D) [dB]
Bsln	49.48
OPT1	48.45
Δ	-1.03
OPT2	47.04
Δ	-2.44
OPT8	47.62
Δ	-1.86

Figure A.3: Optimization in favor of η and SPL_{avg} at J=0.1, under Thrust constraint

Optimization for J=0.1 ; Obj. Functions: η, SPL_{avg} ;

Obj. Constraints: η $>η_{bsln}$, $SPL_{avg}<SPL_{avg_{bsln}}$, $SPL_{max} < SPL_{max\,bsln}$, Thrust$>Thrust_{bsln}$*0.85

	$c_r[m]$	$c_t[m]$	$\beta_r[deg]$	$A_b[m^2]$	σ [-]
Bsln	0.0289	0.0094	41.8359	0.0068	0.0966
OPT10	0.0254	0.0128	32.9895	0.0065	0.0923
%	-12.11	36.17	-21.14	-4.41	-4.45
OPT7	0.0187	0.0128	39.0639	0.0052	0.0736
%	-35.29	36.17	-6.62	-23.52	-23.80
OPT6	0.0211	0.013	35.8787	0.0057	0.0808
%	-26.9896	38.29	-14.23	-16.17	-16.35

	Thrust [N]	Torque [Nm]	Power [W]	Ct[-]	Cq [-]
Bsln	4.24	0.1001	41.78	0.0124	0.002
OPT10	3.64	0.0756	31.6851	0.0107	0.0015
%	-14.18	-24.47	-24.16	-13.71	-25
OPT7	3.6044	0.0767	32.1241	0.0106	0.0015
%	-14.99	-23.38	-23.11	-14.52	-25
OPT6	3.6194	0.0767	31.8348	0.0106	0.0015
%	-14.64	-23.37	-23.80	-14.52	-25

	η [-]	FM [-]	Ct/σ
Bsln	0.203	0.5027	0.1287
OPT1	0.2297	0.527	0.1249
%	13.15	4.83	-2.95
OPT2	0.2244	0.5125	0.1179
%	10.54	1.95	-8.39
OPT8	0.2274	0.5024	0.1275
%	12.02	-0.06	-0.93

	SPL_{avg} [dB]	SPL_{max} [dB]	max(SPL_V)[dB]	max($SPL_{loading}$) [dB]	max(SPL_L) [dB]
Bsln	44.69	58.22	52.1	52.21	43.08
OPT1	43.06	56.44	51.48	49.76	41.37
Δ	-1.63	-1.78	-0.62	-2.45	-1.71
OPT2	41.44	55.03	47.94	50.34	41.83
Δ	-3.25	-3.19	-4.16	-1.87	-1.25
OPT8	42.1	55.58	49.42	50.18	41.76
Δ	-2.59	-2.64	-2.68	-2.03	-1.32

	max(SPL_D) [dB]
Bsln	49.48
OPT1	46.65
Δ	-2.83
OPT2	47.31
Δ	-2.17
OPT8	47.09
Δ	-2.39

Figure A.4: Optimization in favor of FM and SPL_{avg} at J=0.1, under Thrust constraint

Optimization for J=0.00001 ; Obj. Functions: FM, SPL_{avg} ;   **HOVER**

Obj. Constraints: FM >FM_{bsln}, $SPL_{avg}<SPL_{avg_{bsln}}$, $SPL_{max} < SPL_{max\,bsln}$, Thrust>$Thrust_{bsln}$*0.85

	$c_r[m]$	$c_t[m]$	$\beta_r[deg]$	$A_b[m^2]$	$\sigma[-]$
Bsln	0.0289	0.0094	41.8359	0.0068	0.0966
OPT3	0.0287	0.014	29.1293	0.0073	0.1035
%	-0.69	48.93	-30.37	7.35	7.14
OPT2	0.0244	0.013	30.8351	0.0064	0.09
%	-15.57	38.30	-26.29	-5.88	-6.837
OPT1	0.0224	0.013	33.7162	0.006	0.0843
%	-22.4913	38.29787	-19.4085	-11.7647	-6.83

	Thrust [N]	Torque [Nm]	Power [W]	Ct[-]	Cq [-]
Bsln	4.4054	0.0951	39.83	0.0129	0.0019
OPT3	3.974	0.073	30.58	0.0117	0.0014
%	-9.79	-23.24	-23.22	-9.30	-26.31
OPT2	3.7451	0.073	29.45	0.011	0.0014
%	-14.99	-23.24	-26.06	-14.72	-26.31
OPT1	3.7598	0.0684	28.6561	0.011	0.0013
%	-14.65	-28.07	-28.05	-14.72	-31.57

	η [-]	FM [-]	Ct/σ
Bsln	1.10E-06	0.5585	0.1337
OPT3	1.29E-06	0.6234	0.1126
%	17.27273	11.62	-15.78
OPT2	1.27E-06	0.5922	0.1225
%	15.45455	6.03	-8.376
OPT1	1.31E-06	0.6121	0.1303
%	19.09091	9.59	-2.543

	SPL_{avg} [dB]	SPL_{max} [dB]	max(SPL_V)[dB]	max($SPL_{loading}$) [dB]	max(SPL_L) [dB]
Bsln	44.69	58.23	52.09	52.79	39.24
OPT3	43.82	57.13	53.19	50.05	37.38
%	-0.87	-1.1	1.1	-2.74	-1.86
OPT2	42.18	55.61	50.08	50.32	37.6
%	-2.51	-2.62	-2.01	-2.47	-1.64
OPT1	42.5	55.86	51.08	49.98	37.32
%	-2.19	-2.37	-1.01	-2.81	-1.92

	max(SPL_D) [dB]
Bsln	52.17
OPT1	49.31
Δ	-2.86
OPT2	49.59
Δ	-2.58
OPT8	49.23
Δ	-2.94

Figure A.5: Optimization in favor of FM and SPL_{avg} at J=0.00001, under Thrust constraint

Optimization for J=0.1 ; Obj. Functions: FM, SPL_{avg} ;

Obj. Constraints: FM>FM_{bsln}, SPL_{avg}<$SPL_{avg_{bsln}}$, SPL_{max} < $SPL_{max\,bsln}$

	$c_r[m]$	$c_t[m]$	$\beta_r[deg]$	$A_b[m^2]$	σ [-]
Bsln	0.0289	0.0094	41.8359	0.0068	0.0966
OPT1	0.0261	0.0156	37.0605	0.007	0.0991
%	-9.68	65.95	-11.41	2.94	2.59
OPT2	0.0215	0.012	31.9364	0.0057	0.08
%	-25.60	27.65	-23.66	-16.17	-17.18
OPT8	0.0222	0.0136	35.605	0.006	0.0847
%	-23.18	44.68	-14.89	-11.76	12.32

	Thrust [N]	Torque [Nm]	Power [W]	Ct[-]	Cq [-]
Bsln	4.24	0.1001	41.78	0.0124	0.002
OPT1	4.2202	0.0926	38.8	0.0124	0.0018
%	-0.47	-7.492	-7.13	0	-10
OPT2	3.2153	0.065	38.7991	0.0094	0.0013
%	-24.17	-35.06	-7.13	-24.19	-35
OPT8	3.6813	0.0773	32.3912	0.0108	0.0015
%	-13.18	-22.78	-22.47	-12.90	-25

	η [-]	FM [-]	Ct/σ
Bsln	0.2030	0.5027	0.1287
OPT1	0.2175	0.5376	0.1249
%	7.14	5.55	-2.95
OPT2	0.2361	0.5094	0.1179
%	16.30	0.019	-8.39
OPT8	0.2273	0.5246	0.1275
%	11.97	3.00	-0.93

	SPL_{avg} [dB]	SPL_{max} [dB]	max(SPL_V)[dB]	max($SPL_{loading}$) [dB]	max(SPL_L) [dB]
Bsln	44.69	58.22	52.10	52.21	43.08
OPT1	44.52	57.88	52.06	51.5	42.77
Δ	-0.17	-0.34	-0.04	-0.71	-0.31
OPT2	41.26	54.69	49.26	48.59	40.46
Δ	-3.43	-3.53	-2.84	-3.61	-2.61
OPT8	42.50	55.93	50.17	50.16	45.33
Δ	-2.18	-2.28	-1.92	-2.04	2.25

	max(SPL_D) [dB]
Bsln	49.48
OPT1	48.59
Δ	-0.89
OPT2	41.70
Δ	-7.77
OPT8	47.09
Δ	-2.39

Figure A.6: Optimization in favor of FM and SPL_{avg} at J=0.1, without Thrust constraint

Bibliography

[1] *Civil drones (unmanned aircraft)*. URL: https://www.easa.europa.eu/en/domains/civil-drones (visited on 11/20/2023) (cit. on p. 2).

[2] A.J. Torija and C. Clark. «A Psychoacoustic Approach to Building Knowledge about Human Response to Noise of Unmanned Aerial Vehicles». In: *International Journal of Environmental Research and Public Health* (2021) (cit. on p. 4).

[3] A.J. Torija and Zhengguang Li. «Metrics for Assessing the Perception of Drone Noise». In: *Forum Acusticum, Lyon, France. pp.3163-3168* (Dec 2020) (cit. on p. 5).

[4] *Commission Delegated Regulation (EU) 2019/945 of 12 March 2019 on unmanned aircraft systems and on third-country operators of unmanned aircraft systems*. URL: https://eur-lex.europa.eu/legal-content/EN/TXT/?uri=CELEX%3A02019R0945-20200809 (visited on 01/12/2024) (cit. on pp. 5, 31).

[5] *Guidelines on Noise Measurement of Unmanned Aircraft Systems Lighter than 600 kg Operating in the Specific Category (Low and Medium Risk)*. URL: https://www.easa.europa.eu/en/document-library/product-certification-consultations/guidelines-noise-measurement-unmanned-aircraft (visited on 11/10/2023) (cit. on pp. 5, 53).

[6] A. Cambray, E. Pang, S.A.S. Ali, D. Rezgui, and Azarpeyvand M. «Investigation Towards a Better Understanding of Noise Generation from UAV Propellers». In: *AIAA/CEAS Aeroacoustics Conference* (2018) (cit. on p. 5).

[7] Candeloro P., D. Ragni, and T. Pagliaroli. «Small-Scale Rotor Aeroacoustics for Drone Propulsion: A Review of Noise Sources and Control Strategies». In: *Fluids* (2022) (cit. on p. 5).

[8] J. Sun, K. Yonezawa, E. Shima, and H. Liu. «Integrated Evaluation of the Aeroacoustic and Psychoacoustics of a Single Propeller». In: *International Journal of Environmental Research and Public Health, January 2023* () (cit. on p. 5).

[9] D. Weitsman and E. Greenwood. «Parametric Study of eVTOL Rotor Acoustic Design Trades». In: *AIAA Scitech 2021 Forum* (2021) (cit. on p. 5).

[10] P. Yu, J. Peng, J. Bai, X. Han, and X. Song. «Aeroacoustic and aerodynamic optimization of propeller blades». In: *Chinese Journal of Aeronautics* (2019) (cit. on pp. 5, 93).

[11] D. Xue, Q. Yan, Z. Li, and K. Wei. «Multidisciplinary Optimization Design of Low-Noise Propellers». In: *Aerospace* (2023) (cit. on pp. 5, 93).

[12] A. Pagano, L. Federico, and M. Barbarino. «Multi-objective Aeroacoustic Optimization of an Aircraft Propeller». In: *12th AIAA/ISSMO Multidisciplinary Analysis and Optimization Conference* (2008) (cit. on p. 5).

[13] X. Geng, T. Hu, P. Liu, and G. Sinnige T- amd Eitelberg. «Analysis of Thrust-scaled acoustic emissions of aircraft propellers and their dependence on propulsive efficiency». In: *32th Congress of the International Council of the Aeronautical Sciences* (2021) (cit. on p. 5).

[14] D. Casalino, E. Grande, and G. Romani. «Definition of a benchmark for low Reynolds number propeller aeroacoustics». In: *Aerospace Science and Technology* 113,106707 (2021) (cit. on pp. 5, 15, 17, 27, 75–78, 83, 84, 109).

[15] E. Grande, G. Romani, and D. Ragni. «Aeroacoustic Investigation of a Propeller Operating at Low Reynolds Numbers». In: *AIAA Journal* 60 (2)) (2022), pp. 860–871 (cit. on pp. 5, 9, 15, 17, 109).

[16] J.B. Brandt and Selig M.S. «Propeller Performance Data at Low Reynolds Numbers». In: *49thAIAA Aerospace Sciences Meeting* (2011) (cit. on p. 11).

[17] J.H. McMasters and Henderson M.L. «Low-speed Single-Element Airfoil Synthesis». In: *NASA Technical Soaring, Vol VI, No.2* (1979) (cit. on p. 13).

[18] T. Mueller. «Aerodynamic Measurements at Low Reynolds Numbers for Fixed Wing Micro-Air Vehicles». In: *RTO EN-9* (13-17 September 1999) (cit. on pp. 13–15).

[19] J. Winslow, H. Otsuka, B. Govindarajan, and I. Chopra. «Basic Understanding of Airfoil Characteristics at Low Reynolds Numbers $(10^4 - 10^5)$». In: *Journal of Aircraft* 55 (2017) (cit. on pp. 13, 16).

[20] H. Winarto. «BEMT Algorithm for the Prediction of the Performance of Arbitrary Propellers». In: *Melbourne: The Sir lawrence Wackett Centre for Aerospace Design Technoology, Royal Melbourne Institute of Technology* (2004), pp. 1–3 (cit. on pp. 19, 23).

[21] M. Carreno Ruiz and D. D'Ambrosio. «Aerodynamic optimization and analysis of quadrotor blades operating in the Martian armosphere». In: *Aerospace Science and Technology* (2022) (cit. on p. 20).

[22] W.C. Nelson. *Airplane propeller principles.* J. Wiley Sons, Incorporated, 1944 (cit. on p. 21).

[23] E.L. Houghton and P.W. Carpenter. *Aerodynamics for Engineering Students. Fifth Edition.* Butterworth-Heinemann, Oxford, 2003, pp. 541–547 (cit. on p. 23).

[24] Gudmundsson S. «The Anatomy of the Propeller». In: 2014. URL: https://api.semanticscholar.org/CorpusID:107635804 (cit. on p. 24).

[25] D.O. Dommasch. *Elements of Propeller and Helicopter Aerodynamics.* Pitman Pub. Corp., 1953, p. 47 (cit. on p. 26).

[26] Tognaccini R. *Lezioni di aerodinamica dell'ala rotante.* Università degli Studi di Napoli Federico II. Dipartimento di Ingegneria Aerospaziale, 2010-2011 (cit. on p. 27).

[27] Y. El khchine and M. Sriti. «Tip Loss Factor Effects on Aerodynamic Performances of Horizontal Axis Wind Turbine». In: *Energy Procedia* 118 (2017) (cit. on p. 28).

[28] D. Uhlig and M. Selig. «Post Stall Propeller Behavior at Low Reynolds Numbers». In: *46th AIAA Aerospace Sciences Meeting and Exhibit, Reno, Nevada* (January 2008) (cit. on p. 28).

[29] R. Viterna L.and Corrigan. «Fixed pitch rotor performance of large horizontal axis wind turbine». In: *Large Horizontal-Axis Wind Turbines* 1 (1982), pp. 69–85 (cit. on p. 28).

[30] Mahmuddin F. «The Effect of Flat Plate Theory Assumption in Post-Stall Lift and Drag Coefficients Extrapolation with Viterna Method». In: *Journal of Subsea and Offshore - Science and Engineering* 6 (2016) (cit. on p. 29).

[31] Michael Carley. *Some notes on acoustics.* Course notes available on line. 2012. URL: https://people.bath.ac.uk/ensmjc/Notes/acoustics.pdf (cit. on pp. 30, 31).

[32] R. Arina. *Note relative al Corso di Aeroacustica per la Laurea Magistrale in Ingegneria Aerospaziale.* Politecnico di Torino, 2020-2021 (cit. on p. 32).

[33] D.W. Kurtz and J.E. Marte. *A Review of Aerodynamic Noise from Propellers, Rotors, and Lift Fans.* NASA Technical Report 32-7462, January 1, 1970 (cit. on pp. 35, 37).

[34] M. J. Lighthill. «On sound generated aerodynamically I. General theory». In: *Proceedings of the Royal Society of London. Series A. Mathematical and Physical Sciences* No. 1107 (1952), pp. 564–587 (cit. on p. 38).

[35] O. Bergmann, F. Möhren, C. Braun, and F. Janser. «Comparison of Various Aeroacoustic Propeller Noise Prediction Methodologies in Static Operations». In: *AIAA SCITECH 2022 Forum* (January 2022) (cit. on p. 38).

[36] X. Li, M. Jiang, J. Gao, D. Lin, L. Liu, and X. Li. «Recent advances of computational aeroacoustics». In: *Applied Mathematics and Mechanics (English edition)* (2014) (cit. on p. 38).

[37] M.T. Kotwicz Herniczek, D. Feszty, S. Meslioui, J. Park, and F. Nitzsche. «Evaluation of Acoustic Frequency Methods for the Prediction of Propeller Noise0». In: *AIAA Journal* (2019) (cit. on pp. 39, 83).

[38] D. B. Hanson. «Helicoidal Surface Theory for Harmonic Noise of Propellers in the Far Field». In: *AIAA Journal* 1213-1220 (1952), pp. 564–587 (cit. on pp. 39, 40, 44).

[39] D. B. Hanson. «Influence of Propeller Design Parameters on Far-Field Harmonic Noise in Forward Flight». In: *AIAA Journal* No. 18, (11) (November 1980), pp. 1313–1319 (cit. on pp. 39, 40, 49, 62).

[40] B. Magliozzi, D. B. Hanson, and R. K. Amiet. *Aeroacoustics of Flight Vehicles: Theory and Practice. Volume 1: Noise Sources p 1-64*. NASA. Langley Research Center, 1991 (cit. on pp. 43–45).

[41] M. Benedict, J. Winslow, Z. Hasnain, and I. Chopra. «Investigation of Micro Air Vehicle Scale Helicopter Rotor in Hover». In: *International Journal of Micro Air Vehicles* Vol. 7,(3), (2015), pp. 231–255 (cit. on pp. 46, 47).

[42] M. Chusseau, E. Roozen, S. Pauzin, and A. Carrbe. «Light Aircraft Propeller: Design Parameter Effects on Acoustics and Aerodynamics». In: *15th AIAA Aeroacoustics Conference* AIAA 93-4443, (October 25-27, 1993 / Long Beach, CA) (cit. on pp. 46–48).

[43] Donald B. Hanson. «Influence of Propeller Design Parameters on Far-Field Harmonic Noise in Forward Flight». In: *AIAA Journal* Vol. 18, No. 11 (November 1980), pp. 1313–1319 (cit. on p. 48).

[44] Thomas F. Geyer and Danielle J. Moreau. «A study of the effect of airfoil thickness on the tonal noise generation of finite, wall-mounted airfoils». In: *Aerospace Science and Technology* Volume 115, (August 2021) (cit. on p. 49).

[45] Feng Huanhuan, Liu Yonga, Wang Qi, and Zou Sen. «Numerical Study on Tone Noise of Different Thickness Airfoils». In: *IOP Conf. Ser.: Mater. Sci. Eng* 538 012052 (2019) (cit. on p. 49).

[46] H. Patrick, R.W. Finn, and C.K. Stich. «Two and three-bladed propeller design for the reduction of radiated noise». In: *AIAA* (1997) (cit. on p. 50).

[47] J. Goyal, T. Sinnige, F. Avallone, and C. Ferreira. «Aerodynamic and Aeroacoustic Characteristics of an Isolated Propeller at Positive and Negative Thrust». In: *AIAA Aviation 2021 Forum* (2021) (cit. on pp. 61, 62, 109).

[48] D. Casalino, M. Barbarino, and Visingardi A. «Simulation of Helicopter Community Noise in Complex Urban Geometry». In: *AIAA Journal, Vol. 49, No. 8, August 2011* () (cit. on p. 81).

[49] Y. Fuerkaiti, E. Grande, D. Casalino, F. Avallone, and D. Ragni. «Efficient low-fidelity aeroacoustic permanence calculation of propellers». In: *Aerospace Science and Technology, 123* (2022) (cit. on p. 82).

[50] M.T. Kotwicz Herniczek, D. Feszty, S. Meslioui, and J. Park. «Applicability of Early Acoustic Theory for Modern Propeller Design». In: *23rd AIAA/CEAS Aeroacoustics Conference* (2017) (cit. on p. 83).

[51] *Optimization Theory Overview*. URL: https://nl.mathworks.com/help/optim/ug/optimization-theory-overview.html (visited on 11/01/2023) (cit. on p. 89).

[52] N. Rodrıguez, A. Gupta, L. Zabala, and G. Cabrera-Guerrero. «Optimization algorithms combining (meta)heuristics and mathematical programming and its application in engineering». In: *Mathematical Problems in Engineering* (2018) (cit. on p. 90).

[53] M. Albadr, S. Tiun, M. Ayob, and F. AL-Dhief. «Genetic Algorithm Based on Natural Selection Theory for Optimization Problems». In: *Symmetry* (2020) (cit. on p. 91).

[54] *gamultiobj Algorithm*. URL: https://nl.mathworks.com/help/gads/gamultiobj-algorithm.html (visited on 11/10/2023) (cit. on p. 91).

[55] Kalyan D. «Multiobjective Optimization Using Evolutionary Algorithms». In: *John Wiley Sons* (January 2001) (cit. on p. 91).

[56] J. Leishman. *Principles of Helicopter Aerodynamics*. Cambridge University Press, 2006 (cit. on p. 92).

[57] C.W. Acree. «Vertical Climb Testing of a Full-Scale Proprotor on the Tiltrotor Test Rig». In: *Conference Paper. Transformative Vertical Flight 2020,San Jose, CA* () (cit. on p. 93).

[58] J. Bosschers, B. Montgomerie, A.J. Brand, and R.P.J.O.M van Rooy. «Influence of blade rotation on the sectional aerodynamics of rotating blades». In: *22nd European Rotorcraft Forum* (1993) (cit. on p. 109).